UNIVERSITY OF OKLAHOMA GRADUATE COLLEGE

INVESTIGATING THE EFFECTS OF SMALL PEPTIDES ON AMYLOID AGGREGATION

A DISSERTATION

SUBMITTED TO THE GRADUATE FACULTY

in partial fulfillment of the requirements for the Degree of

DOCTOR OF PHILOSOPHY

By ANDREW D. CHESNEY

Norman, Oklahoma

2025

INVESTIGATING THE EFFECTS OF SMALL PEPTIDES ON AMYLOID AGGREGATION

A DISSERTATION APPROVED FOR THE

DEPARTMENT OF CHEMISTRY AND BIOCHEMISTRY

BY THE COMMITTEE CONSISTING OF

Dr. Ulrich Hansmann, Chair

Dr. Doerte Blume

Dr. Yihan Shao

Dr. Rakhi Rajan

I dedicate this work to my friends and family.

Thank you all for pushing me to be the best that I can be.

To my parents and grandparents,

thank you for instilling and nurturing my inquisitive spirit.

Table of Contents

List of Tables

Chapter 3:

Chapter 5:

Chapter 7

List of Figures

Chapter 1:

Chapter 2:

Chapter 3:

Chapter 4:

Chapter 5:

Chapter 7:

Abstract

Amyloids, a class of protein aggregates, are highly stable elongated fibril structures. They are associated with numerous diseases, such as Alzheimer's, Parkinson's, and type II diabetes. Following the COVID-19 pandemic, there have been numerous cases of individuals suffering with Long-COVID, whose symptoms overlap with common neurodegenerative and amyloid associated diseases. To explore the potential interactions between SARS-CoV-2 and amyloid proteins, two amyloidogenic protein fragments from SARS-CoV-2 were investigated with amylin, the amyloid protein associated with type II diabetes, and α-synuclein, associated with Parkinson's. These investigations were performed utilizing all-atomistic molecular dynamics simulations in explicit solvent. Additionally, presented in this dissertation is research performed to identify and evaluate the effect of novel D-retro-inverso (DRI) peptides on mouse serum amyloid A3 (SAA3) fibril stability via virtual screening and molecular dynamics simulations.

Chapter 1 – Introduction

Amyloids are a class of protein assembly characterized by the formation of elongated, unbranched fibril structures with widths ranging from 5 to 20 nm made of repeating β-strands that run perpendicular to the fibril axis[1,2], as shown in **Figure 1**. The formation of amyloid fibrils is highly influenced by the aggregation of hydrophobic residues at the protofibril interface. The interface is stabilized by the interlocking hydrophobic sidechains, forming a highly hydrophobic core referred to as a "steric zipper". Due to the interlocking of the sidechains, any water molecules in the initial interface are driven out. This process is thermodynamically favored as the release of waters results in a favorable gain in entropy and the enthalpic contributions from the backbone hydrogen bonding of the β-sheets. As a result, this amyloidogenic core is highly stable, and can be further stabilized by aromatic stacking of sidechains, and electrostatic interactions. The overall amyloid fibril structure is very thermodynamically stable and is resistant to proteolytic cleavage.

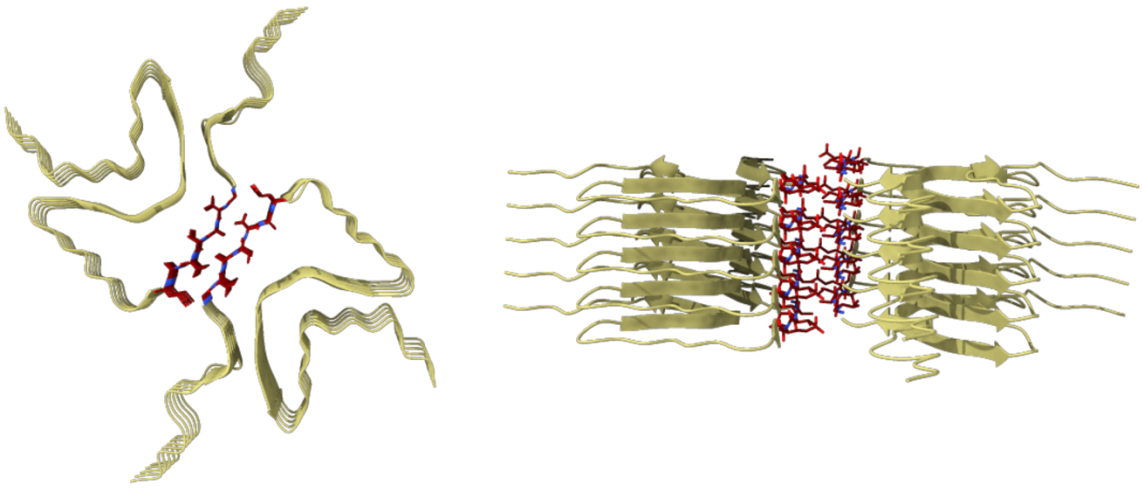

Figure 1: Model of α-Synuclein fibril, PDB: 6OSJ, illustrating the characteristic cross-β sheet motif of amyloid fibrils. The left image is a top-down view of the fibril assembly; the right image is a side-on view. Highlighted in red are the residues involved in the protofibril interface referred to as the 'steric zipper'.

There are 42 known human proteins that can form amyloid fibrils and are associated with various diseases[1], such as Alzheimer's, Parkinson's, and type II diabetes mellitus. Each disease is associated with different proteins that share no similarities in protein sequence and native structures; however, they all share the characteristic amyloid structure when misfolded and aggregated. The formation of amyloids occurs when the precursor protein misfolds from their native structure. This process is often sporadic; however, familial mutations may exacerbate this process introducing structures that are more likely to misfold[3].

In the presented research, I investigated three different amyloid associated proteins: amylin, α-synuclein, and serum amyloid A (SAA). Amylin, also known as Islet Amyloid Polypeptide (IAPP), is a 37-amino acid long protein that has been associated with type II diabetes mellitus. This protein is co-secreted from the β-islet cells of the pancreas with insulin in a ratio of 1:100 amylin to insulin[4,5]. Its normal function is to help regulate glucose levels in the body. However, aggregation of amylin results in the formation of fibrils that disrupt β-islet cells leading to decreased insulin production and increased blood glucose levels. α-Synuclein is a 140-amino acid long protein that is associated with Parkinson's disease. α-Synuclein is expressed predominantly in neurons, and is involved in the transmission of nerotransmitters.[6] Lastly, SAA is an acute phase protein that is associated with the inflammation response. Serum levels of the protein rise drastically, upwards of 1000-fold, in response inflammation stimuli. Chronic inflammation may result in the constant overexpression of SAA leading to increased likelihood of aggregation events occurring. As a result, SAA fibrils are associated with secondary amyloidosis in which the SAA fibrils are deposited in various organs such as the kidneys, liver, and heart.

In 2020, the world experienced a pandemic brought on by the novel corona virus, SARS-CoV-2. This highly infectious virus ravaged through the world, and ultimately caused millions of deaths.[7] Following infection, most individuals only experienced acute symptoms that effected various organ systems. However, some individuals experienced what is referred to as long-COVID which is a multisystemic condition that often causes serve symptoms that occurs usually 3 months after the onset of COVID-19 and lasts at least 2 months and cannot be explained by an alternative diagnosis.[8–10] Individuals suffering from long-COVID have been shown to have an increased risk of developing conditions such as type 2 diabetes[11], cardiovascular, thrombotic and cerebrovascular disease[12], myalgic encephalomyelitis/chronic fatigue syndrome,[13,14] and dysautonomia[15]. Additionally, individuals with long-COVID have shown symptoms of cognitive impairment and memory loss[10], similar to those of individuals experiencing neurodegenerative diseases. Due to the similarities in symptoms and overlap of organ systems effected of individuals with long-COVID and amyloid associated diseases, **Figure 2**, it has been proposed that SARS-CoV-2 may be interacting with amyloid precursor proteins and subsequently promoting the aggregation into fibril structures[16].

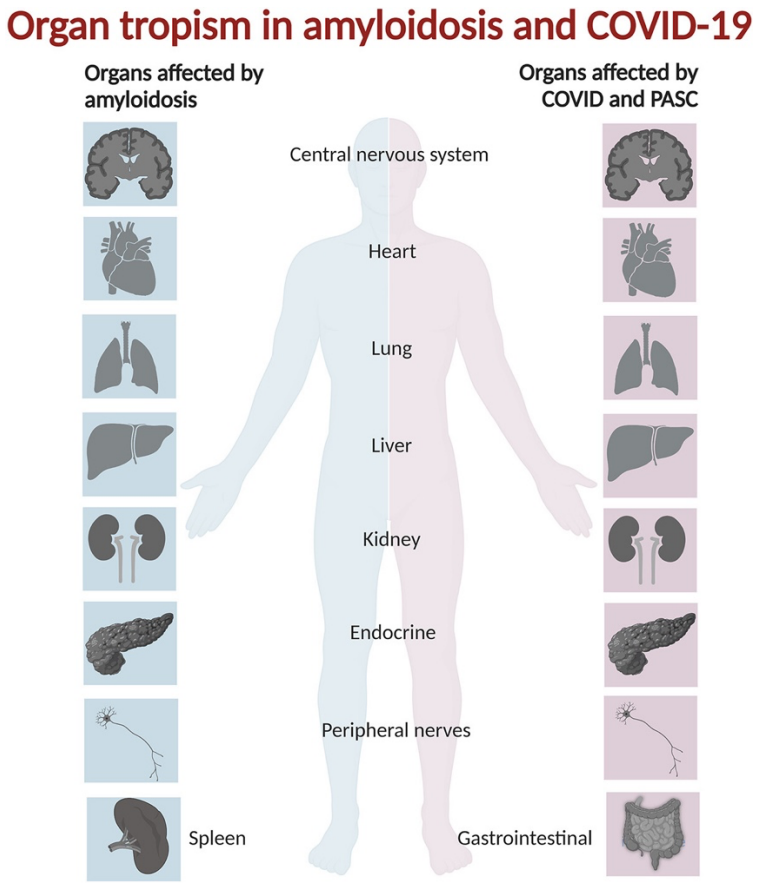

Figure 2: Organs and tissues affected by amyloidosis and COVID/Long-COVID (PASC), indicating many overlapping organ systems.[17]

To investigate the potential effects of SARS-CoV-2 on amyloid proteins, molecular dynamics simulations were utilized as this method provides atom-level resolution of molecular interactions at time scales that are not feasible in traditional lab settings. An overview of molecular dynamics is presented in **Chapter 2** of this dissertation. As the entire virus was not feasible to simulate with the amyloid proteins of interest, we instead investigated the effects of two small amyloidogenic peptides from SARS-CoV-2. The first viral peptide utilized was from the C-terminal region of the envelope protein of SARS-CoV-2, SFYVYSRVK, or SK9. This sequence was selected as it showed homology with a known amyloidogenic peptide segment from the envelope of the SARS-CoV virus[18]. The second viral peptide utilized originated from the spike protein of SARS-Cov-2.

It was shown experimentally[19] that the spike protein is cleaved by the protease neutrophil elastase, which is released by neutrophils locally at sites of inflammation. Of the resulting cleaved peptides, it was shown that the fragment FKNIDGYFKI, or FI10, was capable of forming amyloid fibrils[19]. In **Chapters 3 and 4**, the results of simulations of amylin, with both SK9 and FI10 are presented. Results of simulations of α-synuclein with SK9 and FI10 are presented in **Chapter 5**.

The remaining portion of my dissertation moves away from the potential interactions between SARS-CoV-2 amyloidogenic peptides and amyloid proteins. Instead, it focuses on the identification of novel D-retro-inverso peptides and their effects on mouse serum amyloid A3 (SAA3) fibril stability. Recently it has been shown that following myocardial infarction in mice, cardiac amyloidosis occurs[20]. The resulting fibrils were shown to be formed from aggregated SAA3 released locally by macrophages at the site of inflammation. From previous computational studies performed by the Hansmann group[21], a D-retro-inverso (DRI) peptide, DRI-RSFFS, was purposed as a possible inhibitor for human SAA1 aggregation. A DRI peptide is a peptide in which the sequence of amino acids is reversed and the chirality of each residue is inverted from the L- to D-enantiomer.[22] The resulting peptide is more resistant to proteolytic cleavage[23], while maintaining similar sidechain orientations of the native peptide[22]. This method of peptide modification has been utilized with peptides that target to inhibit amyloid-β aggregation.[24–26] Our experimental collaborators investigating cardiac amyloidosis of SAA3 in mice following myocardial infarction utilized DRI-R5S as a potential treatment. It was found that by administrating DRI-R5S every other day following myocardial infarction, a reduction in scar stiffness and improved cardiac function was observed. To help explain the potential interactions between DRI-R5S and mouse SAA3 and other off-target molecules, I performed molecular

docking studies and binding free energy calculations. **Chapter 6** provides an overview of the experimental results found as well as the computational results during our collaboration with Cimini et. al. To further evaluate the effect of DRI-R5S on mouse SAA3 fibril stability molecular dynamics simulations were performed. Additionally, I sought to identify novel DRI-peptide inhibitors for mouse SAA3 via virtual screening. From this virtual screening three inhibitor candidates were identified. To further validate the effects of these peptides on mouse SAA3 fibril stability, molecular dynamics simulations were performed. The results of these simulations are reported in **Chapter 7**.

Lastly, **Chapter 8** provides a summary of the key results found in the research performed.

Chapter 2 – An Overview of Molecular Dynamics

When investigating proteins, determining the structure is paramount to elucidating the protein's function. Modern structural determination techniques include X-ray crystallography, nuclear magnetic resonance spectroscopy, and cryo-electron microscopy. These methods all allow for the determination of protein structures; however, it is often hard to examine dynamic effects with atomic level resolution. As proteins are not static objects, they should not be studied as such. One potential strategy that can be employed is to simulate the forces applied to the atoms in a structure and observe how these forces propagate through time. This strategy is referred to as molecular dynamics.

Fundamentally, molecular dynamics is a process of iterative calculations of forces in which the positions and velocities of all particles in a system are updated to examine their progression over time. This is possible by treating all the particles in the system as classical Newtonian particles, where forces can be defined as,

$$\boldsymbol{F}_i = m_i \boldsymbol{a}_i = m_i \frac{\partial^2 \boldsymbol{r}_i(t)}{\partial t^2};\ i = 1 \ldots N \quad (1)$$

where m_i is the mass of the i-th particle of a system of N particles, and $\boldsymbol{a}_i$ is the acceleration vector of the i-th particle, which can be also described as the second derivate of the position vector, $\boldsymbol{r}_i$, with respect to time. Practically, it is useful to define forces as the negative gradient of the potential energy function, U($\boldsymbol{r}$) with respect to the position vector $\boldsymbol{r}_i$ of the i-th particle,

$$\boldsymbol{F_i} = -\frac{\boldsymbol{\partial}}{\boldsymbol{\partial r_i}} \boldsymbol{U(r)} \quad (2)$$

To propagate the equation of motion to generate a trajectory of the system, we must integrate Newton's laws of motions which are shown below:

$$\boldsymbol{r}(t+\delta t) = \boldsymbol{r}(t) + \boldsymbol{v}(t)\delta t \quad (3)$$

$$\boldsymbol{v}(t+\delta t) = \boldsymbol{v}(t) + \boldsymbol{a}(t)\delta t \quad (4)$$

$$\boldsymbol{a}(t) = \frac{\boldsymbol{F}(t)}{m} \quad (5)$$

A simple approach to this is by exploring the Taylor expansion of the position function and evaluating it at + δt. Doing so results in the following expression:

$$r(t+\delta t) = r(t) + v(t)\delta t + \frac{1}{2}a(t)\delta t^2 + \frac{1}{6}\frac{\partial^3}{\partial t^3}r(t)\delta t^3 + \mathcal{O}(\delta t^4) \quad (6)$$

Evaluating the same function at – δt results in

$$r(t-\delta t) = r(t) - v(t)\delta t + \frac{1}{2}a(t)\delta t^2 - \frac{1}{6}\frac{\partial^3}{\partial t^3}r(t)\delta t^3 + \mathcal{O}(\delta t^4) \quad (7)$$

Then by adding the resulting equations together and solving for $r(t+\delta t)$ we arrive at the following equation

$$r(t+\delta t) = 2r(t) - r(t-\delta t) + a(t)\delta t^2 + \mathcal{O}(\delta t^4) \quad (8)$$

The resulting function allows for the determination of the position at the next timestep given that the previous positions are known, and the forces are computed without the need to update the velocities initially. Velocities then can be calculated as

$$v(t) = \frac{r(t+\delta t) - r(t-\delta t)}{2\delta t} \quad (9)$$

This simple integration scheme is known as the Verlet algorithm. However, due to the need to subtract very large numbers this algorithm is not the most numerically stable and can lead to numerical errors. Another approach that can be utilized is known as the Leap-Frog algorithm. As

the name implies, in this algorithm the positions and velocities are calculated at different timesteps and 'leap' over each other as the equations are integrated, as illustrated in **Figure 1**.

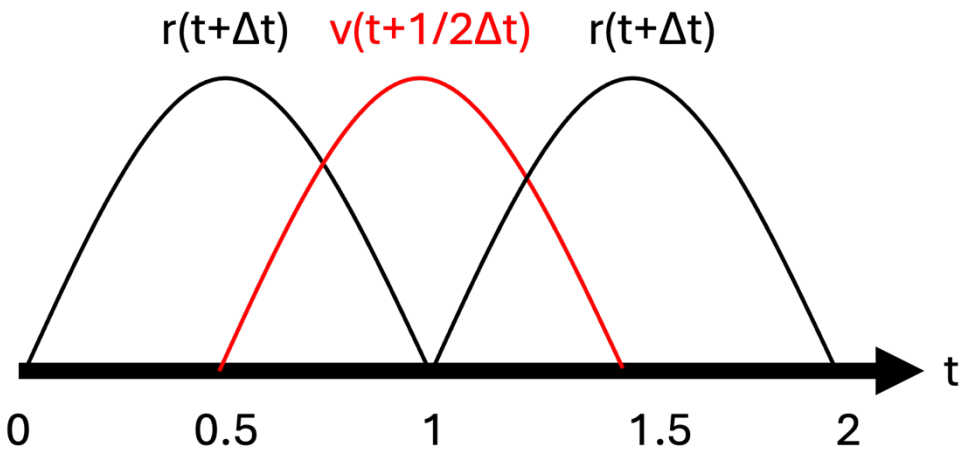

Figure 1: A diagram illustrating the updating behavior of the Leap-frog algorithm, in which positions, **r**, are updated every time step, while velocities are updated every half time step.

As a result of the staggered updating scheme, there is a decrease in the accumulation of numerical errors, while maintaining trajectories that are numerically identical to those produced by the Verlet. This algorithm produces numerically stable trajectories that are time reversible, which is critical for proper molecular dynamic simulations.

As shown above, these techniques can be used to integrate the equations of motion for a system of interest and determine the positions and velocities through forces. To calculate these forces the relationship shown in **Equation 2** is utilized. This relationship illustrates that the negative gradient of the potential energy function can be used to calculate the forces. Therefore, the calculation of the potential energy function is critical to proper molecular dynamics simulations. To calculate the potential energy, a collection of functions with empirically derived constants known as 'forcefields' are used. Parameters may vary between forcefields, however there is a shared

assumption that bonds may not break during a simulation. A simple form of potential energy function can be written as the sum of the bonded and nonbonded interaction energies:

$$U(r) = U_{bonded} + U_{nonbonded} \quad (10)$$

The energies associated with U_{bonded} involve bond stretching, and energies associated with bond angles. On the other hand, nonbonded interactions involve van der Waals and electrostatic forces. A common additive forcefield utilized in protein simulations in the CHARMM forcefield[27]. The potential energy function is modeled in CHARMM by the following expressions, **Equations 11-12**. Represented by **Equation 11** are the bonded terms evaluated to determine U_{bonded}. Those terms include bond stretching, **Equation 11.1**, which describes the distance bound particles deviate from an equilibrium bond length. This behavior is modeled similarly to a classical spring-mass system in which a harmonic oscillator model is used. Here the classical spring constant, k, is described by experimentally derived parameters in the term K_b. Similarly, the energy related to changes in bond angle are calculated by **Equation 11.2**. To account for angle bending, the Urey-Bradley component, **Equation 11.3**, is calculated between the distances of atoms 1 and 3 of the angle formed by atoms 1, 2, and 3. This quantity is also expressed as a harmonic potential. Torsion angles, or dihedral angles, are modeled with **Equation 11.4**, where K_χ is the dihedral force constant, n is the multiplicity of the function, χ is the dihedral angle, and δ is the phase shift. The improper angle, or out of plane bending, is accounted for by **Equation 11.5**.

$$U_{bonded} = U_{bonds} + U_{angles} + U_{UB} + U_{dihedrals} + U_{impropers} \quad (11)$$

$$U_{bonds} = \sum_{bonds} \frac{K_b}{2}(b - b_0)^2 \quad (11.1)$$

$$U_{angles} = \sum_{angles} \frac{K_\theta}{2}(\theta - \theta_0)^2 \quad (11.2)$$

$$U_{UB} = \sum_{Urey-Bradley} \frac{K_{UB}}{2}(b^{1-3} - b_0^{1-3})^2 \quad (11.3)$$

$$U_{dihedrals} = \sum_{dihedrals} K_\chi\big(1 + cos(n\chi - \delta)\big) \quad (11.4)$$

$$U_{impropers} = \sum_{impropers} \frac{K_\varphi}{2}(\varphi - \varphi_0)^2 \quad (11.5)$$

$$U_{nonbonded} = U_{LJ} + U_{elec} = \sum_{\substack{nonbonded \\ i \neq j}} \left(4\varepsilon_{ij} \left[\left(\frac{r_{ij}^{min}}{r_{ij}} \right)^{12} - 2\left(\frac{r_{ij}^{min}}{r_{ij}} \right)^{6} \right] + \frac{q_i q_j}{4\pi\varepsilon_o r_{ij}} \right) \quad (12)$$

The nonbonded interactions are described by two separate terms, the Lennard-Jones potential, and the electrostatic potential. The Lennard-Jones potential describes the effects of van der Waals interactions between nonbonded atom pairs. It is a function of the distances between mass i and j, r_{ij}, as well as the potential well-depth, ε_{ij}, and the separation distance at which the potential energy is zero, r_{ij}^{min}, which both are described by forcefield specific parameters. Pair-wise electrostatic interactions are modeled by a Coulombic potential in which q_i and q_j are the charge of the i-th and j-th atom pair respectively, ε_o is the vacuum permittivity, and r_{ij} is the distance between atom pairs i and j.

By bringing everything together with the forcefield defined potential energy function, and integration techniques, molecular dynamics can calculate the movement and interactions of atoms within a system of interest at atomic level detail. As a result, many quantities of interest such as intermolecular contacts, hydrogen bonding, solvent accessible surface area, and electrostatics, etc.

can be determined at time scales that are not feasible in the traditional laboratory setting. That is why for the work presented in this dissertation, molecular dynamics simulations were used. As this method allowed for the probing of interactions occurring between SARS-CoV-2 derived protein fragments and amyloid proteins. As well as examine the effects of potential peptide inhibitor candidates on the stability of an amyloid fibril of interest.

Chapter 3 – Human Amylin in the Presence of SARS-COV-2 Protein Fragments

To begin my investigations into the effects of amyloidogenic SARS-COV-2 peptides on amyloids, my first project focused on the amyloid protein known as amylin or human islet amyloid polypeptide (hIAPP). The following chapter was published in a similar form in ACS Omega by the author of this dissertation as the following article: Human amylin in the Presence of SARS-COV-2 Protein Fragments, ACS Omega, 8, 12501, by Andrew D. Chesney, Buddhadev Maiti, Ulrich H.E. Hansmann[28]. All text and figures are taken with the permission of the publisher.

Introduction

SARS-COV-2 infections affect not only the respiratory system but a multitude of organs in the human body.[29–32] However, the underlying mechanism for the resulting broad spectrum of symptoms and complications of COVID-19 are not always understood. For instance, diabetes patients have often more severe symptoms of COVID-19, but SARS-COV-2 infections may also trigger onset of diabetes.[33–36] One possible cause for disease symptoms in individuals with type-II diabetes is aggregation of islet amyloid polypeptides (IAPP, also known as amylin). Amylin aggregation (or more general the onset of type-II diabetes) can be caused by various factors, for instance, inflammation induced by infections. However, one can speculate that amylin aggregation is also triggered directly by SARS-COV-2 protein fragments. In previous work, we have presented evidence for such a mechanism for Serum Amyloid A[37] and α-synuclein[38]. However, amylin may be affected differently by interactions with viral proteins since it is more stable than these two proteins, being about 65% helical and stabilized by a disulfide bridge. For this reason, we investigate in this study whether interactions with SARS-COV-2 protein fragments also alter

amylin amyloid formation, and how this effect differs from the one seen in our previous studies. For this purpose, we use all-atom molecular dynamics simulations to investigate the effect of two virus protein fragments on amylin monomers (**Figure 1c**) and two fibril models (**Figure 1d** and **Figure 1e**). The first fragment, SK9, is from the Envelope protein and allows us to connect our work to the above described previous one, while Spike-protein fragment FI10 unique for SARS-COV-2 and has been shown to form amyloids in vitro[15.] Note that the two fragments, shown in **Figure 1a** and **Figure 1b**, are both from viral surface proteins, increasing the chances for interaction with extracellular proteins such as amylin. Unlike in the earlier work on Serum Amyloid A[37] and α-synuclein[38] we do not see a shift in the ensemble of monomers toward more aggregation prone conformations, but rather protection of the native conformation. However, we observe stabilization of fibril structures that not only depends on the viral protein fragments but also on the amylin fibril geometry.

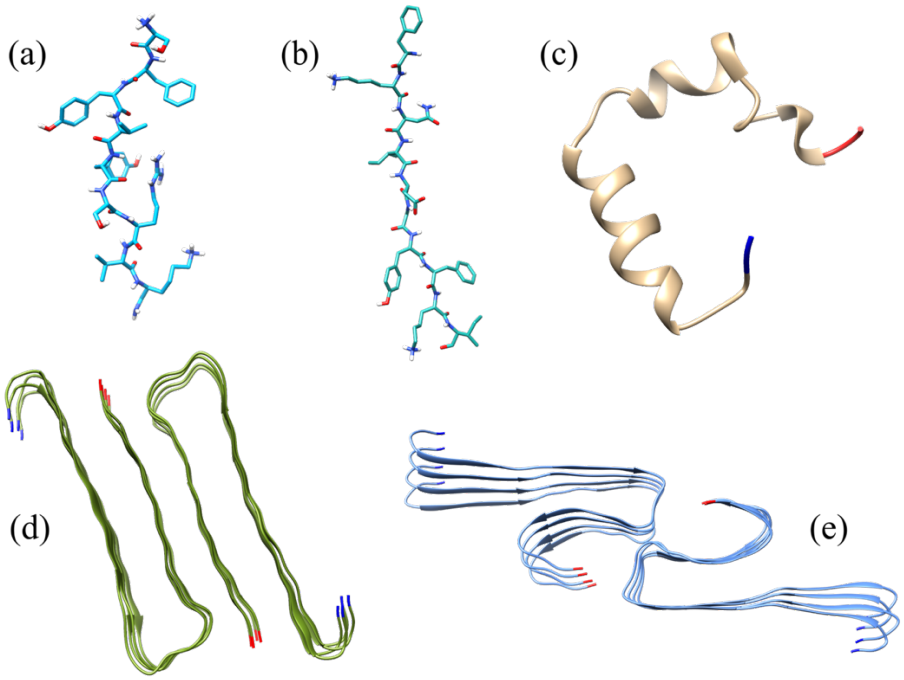

FIGURE 1: Licorice representation of the two SARS-COV-2 protein fragments used in this study: (a) SK9; (b) FI10. Ribbon representations of the (c) amylin monomer (PDB-ID: 2L86), and the two fibril models with PDB-IDs (d) 2F4L and (e) 6ZRF are also shown. The N- and C-terminals are colored in blue and red, respectively.

Materials and Methods

System Preparation

We rely on molecular dynamics (MD) simulations to study the effect of SARS-COV-2 proteins on amylin aggregation. Our study focuses on the change in the conformational ensemble and the stability of amylin monomer and fibrils induced by presence of the nine-residue segment SFYVYSRVK (SK9) of the Envelope protein or the ten-residue segment FKNIDGYFKI (FI10) of the Spike protein from SARS-COV-2. The initial configuration of SK9 is the same as the one used in our previous work,[37,38] and was derived from the model of the SARS-COV-2 Envelope

protein deposited in the MOLSSI COVID-19 hub[39]. The N- and C-terminal of the SK9 segment are capped by a NH_3^+ and -$CONH_2$ group, respectively. Following Nyström and Hammarström[40] the initial configuration of the FI10 viral fragment was derived by extracting the residues F194-I203 from the structure of the SARS-COV-2 Spike protein (PDB ID: 6VXX), with the N- and C-terminal of the peptide capped again by a NH_3^+ and -$CONH_2$ group. To compare the effect of terminal group of the small FI10 peptide on our results, we have also considered the case where the N- and C-termini were capped with a NH_3^+ and -COO^- group, respectively.

The initial conformation of the amylin monomer model has been taken from the Protein Data Bank (PDB). This structure (PDB ID: 2L86 [41]) was resolved by solution NMR, and we add at the N- and C-terminals a NH_3^+ and a COO^- group respectively. Unfortunately, only a few models of amylin fibrils have been resolved and published in the PDB. Due to our familiarity with the fibril model put forward by Eisenberg and co-workers[42], which we have studied in a different context in previous work [43], we again chose this model, but reduced the number of layers from five to four chains in each of the two proto-fibrils. This is because we expect that by decreasing the layers in this manner the stability of the fibril fragment will be lowered, and any potential effect resulting from presence of SK9 will be seen more clearly. Note that while we call this amylin fibril model 2F4L, this is not a PDB-ID but rather our shorthand notation for **T**wo-**F**olds-**F**our-**L**ayers. In order to be consistent with earlier work[43], we add again at the N- and C- terminal a $NH3^+$ and a COO^- group. The initial conformation of the other amylin fibril model was extracted from the Cryo-EM resolved model[44] with PDB-ID: 6ZRF such that it has the same number of chains as the 2F4L fibril model. Note that we use for this second fibril model -$COCH_3$ and -$NHCH_3$ as end groups, allowing us to compare our control simulations (in absence of viral protein fragments) with the experiments

described in Ref [45]. The use of different end-groups is justified as our main interest is the comparison of simulations with and without SARS-COV-2 protein fragments.

Simulations starting from the amylin monomer and fibril models described above serve as control in our study. For investigating the effect of SARS-COV-2 protein fragments on amylin we have performed simulations that start from configurations where either SK9 or FI10 peptides bind to these models. These start configurations were generated using AutoDock Vina[46] and HADDOCK[47,48] by docking the respective segments in a ratio of 1:1 with either monomer or fibrils. The resulting configurations are shown in **Supplemental Figure S1**.

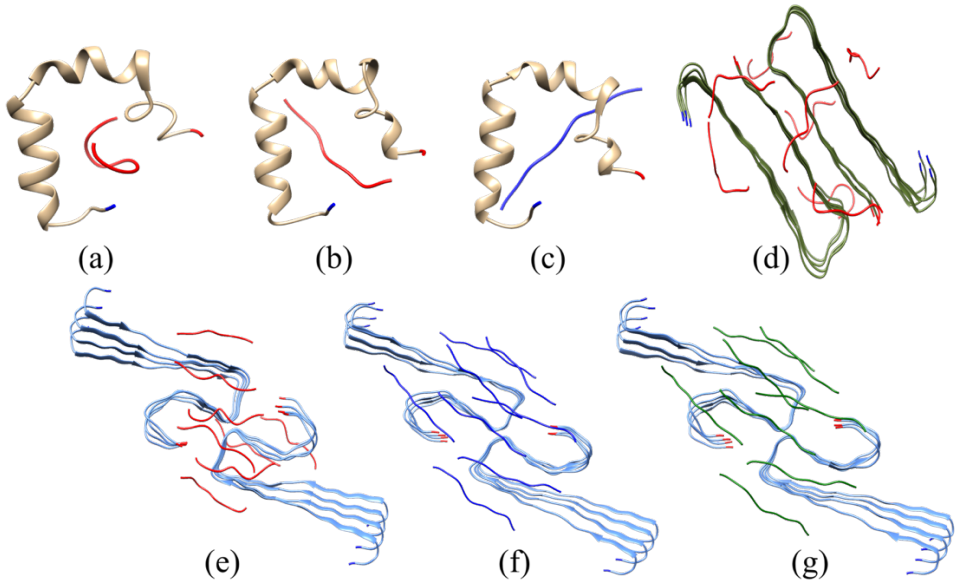

Figure SF1: Start configurations of amylin monomer (a-c), the 2F4L fibril (d) and the 6ZRF fibril (e-g) with SK9 (red) and FI10 (blue (CONH2) and green (COO-)). N-termini are marked in dark blue and C-termini in red.

Note that the viral protein segments are not restricted to these initial positions on monomer or fibrils but can move freely throughout the simulations and even detach from the amylin.

General Simulation Protocol

The set-up and simulation of all systems rely on the GROMACS 2018 and GROMACS 2022 package[49]. We use the CHARMM 36m all-atom force-field[50] with TIP3P explicit water[51] as implemented in the GROMACS package to describe the inter- and intramolecular interactions for the monomer and fibrils. This force-field and water model combination has been found in previous work performed in our group[43,52] and in literature[53–55] to be well-suited for simulations of fibrils and oligomers. Hydrogen atoms are added with the *pdb2gmx* module of the GROMACS suite[49]. The start configurations for all systems are put in the center of the cubic box, with at least 15 Å between the solute and the edge of the box. Periodic boundary conditions are employed. The systems are solvated with water molecules, and counterions are added to neutralize the system, with the Na^+ and Cl^- ions at a physiological ion concentration of 150 mM NaCl. Both the number of water molecules and the total number of atoms are listed in **Table 1**. The energy of each system is minimized by steepest decent for up to 50,000 steps, and afterwards the system is equilibrated at 310K for 200 ps at constant volume and in an additional 200ps at constant pressure (1 atm), constraining the positions of heavy atoms with a force constant of 1000 kJ mol^{-1} nm^{-2}.

Table 1: Simulated systems

System Description	Atoms	Water Molecules	Independent Trajectories	Simulation Length (ns)	Total Sampling (ns)
Monomer (PDB ID: 2L86)					
Control	26,747	8,720	3	4,000	12,000
w/ SK9 (AD-Vina)	26,767	8,733	3	1,000	3,000
w/ SK9 (HADDOCK)	25,856	8,430	3	1,000	3,000
w/ FI10	30,416	10,083	3	1,000	3,000
Fibril Model 2F4L					
Control	118,169	37,884	3	200	600
w/ SK9	120,148	38,090	3	200	600
Fibril Model 6ZRF					
Control	149,710	48,356	3	200	600
w/ SK9	268,411	87,361	3	200	600
w/ FI10-$CONH_2$	268,423	87,373	3	200	600
w/ FI10-COO^-	268,433	87,403	3	200	600

Starting from the above generated initial conformations (shown in Supplemental **Figure SF1**) simulations are performed at constant temperature (310 K) and pressure (1 atm). The temperature is controlled by a v-rescale thermostat[56] with a coupling constant of 0.1 ps, and pressure is kept constant by using the Parrinello-Rahman barostat[57] with a pressure relaxation time of 2 ps. By using the SETTLE algorithm[58] to keep water molecules rigid, and restraining protein bonds involving hydrogen atoms to their equilibrium length with the LINCS algorithm[59], we are able to use a time step of 2 fs for integrating the equations of motion. Because of the periodic boundary conditions, we compute the long-range electrostatic interactions with the particle-mesh Ewald (PME) technique, using a real-space cutoff of 12 Å and a Fourier grid spacing of 1.6 Å. Short-range van der Waal interactions are truncated at 12 Å, with smoothing starting at 10.5 Å. For each system, we follow three independent trajectories differing by their initial velocity distributions. The length of the various trajectories is also listed in **Table 1**.

Trajectory Analysis

The molecular dynamics trajectories are analyzed with the GROMACS tools[49], VMD[60] and MDTraj software[61]. For visualization of trajectory conformations we use VMD[60], and UCSF Chimera[62]. The root-mean-square deviation (RMSD), root-mean-square-fluctuation (RMSF), radius of gyration (RGY) and solvent accessible surface area (SASA) are calculated using GROMACS tools, for the latter quantity using a spherical probe of 1.4 Å radius. The residue-wise contact frequencies are calculated using VMD and MDTraj software, defining contacts by a cutoff 4.5 Å in the closest distance between heavy atoms in a residue pair. Hydrogen bonds are defined by a distance cutoff of 3.5 Å between the donor and acceptor atoms and an angle cutoff of 30°. The residue-wise secondary structure propensity is calculated in VMD by the STRIDE algorithm[63].

In order to avoid the in our case prohibitive computational costs of free energy perturbation methods, thermodynamic integration, or similar approaches are binding free energies of the viral protein fragments to amylin fibrils approximated by the molecular mechanics Poisson-Boltzmann surface area (MM-PBSA) method as implemented in the GROMACS suite[49,64]. This approximation is not without problems, with one important drawback being that it neglects entropic contributions of the solute. As MM-PBSA is therefore not suitable for studying the binding of the viral protein fragments SK9 and FI10 to amylin monomers, we use for these systems instead the approach described in Bellaiche et. al[65]. This approach was used earlier to study inhibition of Aβ amyloid formation by small peptides[66] and relies on calculating a dimensionless association constant from the distribution of bound and unbound conformations. For comparison, we also estimate binding free energies with the protein binding energy predictive model

(PRODIGY) which is based on a simple linear regression of the number of interfacial contacts between residues in a protein-protein complex[67].

Results and Discussion

1) MONOMER SIMULATIONS

We start our investigation into the effect of SARS-COV-2 protein fragments on amylin aggregation by first looking into the changes of the ensemble of monomer conformations induced by viral proteins. In our previous work we have demonstrated that presence of the nine-residue-long C-terminal fragment SK9 (SFYVYSRVK) of the SARS-COV-2 Envelope protein shifts the ensemble of SAA[37] and αS[38] monomers toward more aggregation-prone conformations, increasing in this way the probability for amyloid formation. The starting point for our present simulations is the amylin monomer model with PDB-ID: 2L86[41] in complex with SK9. By comparing two different programs (AutoDock Vina and HADDOCK) to identify potential binding sites[46–48] we come up with two distinct sets of trajectories. This allows us to probe the effect of the initial binding site on our results. A third set of trajectories was started from a configuration where the Spike protein fragment FI10 (FKNIDGYFKI) binds to the amylin monomer. This fragment, cleaved by the enzyme neutrophil elastase, which is released from neutrophils during acute inflammation, is unique for SARS-COV-2 and has been shown to form amyloids *in vitro*.[40] Simulations of SK9 or FI10 interacting with amylin are compared with control simulations where the viral protein fragments are absent. PDB-files of start and final configurations of all runs are available as **supplemental material**.

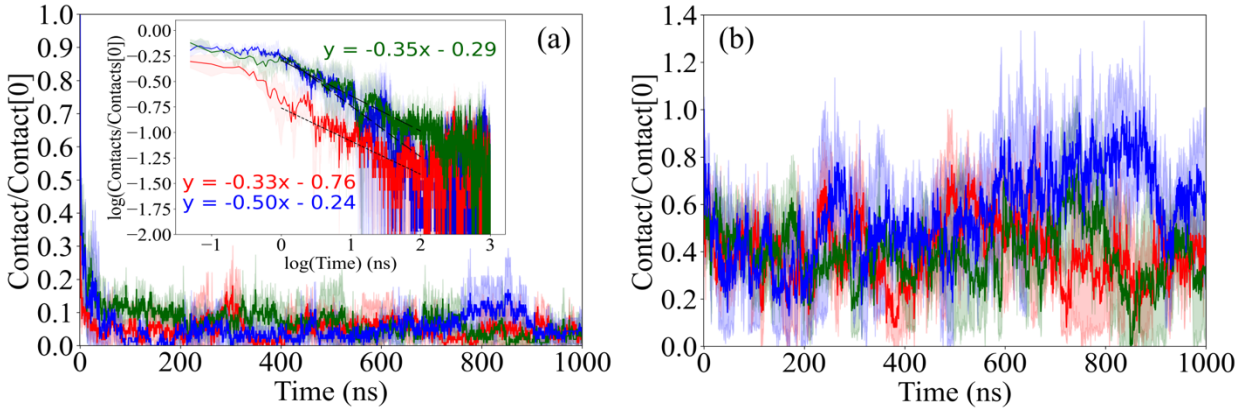

Figure 2: Averaged number of *original* contacts between SK9 and amylin as a function of time (a). The corresponding average number of *all* contacts (including newly formed ones) is shown in (b). Contacts are normalized to one for the respective start configurations. Red marks data from runs where the initial binding site of SK9 was found with AutoDock Vina, greens such where the binding site was found with HADDOCK. Blue marks data from runs where FI10 interacts with amylin.

In **Figure 2a,** we show the number of original binding contacts (contacts that exist at start) as function of time. Initially, SK9 has in one set (binding site derived with Autodock Vina) 37 contacts with the amylin monomer, 35 in the other set (binding site found with HADDOCK); and FI10 forms 38 contacts with the amylin monomer. In order to compare the various trajectories, we normalize the number of contacts for each system to a value of one at start. The log-log-plot in the inset shows that the number of contacts decreases by a power-law, with the exponent 0.34(1) for SK9 and of about 0.5 for FI10. These exponents indicate a diffusive motion of the viral protein fragments in relation to the amylin monomer, that in the case of SK9 is slower than in normal diffusion, and normal (i.e., random-walk-like) for FI10. Note, however, that in the process of this diffusive motion many of the disappearing original contacts are replaced by contacts not seen in the start conformation. As a consequence, the total number of contacts between the viral protein fragment and amylin decreases much slower, see **Figure 2b**, staying for SK9 close to 30%-40% of the initial number. For FI10 the number of contacts stays even at 60% -70%. The center-of-

mass distance between both molecules is around 5 Å -20 Å, but occasionally increases up to 50 Å, see **Supplemental Figure SF2**.

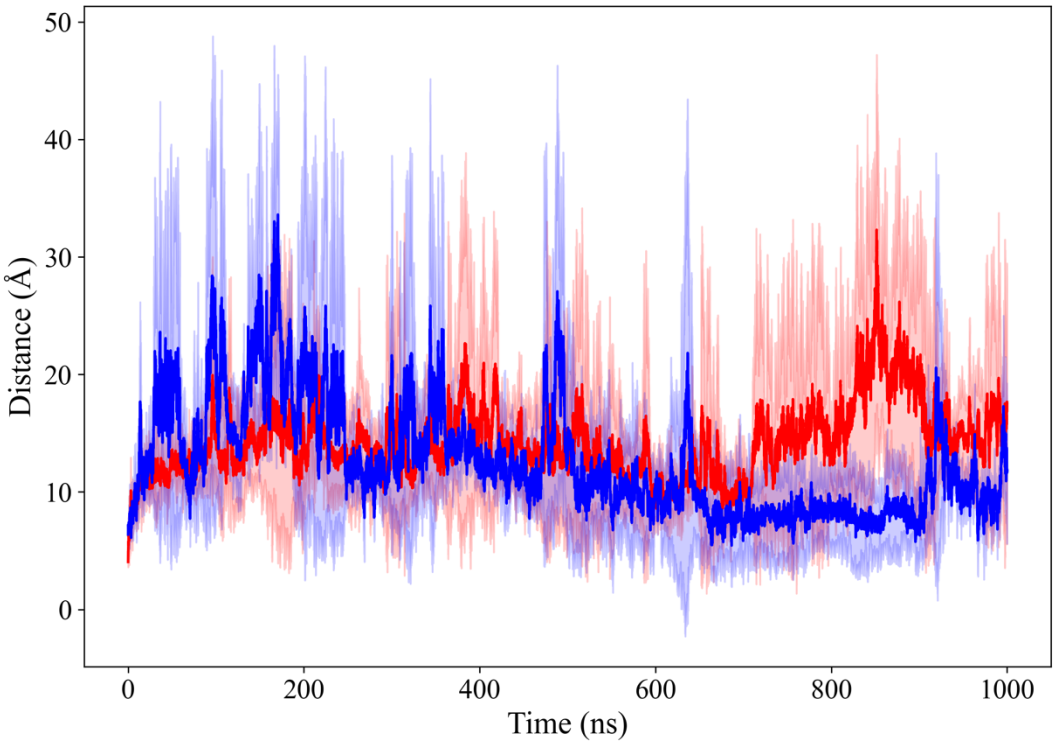

Figure SF2: Average center of mass distances as function of time between the amylin monomer and SK9 (red) or FI10 (blue)

Hence, most of the time, the viral protein fragment stays attached to the amylin monomer, but occasionally it separates transiently. Together with our binding free energy estimates, the above observations indicate stable binding between the viral protein fragment and amylin. For SK9 we find a value of -21(3) kJ/mol for the trajectories starting from the Autodock Vina generated binding site, and a value of -22(5) kJ/mol for trajectories with HADDOCK generated initial binding site.

These values are calculated taking the last 800 ns of the trajectories into account and only decrease to -18.2 (3) kJ/mol and -18(5) kJ/mol, when only the last 200 ns are considered. Hence, the binding of SK9 to amylin depends little on the binding site and decreases only slowly. For FI10 we find values of -22(2) kJ/mol taking the last 800 ns into account. When restricting the calculation to the last 200 ns, we have to rely on only two trajectories as in the third one FI10 stayed in contact with amylin over the whole time, i.e., did not allow estimation of a binding energy with the approach *Bellaiche et. al*.. Hence, our values of -28(4) kJ/mol for the two trajectories where we could use the approach is an underestimation. Nevertheless, this value indicates already that FI10 is binding more tightly with the amylin monomer than SK9, which is supported by all other quantities in **Table 2**. We remark that we observe the independence from the binding site, and the difference between SK9 and FI10, also when the binding energies are estimated directly from the start conformation, using Prodigy[67]. However, the obtained absolute values of the free energies, -45.6 (0) kJ/mol for SK9 docked with AutoDock Vina and -49.4 (7) kJ/mol for those docked with HADDOCK, and -41.6 (7) kJ/mol for FI10, are larger for Prodigy, which uses an approximation.

Note that except for the terminal residues we find little difference in the frequencies that SK9 residues bind to amylin, with slightly higher values for the central Y5 and lower values for residues S6-S8 than for residues F2-V4. On average the binding probability of a SK9 residue is about 60(10)% for the last 800 ns, and 50(20)% when calculated only over the last 200 ns. Here, the terminal residues are excluded in the calculation of the binding probabilities. Similarly, we find for FI10 a binding probability of about 60(10)%, when measured over the last 800 ns, and 70(20)% when measured only over the last 200 ns. However, residues D5-I10 of FI10 have higher binding propensities than the first three residues (FKN), see **Supplemental Table ST1**.

Table ST1: Residue-wise binding frequencies of SK9 and FI10 residues to amylin monomers

SK9 (Autodock Vina) Binding Frequencies (%)									
Residues	Ser-1	Phe-2	Tyr-3	Val-4	Tyr-5	Ser-6	Arg-7	Ser-8	Lys-9
Last 800ns	37 (6)	63 (9)	67 (4)	70 (10)	80 (10)	55 (6)	56 (2)	50 (5)	42 (3)
Last 200ns	28 (3)	58 (5)	70 (20)	70 (20)	70 (20)	50 (10)	48 (8)	30 (20)	28 (9)
SK9 (HADDOCK) Binding Frequencies (%)									
Last 800ns	41 (8)	70 (10)	70 (10)	60 (20)	80 (20)	50 (10)	60 (20)	40 (10)	30 (10)
Last 200ns	40 (30)	60 (20)	60 (30)	50 (30)	60 (30)	30 (10)	50 (30)	30 (10)	30 (20)

FI10 Binding Frequencies (%)										
Residues	Phe-1	Lys-2	Asn-3	Ile-4	Asp-5	Gly-6	Tyr-7	Phe-8	Lys-9	Ile-10
Last 800ns	64 (5)	54 (6)	48 (7)	76 (8)	53 (6)	50 (10	80 (4)	86 (6)	58 (5)	77 (9)
Last 200ns	70 (20)	70 (20)	54 (7)	90 (10)	60 (10)	40 (30)	91 (4)	95 (3)	60 (10)	80 (20)

The frequencies are again independent from the initial binding site. Similarly, no clear pattern is seen in the amylin residues binding with SK9 or FI10, see **Supplemental Figure SF3**, reflecting the diffusive movement of the viral protein fragment in relation to the amylin monomer.

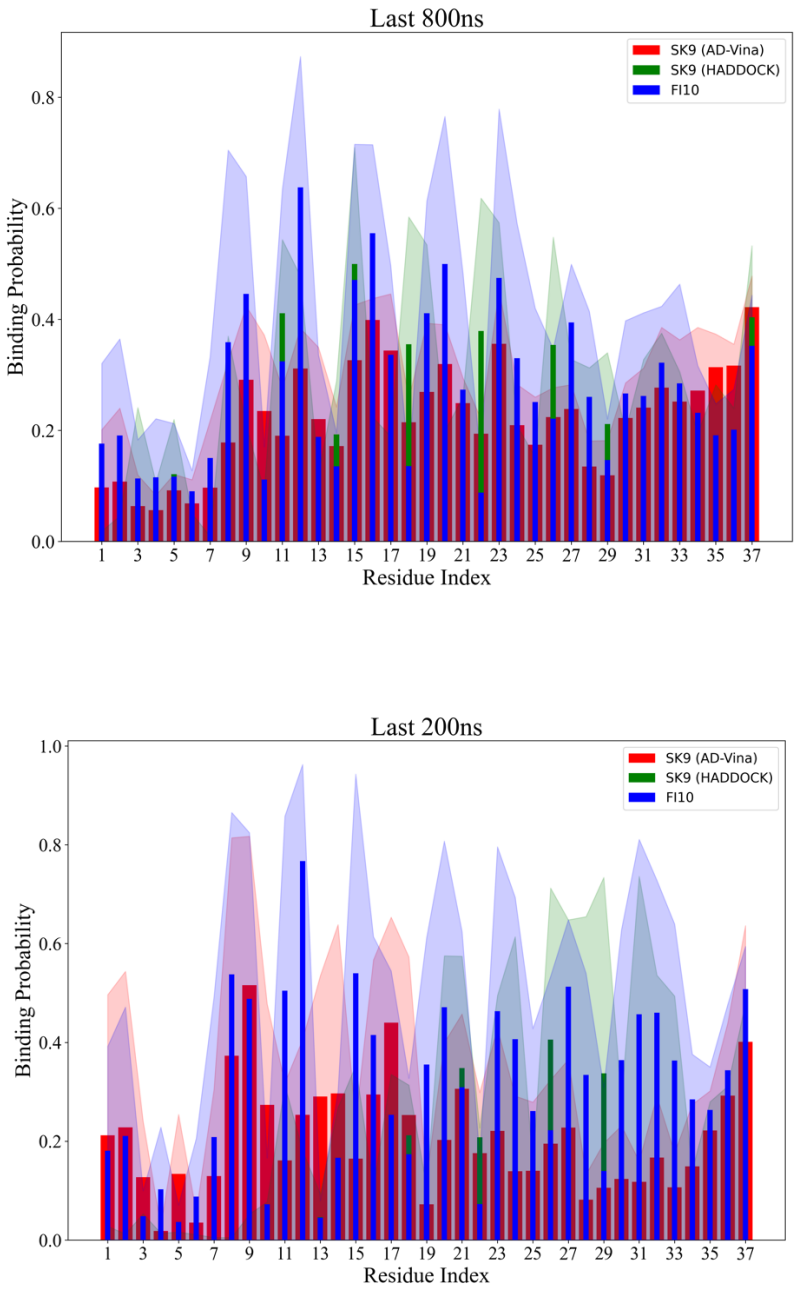

Figure SF3: Residue-wise binding frequencies for the amylin monomer interacting with SK9 or FI10 (blue). Binding sites for SK9 were found by two docking programs, Autodock Vina (red) and Haddock (green).

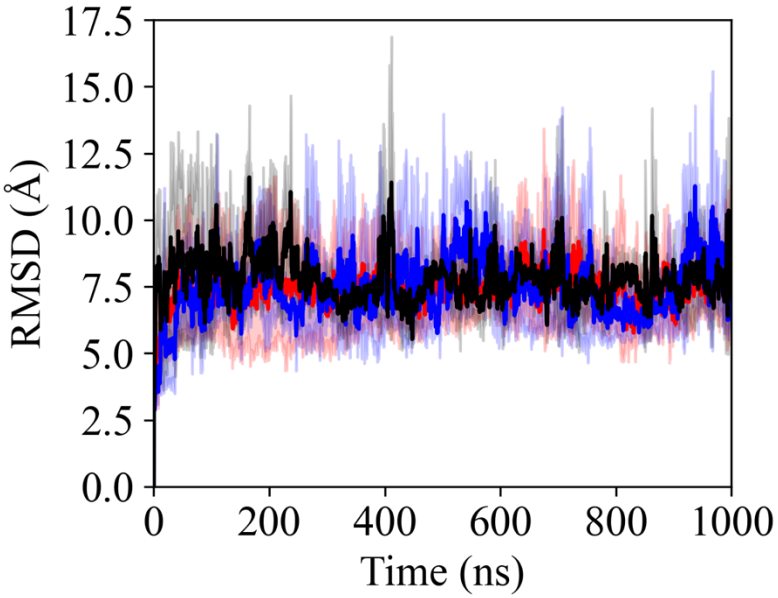

Figure 3: Average root-mean-square-deviation (RMSD) to the start conformation as function of time for amylin in presence of SK9 (red) or FI10 (blue), and in absence of SK9 and FI10 (black). The RMSD is evaluated over backbone atoms only. Averages are calculated over all trajectories for each system.

The effect of the binding of the viral protein fragment on the ensemble of amylin monomer conformations can be seen by comparing the simulations of amylin interacting with either SK9 or FI10 with the control simulations (where the viral protein fragments are absent). One example is the root-mean-square-deviation (RMSD) to the start conformation which we show as function of time in **Figure 3**. Shown are averages over all trajectories for each system. We have merged all trajectories of SK9 interacting with the amylin monomer as the data for SK9 differ little between the runs starting from binding sites generated with Autodock Vina and the ones generated by HADDOCK. After a rapid initial increase the RMSD stays in the control simulations, and for amylin interacting with either SK9 or FI10, almost constant over the whole length of the trajectory. However, while the RMSD values differ little between control and amylin in presence of either SK9 or FI10, visual inspection of the final configurations (**Figure 4**) shows differences in size and

helicity to the control. For instance, the average radius of gyration of the amylin monomers is 11.4(2) Å for the SK9 and 12.9(1) Å for the FI10 simulations, which is higher than in the control 11.2(1) Å. A similar pattern is seen for the end-to-end distance, where we find 19(5) Å in the SK9 simulations, 26(5) Å in presence of FI10, and 20(1) Å for the control, see **Table 2.** While the average solvent accessible surface area (SASA) of the amylin monomer is similar in all cases, we find that the ratio of exposed surface of hydrophilic residues to that of hydrophobic residues is 0.86(2) in the simulations where FI10 interacts with amylin, which is comparable to the 0.85(3) measured in simulations where SK9 interacts with amylin, but both values are smaller than the value (0.875(5)) measured in the control simulations where neither of the viral protein fragments is present.

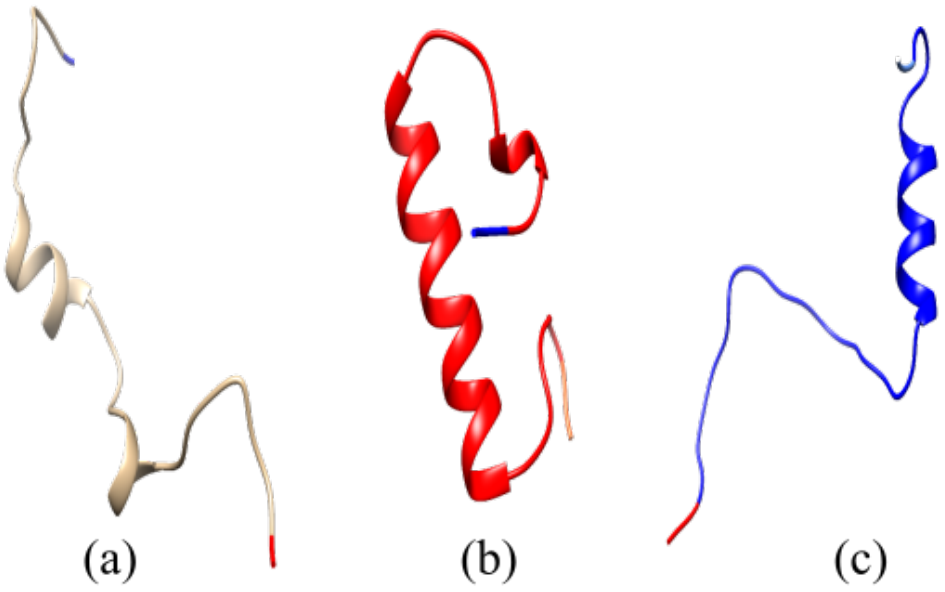

Figure 4: Representative snapshots of the final amylin conformations in absence (a), and presence of SK9 (b) or FI10 (c). The N- and C-terminals are colored in blue and red, respectively

Table 2: Averages of various quantities measure in simulations of amylin monomer alone, or in presence of SK9 or FI10. Averages are over the last 200 or 800 ns, and over all respective trajectories. Contacts and binding free energies are between SK9 or FI10 and amylin. With the exception of the binding free energies are all quantities normalized to One at start.

System	Time Interval	Total Contacts	Original Contacts	SASA	R_g	Helicity	End-to-End Distance	ΔG_{bind} (kJ/mol)
Control	800ns	—	—	0.96 (4)	1.04 (5)	0.6 (1)	1.325 (5)	—
	200ns	—	—	0.98 (7)	1.1 (1)	0.6 (2)	1.27 (8)	—
w/ SK9	800ns	0.39 (8)	0.05 (2)	0.96 (3)	1.14 (6)	0.79 (9)	1.4 (3)	-21 (4)
	200ns	0.33 (8)	0.04 (1)	0.96 (3)	1.07 (6)	0.68 (3)	1.3 (4)	-18 (4)
w/ FI10	800ns	0.60 (2)	0.054 (7)	1.00 (5)	1.2 (1)	0.79 (5)	1.61 (9)	-22 (2)
	200ns	0.70 (5)	0.08 (3)	1.03 (6)	1.2 (1)	0.72 (3)	1.7 (3)	-28 (4)

The reason for the differences in these ratios, calculated from averages taken over the last 200 ns, can be seen in **Figure 5** where we show the root-mean-square-fluctuations (RMSF) of residues, evaluated over the last 200 and 800 ns. This quantity allows us to quantify the flexibility of residues. Hence, the lower values seen in presence of SK9 or FI10 indicate a stabilization of the monomer. Especially, we see in the control simulations that residues N22 - N31 have a higher flexibility than others, but this distinction is not seen in the simulations where the viral protein fragments are present. This is interesting as human amylin differs in the segment N22 - N31 from the less aggregation-prone rat amylin: rat amylin contains three proline residues between residues 20-29 that disrupt secondary structure due to structural hindrance and decreased flexibility of the protein backbone. As a result of these residues, also found in the amylin fibril inhibiting Pramlintide, rat amylin is less aggregation-prone and more soluble than human amylin. Hence, interactions with SK9 or FI10 mimic the protective effect of the rat mutations or in the amyloid inhibiting drug Pramlintide.

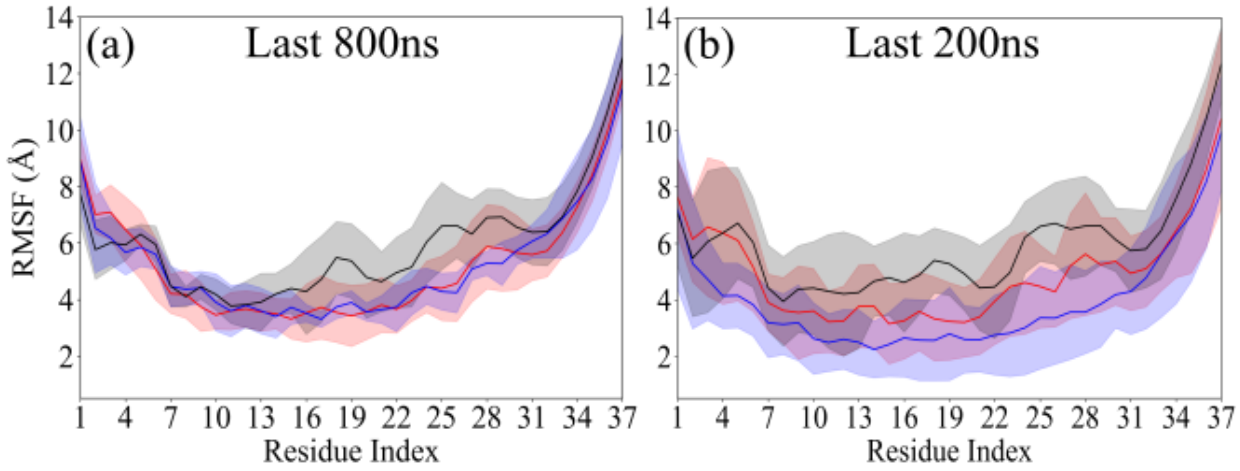

Figure 5: Residue-wise root-mean-square fluctuation of the amylin monomer in absence (black) or presence of SK9 (red) or FI10 (blue) calculated over (a) last 800ns and (b) last 200ns of the simulations. Shaded regions mark the standard deviations of the shown quantities.

Indeed, we find that the average helicity, also shown in **Table 2,** stays marginally higher when amylin interacts with either SK9 (68(3)%) or FI10 (72(3)%) than in the control (60(20)%). However, these averages may be misleading. We show in **Figure 6** the residue-wise helicity measured over the last 200 ns in simulations with either SK9 or FI10 present, but subtracting the corresponding values measured in the control. In the presence of the viral protein fragments, residues F15 to S28 consistently have higher average helicity than observed in the control while residues A5 to N14 have a lower average helicity. This decrease of helicity for segment A5 to N14 is more pronounced for FI10, which at the same time also stabilizes helicity in residues L16 to T30 more than SK9. Residues S20 to S29 have been shown to form the primary amyloidogenic domain in amylin[68] while the N-terminal residues (1-8) are not directly involved in fibril formation[69]. Hence, we conclude that both SK9 and FI10 are stabilizing the native monomer conformation of amylin, decreasing the chance of unfolding and seeding amyloids. This is unlike what we observed in our previous work where we found that SK9 shifted the ensemble of SAA[37] and αS[38] monomers

toward more aggregation prone conformations, increasing in this way the probability for amyloid formation.

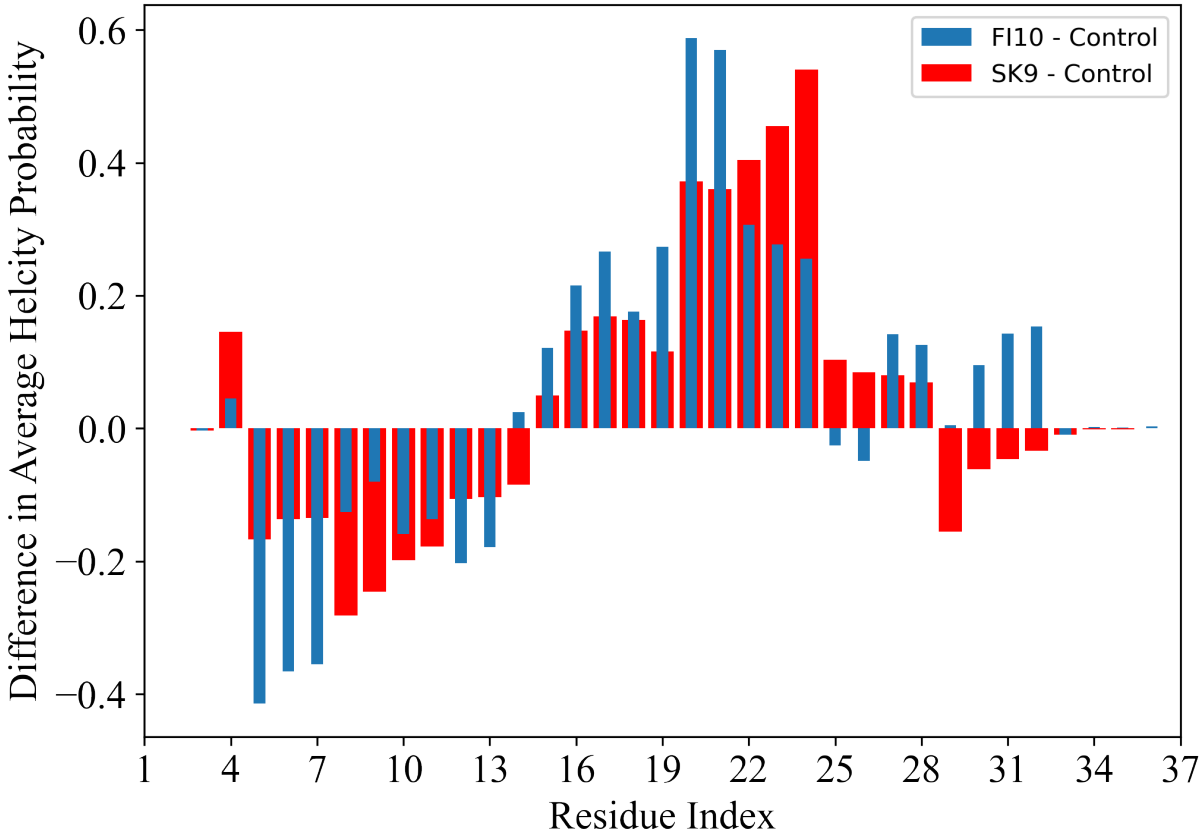

Figure 6: Residue-wise helicity of amylin monomer in presence of SK9 (red) and FI10 (blue) calculated over the last 200ns. Shown is the difference to the corresponding values in the control simulations where the viral protein fragments are absent.

2) FIBRIL SIMULATIONS

According to the Le Chatelier's principle, the equilibrium between amylin in its functional form and aggregated in amyloids can be shifted not only by increasing the propensity of aggregation-prone monomer conformations, raising in this way the probability for amyloid formation, but also by stabilizing existing fibrils. Amyloids with more stable fibrillar structures have been shown to have higher rates of aggregation.[70] In previous work[37,38] we observed such stabilizing effect for the SK9 fragment on SAA and αS fibrils. Hence, we have also probed the change in stability of

amylin fibrils introduced by interactions with virus protein fragments. Unfortunately, only few models of amylin fibrils have been resolved and published in the PDB. Because of our familiarity with the fibril model put forward by Eisenberg and co-workers[42], which we have studied in a different context in previous work [43], we chose again this model, called by us 2F4L. PDB-files of start and final configurations are available as **supplemental material**.

At the start of the three trajectories, the viral SK9 peptides form 257 contacts with the 2F4L fibril, about 32 contacts per chain. This number decreases rapidly over the first nanosecond, and more slowly afterwards, but stays constant after 100 ns at 109(6) contacts, about 42% of the original number of contacts, i.e., on average 14(1) contacts per chain, leading to a binding free energy of -17(9) kJ/mol between an amylin and a SK9 peptide. Note that not all the observed contacts appear in the start configuration: the SK9 fragment is not tethered to the fibril and new contacts are formed as old original ones dissolve.

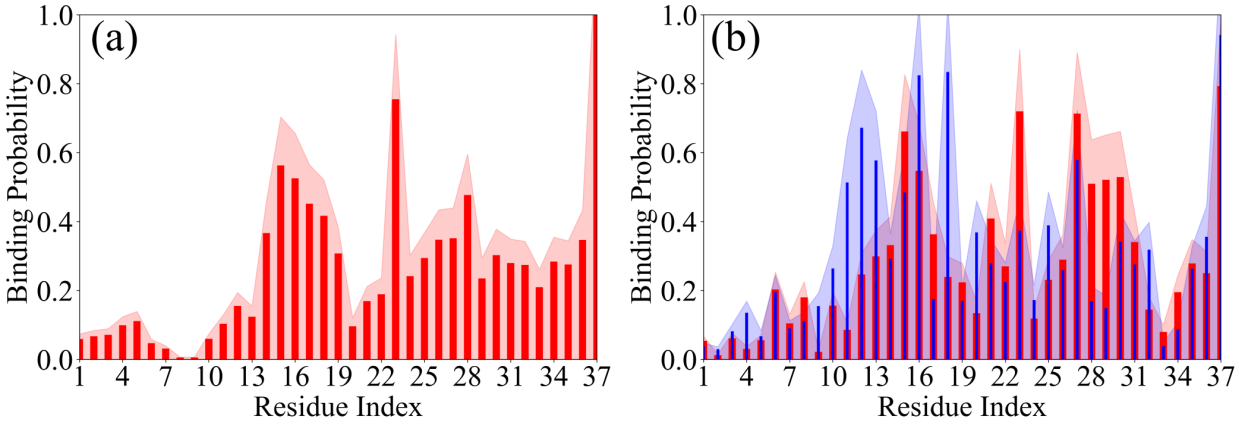

Figure 7: Residue-wise frequency of contacts of (a) the fibril model 2F4L with SK9, and (b) the fibril model 6ZRF, with either SK9 (red) or FI10 (blue). Shaded regions mark the standard deviation of the averages.

We show in **Figure 7a** the frequency with of amylin residues having a contact with SK9 as measured over the last 100 ns. The main binding regions include residues N14-S19 (centered around F15) in the outer layers of the protofibrils, and residues F23 and Y37 on the edge of the protofibril layers. Residues N14-S19 make hydrophobic contacts and π-π stacking interactions with SK9 to hold the SK9 close to protofibril layers, stabilizing their stacking. On the other hand, the residues F23 and Y37 form hydrogen bonds and hydrophobic contacts with SK9 that stabilize the packing of the two protofibrils. Hence, the effect of SK9 binding to the amylin chains is a slight stabilization of the fibril. This can be seen in **Figure 8a** where we compare the residue-wise root-mean-square fluctuation of the amylin fibril 2F4L bound to SK9 with that of the control (2F4L without SK9 present). This quantity is a measure for the flexibility of a residue, and while the overall form of the RMSF curves are similar, residues in the 2F4L fibril bound to SK9 have consistently lower RMSF values, i.e., are less flexible.

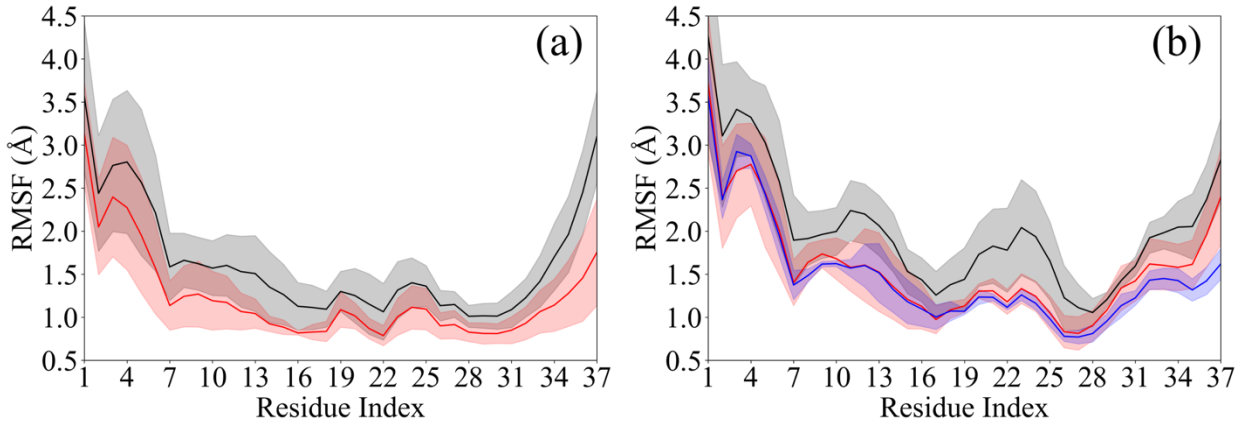

Figure 8: Residue-wise RMSF for (a) the fibril model 2F4L and (b) the fibril model 6ZRF. The black curve marks data from the simulation in absence of viral protein fragments, while the red curve show the results obtained when SK9 is present, and the blue curve data for when FI10 is interacting with the amylin fibrils. Shaded regions mark the standard deviation of the averages.

Consequently, the final configurations are less disturbed than in the control, see the insets of **Figure 9a** which shows as a function of time the root-mean-square deviation (RMSD) to the start

conformation, taken over all backbone atoms of all chains. Note that we consider for the calculation of the RMSD only residues 8-37 as the first seven residues are disordered. While the differences to the control are small, they show larger stability of 2F4L bound to SK9 than for the fibril in absence of SK9. This can also be seen by visual inspection of the final conformations shown in the insets. Consistent with the RMSF plots, this stabilization is mainly due to the reduction of flexibility for the first N-terminal residues which in the control appear to disrupt the stacking of the N-terminal β-sheets.

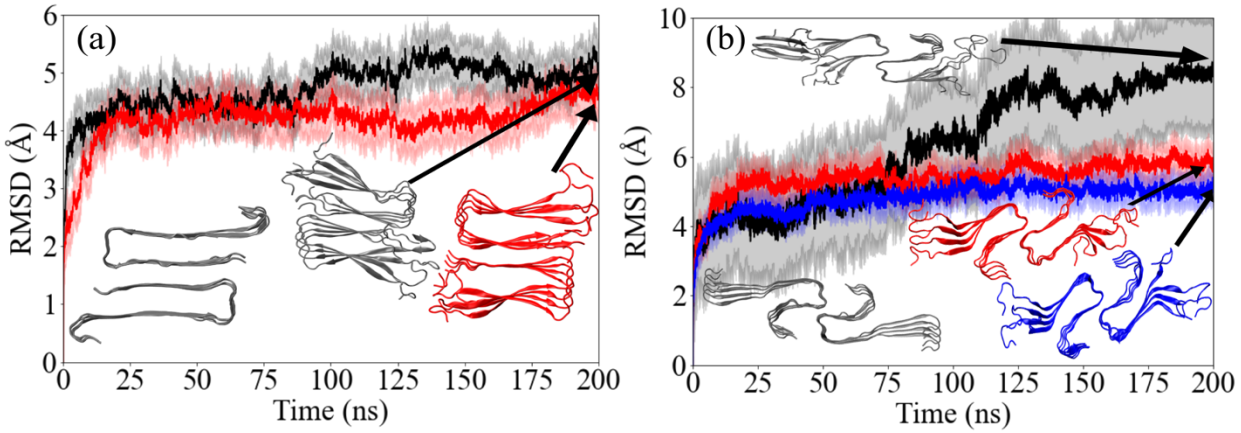

Figure 9: RMSD to the start configuration as function of time for (a) the fibril model 2F4L and (b) the fibril model 6ZRF. The RMSD is calculated over all backbone atoms in residues 8-37 of all chains in the respective fibril model. Black curves are from the control simulations while red curves are from data measured in simulations where SK9 is present, and similarly, blue curves for the case of FI10 interacting with the amylin fibril. Shaded regions mark the standard deviation of the averages. The start configuration and representative final configurations are shown as insets.

However, these visual impressions are difficult to quantify. For instance, the solvent accessible surface area (SASA), in **Table 3,** is 15251(356) Å^2 when measured in the simulations with SK9 which is smaller than when measured in the absence of SK9, 15554(337) Å^2. The difference between the two averages is small and within the standard deviations, but the difference becomes more pronounced when excluding the disordered first seven residues from the SASA calculation, leading to 11445 (254) Å^2 in presence of SK9 versus 11853(227) Å^2 in the control. The reduction

in exposed surface area in the complex is slightly higher for hydrophobic residues than for hydrophilic residues, but no clear picture emerges. Little difference is also seen for the average distance between the two folds (8.1(3) Å in presence of SK9 vs 8.2(8) Å for the control), and the averages distance between layers is with 2.9(2) Å about the same in presence and absence of SK9. Similarly, neither our MMPBSA approximations of the packing and stacking free energies nor the measured numbers of stacking or packing contacts or hydrogen bonds in **Table 3** give a clear signal explaining the observed weak stabilization.

Table 3: Various quantities averaged over the last 100 ns of three trajectories in simulations of the amylin 2F4L fibril model in absence or presence of SK9.

	Control	w/ SK9
Total SASA (Å^2)	15554 (337)	15251 (356)
Hydrophobic SASA (Å^2)	7782 (243)	7623 (229)
Hydrophilic SASA (Å^2)	7773 (141)	7628 (134)
Packing distance (Å)	8.2 (8)	8.1 (3)
Stacking distance (Å)	2.9 (2)	2.9 (2)
Packing contacts	90 (11)	92 (16)
Stacking contacts	494 (26)	492 (20)
Intrachain contacts	1226 (6)	1242 (3)
Packing hydrogen bonds	6 (3)	7 (3)
Stacking hydrogen bonds	146 (5)	142 (7)
Intrachain hydrogen bonds	17 (1)	16 (1)
Packing free energy (kJ/mol)	-189.2 (48.3)	-184.8 (77.0)
Stacking free energy (kJ/mol)	-251.1 (163.1)	-305.7 (113.7)

Correspondingly, we do not see a difference in the frequency of the S29-S29 hydrogen bonds found in earlier work by us to be crucial for the packing of the fibril, or for the N31-N31 bond important for stacking[43]. However, we find the frequency of the F23-Y37 packing hydrogen bonds raised from 18% to 38%, and the distribution of packing hydrogen bond is tighter in presence of SK9. While in the simulations of the control more than 20 types of hydrogen bonds contribute at

least 1% to the measured packing hydrogen bonds, only seven types of hydrogen bonds do this in the simulations where SK9 is present. Hence, while the number of packing hydrogen bonds changes little in presence of SK9, the bonds are less transient when SK9 interacts with the fibril. The more focused packing can be also seen in the map of packing contacts in **Supplemental Figure SF4a-c**.

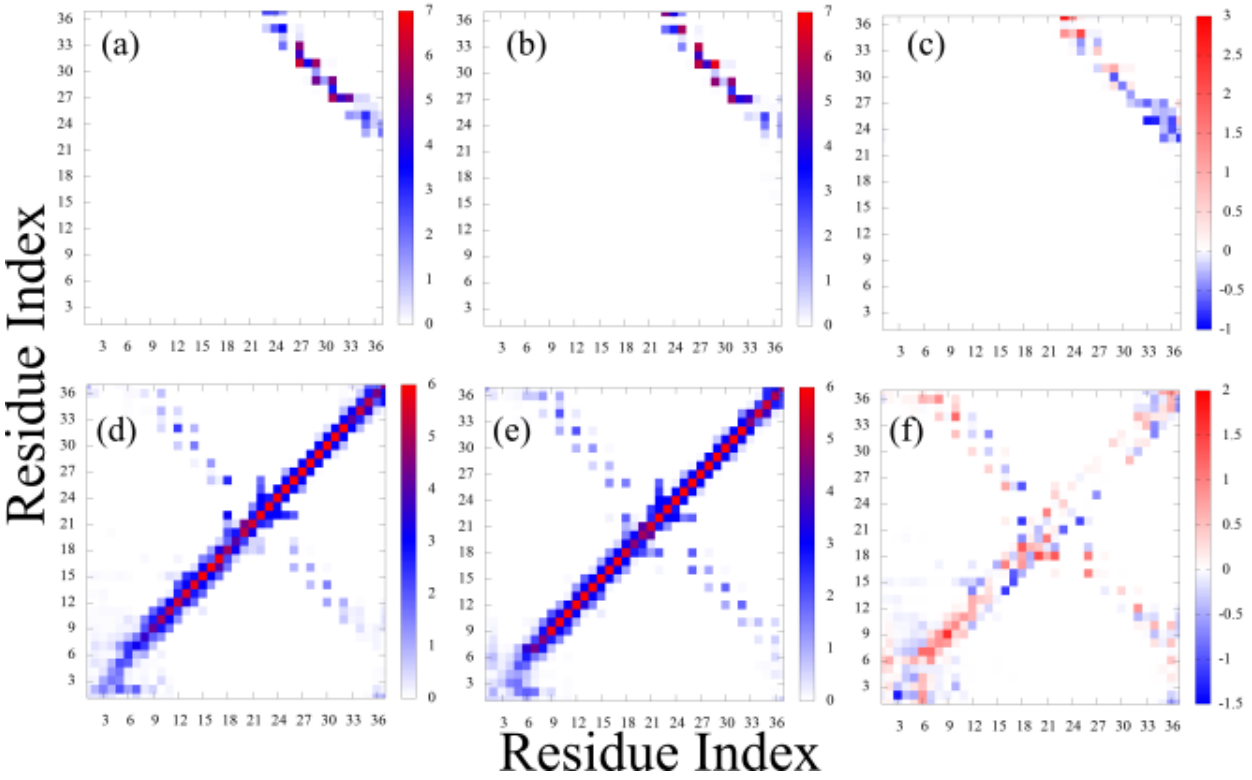

Figure SF4: Map of packing contacts, i.e., contacts between residues located on chains on different protofibrils for the (a) control and (b) in presence of SK9 of the fibril model 2F4L. The average number of such contacts are shown. The difference between the two systems is shown in (c). The corresponding maps for contacts between residues on chains on different layers, i.e., stacking contacts, are shown in (d)-(f).

The effect is less obvious for the stacking or intrachain hydrogen bonds. However, we observe an increase in contacts involving the N-terminal residues T4-L16, while such involving the C-

terminal residues S20-Y37 decrease or shift more to off-diagonal contacts, see **Supplemental Figure SF4d-f**. This is consistent with the observed stabilization of the N-termini of the chains. As we find a slight increase in the number of intrachain contacts when SK9 is interacting with the 2F4L amylin fibril, increasing from 153(1) to 155(1), we conjecture that the main reason for the weak stabilization of this fibril geometry by SK9 is due to stabilization of the fold-geometry of the chains.

A characteristic of amyloids is the polymorphism of the resulting fibrils, and the virus proteins may change the amylin fibril stability differentially depending on the polymorph. Hence, we also evaluated the effect of SK9 on a second fibril model, resolved in 2020 by Gallardo et. al[44] and deposited in the PDB under identifier 6ZRF. Simulations of this fibril model were also chosen by us to compare the effect of SK9 on fibril stability with that of the FI10 virus protein fragment. PDB-files of start and final configurations are again available as **supplemental material**.

The SK9 segments form 238 contacts (about 30 contacts per chain) initially with amylin chains in the 6ZRF fibril model, which is slightly less than in the 2F4L fibril. Again, these contacts rapidly decrease in the first 10 ns before the number of contacts stabilizes to 97(16) (about 40% of the initial number of contacts) over the last 100 ns. The binding free energy between SK9 and the 6ZRF amylin model is -31.4(4.4) kJ/mol, which is larger in magnitude than the 2F4L fibril. However, contacts are formed with similar residues as in the case of the 2F4L fibril, see **Figure 7b**: residues N14-V17 (centered around F15), N21, F23, L27 to T30 (centered around L27), and with highest probability to Y37. As for the 2F4L fibril these contacts result mostly from hydrophobic interactions, but also from π-π stacking (involving residues F15, F23, L27, S29 and Y37), or transiently formed hydrogen bonds (N14@O-SK9:Y5@HN, L16@O-SK9:Y3@HN,

F23@O-SK9:Y3@HN, L27@O-SK9:Y3@HN and Y37@O-SK9:S1@H3). The net-effect is again a stabilization of the amylin fibril, see the reduced flexibility of residues in the RMSF plot of **Figure 8b** and a reduction in RMSD compared to the control that is more pronounced than for the 2F4L fibril geometry, see **Figure 9b**. For residues N14-V17, L27-T30 and Y37, increase these contacts with SK9 the frequency of stacking contacts between successive layers when compared to the control, see, for instance, in **Supplementary Figure SF6 (f)** residue N14 forming hydrogen bonds between its side chain carboxamide and other N14 residues in the protofibril. On the other hand, the interaction of SK9 with residues N21 and F23 strengthen the packing interactions between the two protofibrils. Residue F23, interacts with the hydrophobic core formed by residues L27-T30 and Y37 on the opposite protofibril which in turn brings the protofibrils closer together resulting in tighter packing. That SK9 stabilizes mainly packing of the protofibrils, avoiding the sliding of the protofibrils sometimes seen in the control simulations, is also confirmed by visual inspection of the final configurations, some of them shown as insets in **Figure 9b**.

As a result of this stabilization the reduction in solvent accessible surface area (SASA), resulting from interaction with the SK9 peptides, is more pronounced for the 6ZRF amylin fibril than for the 2F4L fibril model. This is also observed even when including the first seven residues, see **Table 4**, but again with little difference between hydrophobic and hydrophilic residues. Unlike for the 2F4L fibril, we also find a pronounced reduction in the packing distance (4.8(0.4) Å versus 5.9(1.4) Å in the control), which, however, is not seen in the distance between layers (3.0(0.2) Å versus 2.9(0.2) Å in the control), see **Table 4**. The differences in SASA values are consistent with a change in packing free energy of $\Delta\Delta G$ = -44.9 (49.1) kJ/mol between the two protofibrils, and $\Delta\Delta G$ = -41.5 (34.4) kJ/mol in stacking free energy between two layers, see **Table 4**. The lower binding free

energies result from an increase in the number of packing contacts and layer-wise stacking contacts and hydrogen bonds, see **Table 4**. But note also the additional intra chain hydrogen bond observed in presence of SK9 that further stabilizes the amylin chain folds. As for the 2F4L fibril model, we find that presence of SK9 leads to a decrease in the number of different residue pairs that form packing hydrogen bonds: 15 such pairs contribute at least 1% in the control, while in presence of SK9 the number is reduced to five. The F23-A25 bond is dominant in both cases and contributes to about 70% of the packing hydrogen bonds. Interestingly, instead of the many kinds of transiently formed packing hydrogen bonds in the control, we find in the presence of SK9 a strong presence of N21-Y37 pairs. These pairs contribute 19% of the packing hydrogen bonds (instead of 2% in the control), and almost 90% of packing hydrogen bonds are of this type. As a consequence, the map of packing contacts in **Supplemental Figure SF5b** is more focused on contacts between residues in segment S20-A25 on one fold with residues N35-Y37 on the opposite fold than seen for the control (see **Supplemental Figure SF5a,** with the difference shown in **SF5c)**. Similarly, the frequency of stacking contacts, especially such involving residues A8-N14 also increases with the binding of SK9, see **Supplemental Figure SF5d-e**.

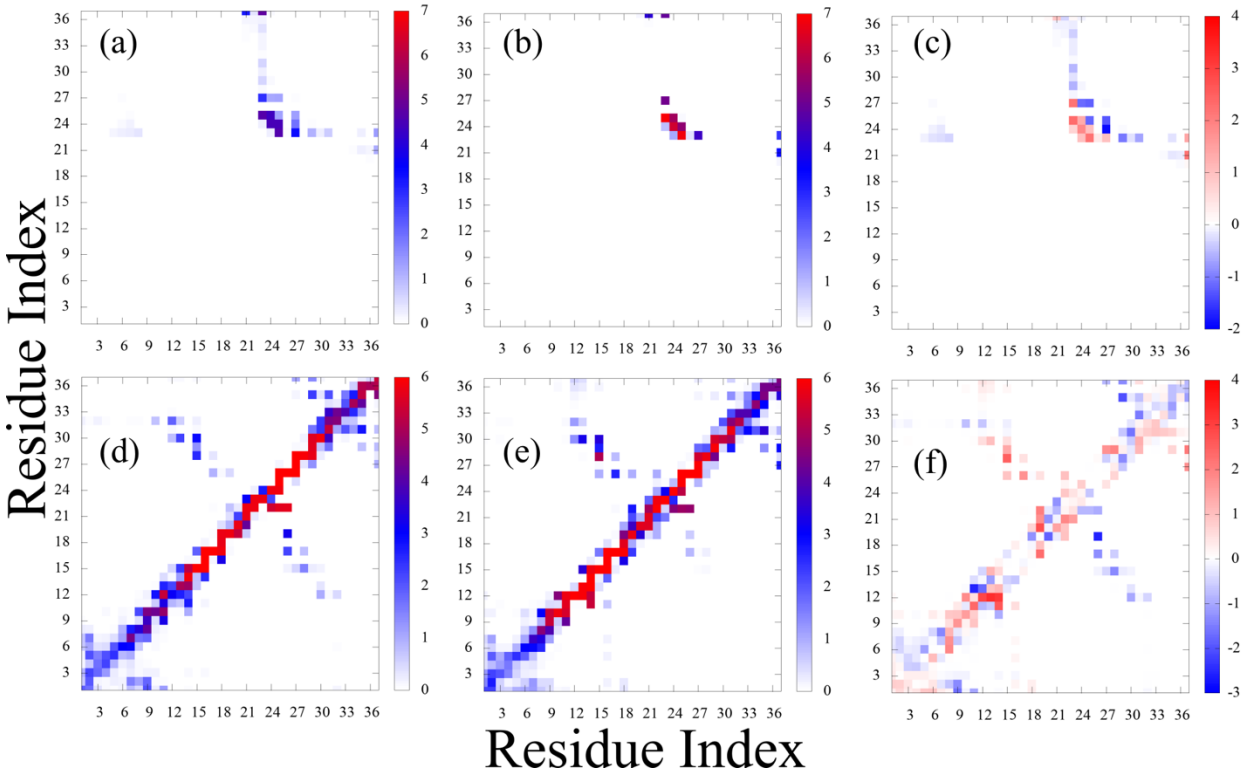

Figure SF5: Map of packing contacts, i.e., contacts between residues located on chains on different protofibrils in the fibril model with PDB-ID 6ZRF. Shown are maps for the (a) control and (b) in presence of SK9. Shown are the average number of such contacts. The difference between the two systems is shown in (c). The corresponding maps for contacts between residues on chains on different layers, i.e., stacking contacts, are shown in (d)-(f).

These interactions stabilized the N-terminal β-sheets however, the effect is less pronounced than for the packing and goes with a free energy raising twisting of these sheets. Hence, the increased frequency of packing and stacking contacts is consistent with the MMGBSA estimates which indicate that in presence of SK9 both elongation and packing are favored more than in the control, with the effect slightly more pronounced for the packing of the protofibrils.

Comparing the effect of FI10 with SK9 on the 6ZRF fibril, we note that the FI10 segments form 229 contacts (29 contacts per amylin chain) in the start configuration, which is fewer initial contacts than SK9. However, these contacts are more stable, and on average 139(6) contacts (about 61% of the original number) are observed over the last 100 ns, leading to a binding free energy between FI10 and amylin of -29 (3) kJ/mol that is only marginal lower than for SK9. The residue-wise distribution of contacts in **Figure 7b** is broader than for SK9. Binding sites such as R11-A13 (centered around L12) and H18 are observed more frequently while F23 and L27 have less pronounced peaks. Residue Y37 has an even higher binding probability to FI10 than to SK9. These contacts are again formed by hydrophobic interactions, π-π stacking and transiently formed hydrogen bonds (with N14@O-SK9:Y5@HN, L16@O-SK9:Y3@HN and L27@O-SK9:Y3@HN; and L16@O-SK9:Y3@HN replaced by L16@O-FI10:K2@HN, F23@O-SK9:Y3@HN by F23@O-FI10:G6@HN, and Y37@O-SK9:S1@H3 by two new ones: Y37@O-FI10:F1@HN and Y37@HN-FI10:F1@O). Formation of the additional hydrogen bond leads to the larger binding probability for residue Y37. FI10, unlike SK9, has a negatively charged residue that may reduce the flexibility of N-terminal residues by interacting with the positively charged R11. Similarly, interaction of the negatively charged residue on FI10 with H18 could reduce fibril destabilizing stress on the chain geometry appearing when the histidine is in the charged state.

Overall, we see a stronger interaction between FI10 and the fibril than between SK9 and the fibril. The RMSF plot of **Figure 8b** indicates that the resulting reduction in residue flexibility, when compared to the control, is slightly larger than for SK9, indicating larger stabilization of the fibril. This observation is supported by **Figure 9b** where the RMSD is lower than for SK9 binding to the fibril. Visual inspections of the final configuration, shown as inset of the figure, suggests that

similar to SK9, the effect of FI10 on fibril stability is again mainly by stabilizing packing, and no sliding of the protofibrils was observed.

Table 4: Various quantities averaged over the last 100 ns of three trajectories in simulations of the amylin 6ZRF fibril model in absence or presence of SK9 or FI10.

	Control	w/ SK9	w/ FI10
Total SASA (Å^2)	12779 (112)	12040 (267)	11861 (284)
Hydrophobic SASA (Å^2)	6451 (160)	6090 (85)	6063 (263)
Hydrophilic SASA (Å^2)	6328 (68)	5950 (265)	5798 (129)
Packing distance (Å)	6 (1)	4.8 (4)	4.4 (1)
Stacking distance (Å)	2.9 (2)	3.0 (2)	2.9 (2)
Packing contacts	54 (4)	59 (5)	62 (2)
Stacking contacts	503 (10)	537 (14)	525 (13)
Intrachain contacts	1254 (2)	1255 (22)	1256 (13)
Packing hydrogen bonds	3 (1)	2 (1)	2 (1)
Stacking hydrogen bonds	134 (4)	139 (5)	143 (7)
Intrachain hydrogen bonds	22 (0)	24 (1)	25 (2)
Packing free energy (kJ/mol)	-152.6 (57.2)	-197.5 (39.3)	-222.6 (24.2)
Stacking free energy (kJ/mol)	-620.1 (38.5)	-661.6 (29.6)	-624.3 (50.9)

Consistent with this assumption is that the reduction in solvent accessible surface area upon interaction with the viral protein fragment is about 180 Å^2 larger for FI10 than for SK9, when ignoring the disordered first seven residues. The additional reduction of SASA results mostly from hydrophilic residues, see **Table 4.** Packing distance (4.4 (1) Å) and the inter-layer distances (2.9 (2) Å) are likewise smaller than in the case of SK9, indicating that the larger stabilization of the amylin fibril by FI10, when compared to SK9, results from increased packing and stacking interactions. This can be also seen from our MMPBSA approximations of packing and stacking free energies which shows that packing of the protofibrils in the presence of FI10 is more favorable by $\Delta\Delta G$ = -70.0 (43.9) kJ/mol, and the stacking of layers by $\Delta\Delta G$ = -3.6(45.2) kJ/mol per chain. The large standard deviation in the stacking free energy difference makes it difficult to compare

these results with that of SK9, but it appears that, unlike for SK9, the stabilization of the fibril is mostly due to that of improving the packing of the protofibrils. This is consistent with the larger number of packing contacts, exceeding that seen in control or when SK9 interact with fibril. On the other hand, differences between SK9 and FI10 are marginal for the stacking contacts and hydrogen bonds, see **Table 4**. However, similar to SK9, presence of FI10 leads to a reduction in the number of packing hydrogen bond forming residue pairs from 15 in the control to four pairs, with the N21-Y37 pairs now contributing 23% of the packing hydrogen bonds, and the F23-A25 hydrogen bond contributing 72%. Hence, 95% of packing hydrogen bonds result from only two types of hydrogen bonds, see also the map of packing contacts in **Supplemental Figure SF6a-c**. While we also see, an increase in stacking contacts, involving residues A8-N14, see **Supplemental Figure SF6d-e**, the fibril-stabilizing effect is even more than for SK9 due to enhancing the packing of the two protofibrils.

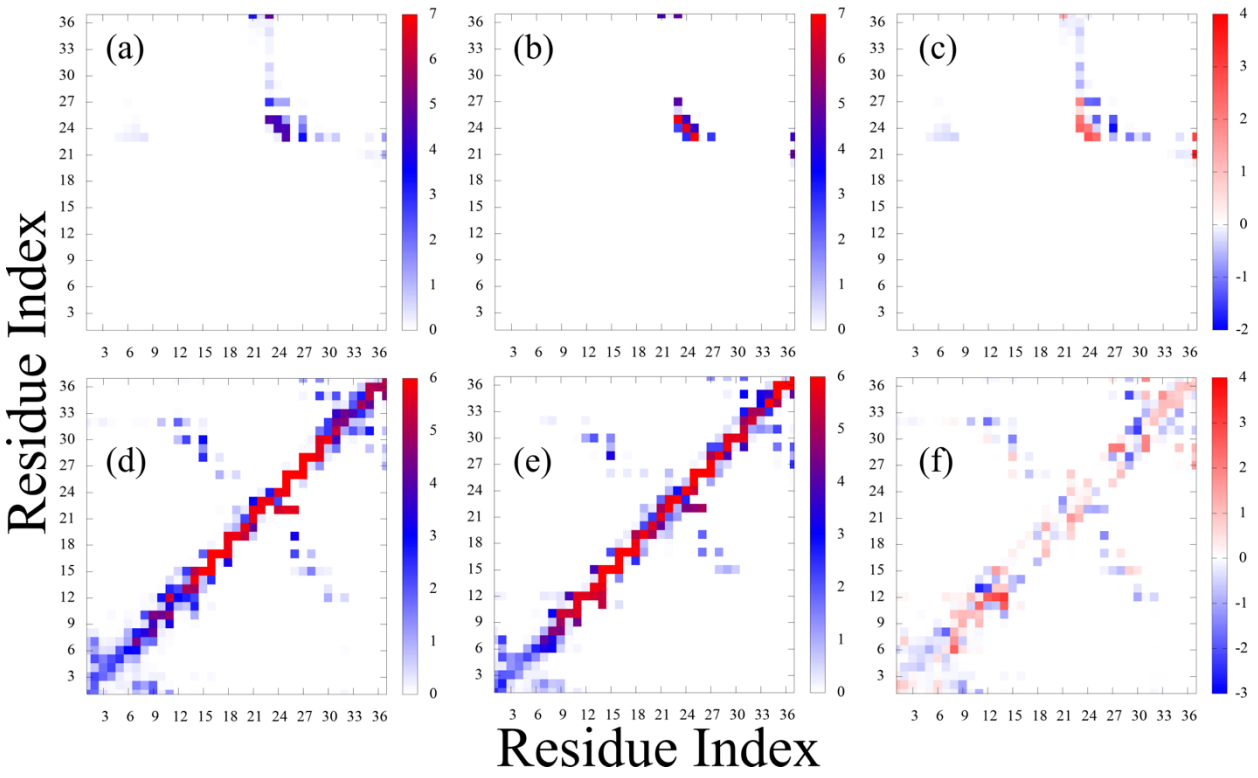

Figure SF6: Map of packing contacts, i.e., contacts between residues located on chains on different protofibrils in the fibril model with PDB-ID 6ZRF. Shown are maps for the (a) control and (b) in presence of FI10. Shown are the average number of such contacts. The difference between the two systems is shown in (c). The corresponding maps for contacts between residues on chains on different layers, i.e., stacking contacts, are shown in (d)-(f).

How do our results depend on our simulation set up? For instance, both virus protein fragments have in our simulations a NH_3^+-group at the N-terminus and a $CONH_2$-group at the C-terminus. This is due to reduced electrostatic interactions between the opposite charges at the termini. In order to test how our results depend on the choice of end group, we have also simulated a system where FI10 is not capped at the C-terminus, i.e., ends with a COO^- group. We compare in supplemental figures **SF7** the RMSD as function of time for the control and the amylin fibril interacting with the two differently capped FI10 peptides. In both cases, the RMSD is lower than for the control, and therefore the values do not seem to depend on the end-group.

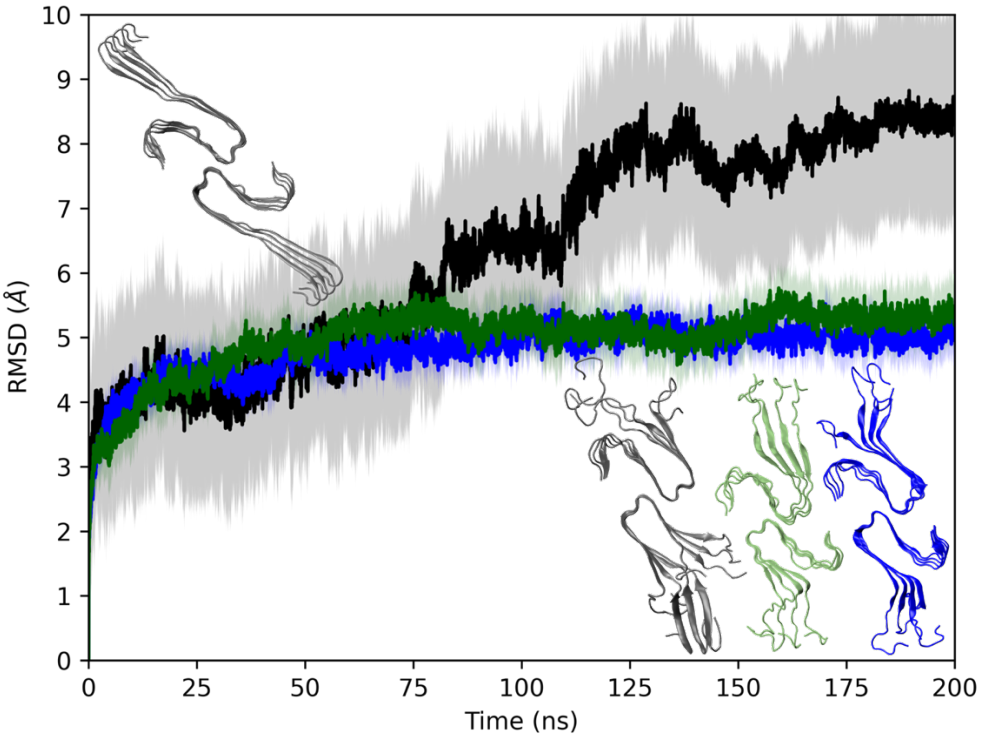

Figure SF7: RMSD to the start configuration as function of time for the fibril model 6ZRF. The RMSD is calculated over all backbone atoms in residues 8-37 of all chains in the respective fibril model. Black curves are from the control simulations while green curves are from data measured in simulations where FI10 is present and has a C-terminal end group COO-. Similarly, blue curves mark the case of FI10 with end group $CONH_2$ interacting with the amylin fibril. The standard deviation of the averages is shown shaded. The start configuration (top/left) and representative final configurations (right/bottom) of the amylin fibril models are shown as insets.

However, in the RMSF plot of **supplemental figure SF8** values of the FI10 peptide with uncapped

C-terminus are higher than for the capped one, but still lower than the control.

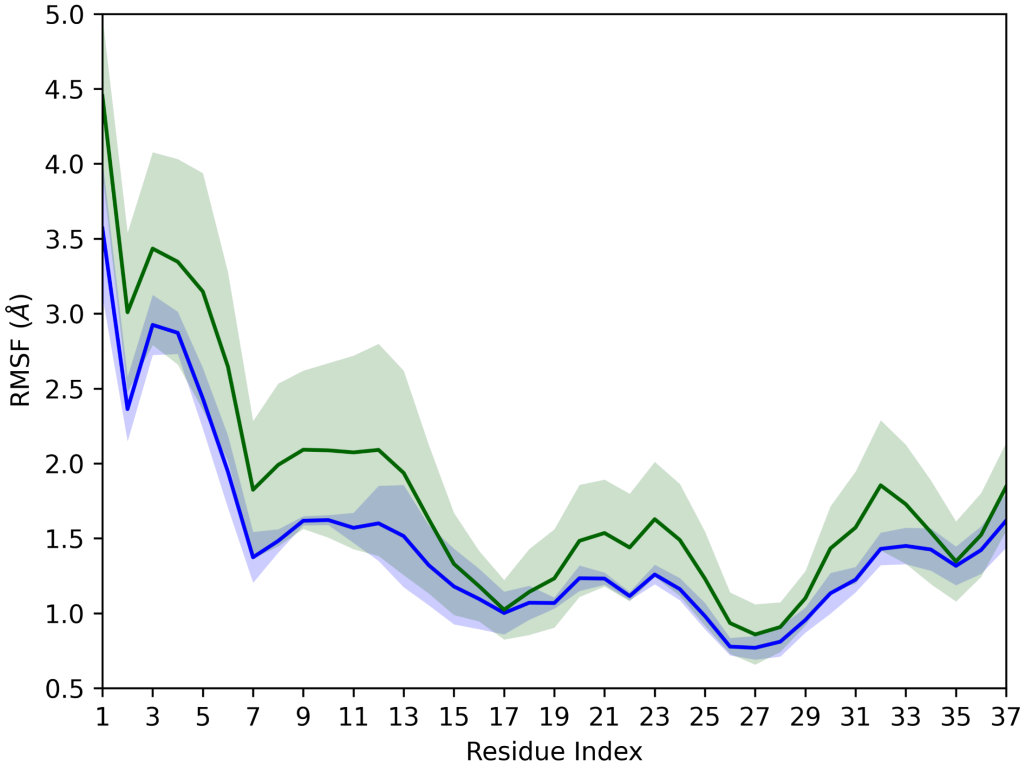

Figure SF8: Residue-wise RMSF for the fibril model 6ZRF in presence of FI10 with COO- (green) and $CONH_2$ (blue) end group. Shaded regions mark the standard deviation of the averages.

Other quantities such as the SASA, 12360(502) $Å^2$, are closer to the values found for the control, 12779 (112) $Å^2$, than for the fibril in presence of the capped FI10 peptides, 11861(284) $Å^2$. Unlike for the capped peptide, the differences result mostly from hydrophilic residues. Only residue 8-37 were considered in calculating the above SASA values. When including the disordered first seven residues the values for control, 16848 (257) $Å^2$, and the fibril in presence of the uncapped peptide, 16834(459) $Å^2$, agree within the error bars, while still lower for the fibril in presence of the capped FI10, 16283(577) $Å^2$. This may be because the uncapped peptide forms more compact configurations as its average end-to-end distance of 20.6(9) Å is smaller than the 23(1) Å of the capped FI10. Therefore, the uncapped peptide binds less tightly to the amylin fibril than the capped one. This can be seen with the number of contacts in the last 100 ns being only about 116 (6), i.e.,

51% of the original number of contacts seen for the uncapped FI10 versus 139(6), i.e., 61% for the capped peptide. The residue-wise binding frequencies in **supplemental figure SF9** show a similar, but broader, distribution as for the capped peptide, with for the N-terminal residues K1-H18 less binding propensity.

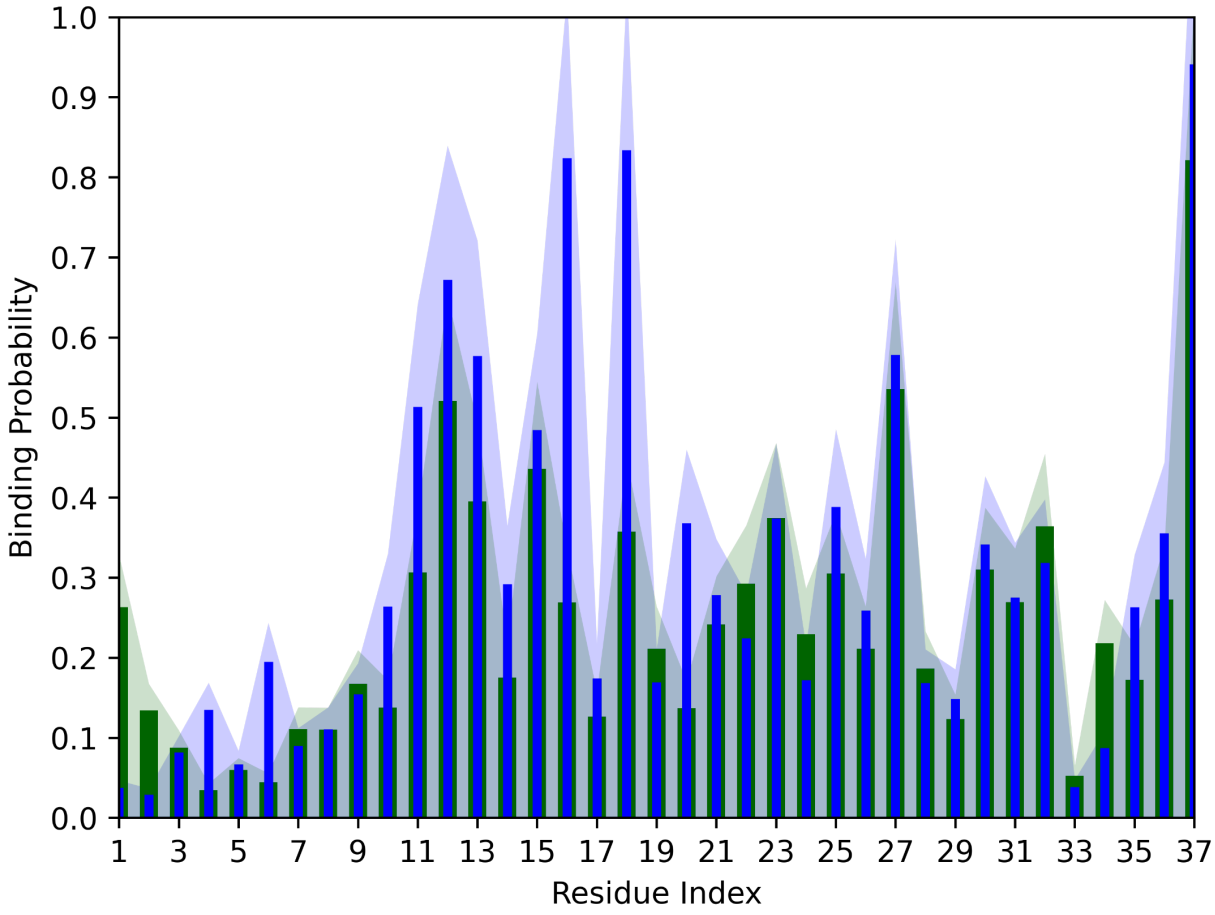

Figure SF9: Residue-wise frequency of contacts for the fibril model 6ZRF with FI10 having either COO- (green) or $CONH_2$ (blue) end group. Shaded regions mark the standard deviation of the averages.

Correspondingly, we find that the difference in binding free energies, $\Delta\Delta G$ = -10.5 (2.3) kJ/mol, resulting from the different end groups, indicates less of an interaction between the uncapped virus protein fragments and the amylin fibril. Hence, we conclude that capping of the termini reduces

self-interaction in the FI10, leading to more stretched conformations which in turn interact more strongly with the amylin fibril. This effect, however, does not seem to reduce the overall stabilization of the fibril.

Conclusions

Using extensive molecular dynamics simulations, we have studied the effect of two virus protein fragments from the Envelope protein (SK9) and from the Spike protein (FI10) of SARS-COV-2 on the ensemble of amylin monomer conformations, and on the stability of amylin fibrils. Such interactions may be correlated with the observed onset of type-2 diabetes following COVID-19.[33–36] While both virus protein fragments bind to the amylin monomer structure, we do not find the induced shift toward more aggregation-prone conformations that we saw previously in our studies with Serum Amyloid A[37] and α-synuclein[38]. Unlike these proteins amylin has, even as a monomer, a more defined structure, and the mostly helical fold appears to be stabilized by the presence of SK9 or FI10. Indications for such a protective effect seems to be seen also in experiments by the Huang Lab at HUKST that are currently analyzed (Jinqing Hiuang, private communication).

However, presence of amylin aggregates, proposed to cause symptoms of type-2 diabetes, can also be raised by stabilizing existing fibrils, shifting the equilibrium from functional monomers toward the toxic amyloids. We indeed see such stabilization of amylin fibrils by the viral protein fragments. Similar to what we found in our previous work, this stabilizing effect depends on the fibril model. Hence, as also observed by us earlier for α-synuclein[38], interactions with the viral protein fragments may shift the equilibrium between various fibril polymorphs. Fibril stabilization is observed for both SK9 and FI10 and depends only little on details of our simulation set up. For instance, the uncapped peptide binds by about 10 kJ/mol less tightly to the amylin fibril than the

capped one, leading to different values in the measured quantities, without changing qualitatively the picture. The stabilization of fibril geometry is mainly by enhancing the packing of protofibrils and less by encouraging elongation of fibrils. Interestingly, the effect is stronger for FI10. This segment unique is for SARS-COV-2 and cleaved from the spike protein by the enzyme neutrophil elastase, released from neutrophils during acute inflammation. In vitro, the FI10 fragment forms amyloids.[40] While not yet supported by experimental evidence, we speculate that SARS-COV-2 infections, often causing chronic inflammation, increase enzymatic cleavage of the spike protein, releasing in some cases amyloidogenic fragments such as FI10. These fragments could then cross-seed amylin fibrils which in turn may contribute to an onset of type-2 diabetes.

Comparing our results with earlier work we find as a common theme that small SARS-COV-2 protein fragments (as potentially derived by cleavage during infection-cause inflammation) can seed aggregation of amyloidogenic human proteins, but that this effect depends both on the viral fragment and the structure of the fibril polymorph.

Acknowledgements

Our simulations were done using the SCHOONER cluster of the University of Oklahoma, XSEDE resources allocated under grant no. MCB160005 (National Science Foundation), and TACC resources allocated under grant no. MCB20016 (National Science Foundation). We acknowledge financial support from the National Institutes of Health under grant no. GM120634. We thank Asis K. Jana for the help in the early stages of this project, mainly setting up and running the 2F4L fibril simulations and early parts of the trajectories of amylin monomers interacting with SK9.

Chapter 4 - Differential effects of SARS-CoV-2 amyloidogenic segments on the aggregation and toxicity of human islet amyloid polypeptide within membrane environments

To further explore the effect of SARS-CoV-2 amyloidogenic segments, SK9 and FI10, had on amylin, or human islet amyloid polypeptide, aggregation our collaborators, Dr. Jinqing Huang's group, from The Hong Kong University of Science and Technology performed in-vitro experiments of amylin in the presence and absence of SK9 or FI10 within a sodium dodecyl sulfate (SDS) simulated membrane environment. The experimental work was supported by molecular dynamics simulations of amylin in the presence of SK9 or FI10, which I, myself, performed and analyzed. The collaboration resulted in the publication of the journal article, "Differential effects of SARS-CoV-2 amyloidogenic segments on the aggregation and toxicity of human islet amyloid polypeptide within membrane environments", in the International Journal of Biological Macromolecules, 283 (2024) 137930 by Jianing Zhang, Vince St. Dollente Mesias, Andrew D. Chesney, Vignesh K. Anand, Xianzhen Feng, I-Ming Hsing, Ulrich H.E. Hansmann, Jinqing Huang[71]. The following chapter highlights the key experimental findings as well as the results of the molecular dynamic simulations performed.

To evaluate the effects of SK9 or FI10 on amylin aggregation within a SDS membrane environment various structural characteristics methods were utilized. Namely, circular dichroism (CD) spectroscopy, one-dimensional proton nuclear magnetic resonance (1D ^{1}H-NMR), and atomic-force microscopy (AFM). From the CD experiments there were clear signal differences between amylin with SK9 or FI10 in the presence and absence of SDS correlating to differences in secondary structure. In the absence of both fragments and SDS, the CD spectra of amylin indicated

the formation of β-sheet structures following one day of incubation. However, in the presence of SDS amylin was shown to maintain α-helical and random coil conformations as shown in the amylin monomer structure deposited in the Protein Data Bank under the ID 2L86, which was the start structure utilized for our previous molecular dynamic simulations. Interestingly, in the presence of SK9 and SDS amylin showed immediate changes in secondary structure compared with amylin only in SDS. These spectra showed an immediate shift towards β-sheet structures. In the presence of FI10 and SDS, the effect was less pronounced and indicated the presence of α-helical and β-sheet confirmations after 1 day of incubation. The CD spectra of amylin in the presence of SK9 or FI10 without SDS was also taken. These spectra indicated that the α-helical structures were maintained by both fragments over the 1-day incubation period.

Using 1D ^{1}H-NMR, intermediate confirmations of amylin with and without SK9 and FI10 in the presence of SDS were characterized. The resulting spectra indicated that there were distinct conformations due to the interactions of SK9 and FI10 with amylin. It was purposed that both SK9 and FI10 were able to promote aggregation, however the misfolding was facilitated by an off-pathway mechanism. This mechanism produced discrete intermediates that were stabilized by the viral peptides and not observed in the samples of amylin by itself. To further distinguish the morphological differences indicated by the CD and NMR spectra, AFM was used. It was shown that in the presence of SK9 and SDS, amylin was able to form long, interconnected 'root-like' fibrils. Suggesting that SK9 facilitates the rapid formation of small amylin aggregates that grow into elongated fibrils via cross-linking. On the other hand, in the presence of FI10, the formation of mature, full-length fibrils was inhibited. Instead FI10 stabilized smaller oligomer confirmations that were long lasting.

To examine the effects that amylin in the presence of SK9 or FI10 has on membrane toxicity, a fluorescence leakage assay was performed with small unilamellar vesicles. From this assay, it was noted that the system of amylin with FI10 induced the most leakage. While the systems with SK9 and amylin by itself, showed a comparable trend and had less leakage as compared to the FI10 system. These results suggest that amylin oligomer species, stabilized by the presence of FI10, lead to higher lipid toxicity, compared to amylin fibrils that formed in the presence of SK9. To further explain the potential cytotoxic effect of the amylin-SK9/FI10 species, a MTT assay was utilized to assess Human Embryo Kidney (HEK 239 T) cell viability based on cellular metabolism. The performed assays indicated decreased cell viability in all cases. However, there was a concentration dependence effect observed for SK9 and amylin. At 10 μM, the presence of SK9 significantly reduced the cell viability compared to amylin by itself, while at 25 μM little to no substantial change in cell viability was observed. FI10 did not show this concentration dependance and was shown to significantly decrease cell viability at both 10μM ($p < 0.01$) and 25 μM ($p < 0.05$). This difference in cell viability may be attributed to the formation of oligomers of amylin as was observed by AFM analysis. Overall, the work performed indicate that SK9 and FI10 interact differentially with amylin in the membrane environment, and influence amylin morphology and impact its cytotoxicity and impact on cellular processes.

Molecular dynamics simulations were performed to explore the possible interactions between amylin and the two viral fragments, SK9 and FI10. We began our investigation by simulating an amylin monomer in the presence or absence of SK9 and FI10 for 4μs in triplicate. Building off our previous simulations, these systems started from PDB: 2L86, which exhibits helical structure. In **Figure 1a**, we show the average intrachain contacts found with the amylin monomer over the

course of the 4μs trajectory. From this figure, we note a loss of contacts in the control simulation at around~1.5μs, compared with the simulations with the viral fragments present. Over the course of the simulations, those in the presence of either viral fragment showed slightly higher contacts. To get a better understanding of how the amylin monomer structure is changing with respect to its initial structure, native contacts, or contacts that are initially present, were calculated, **Figure 1b**. From this figure we note a decrease in the native contacts of the control simulation at ~ 1.5μs, which begins to hover around 10 of the original contacts remaining. While in the presence of SK9 and FI10 the contacts remain around 30 after an initial drop that was observed in all cases. To further explore the effects the viral fragments had on the structure of the amylin monomer, the secondary structure was calculated. In **Figure 1c**, we show the percentage of residues that exhibit helical character over the trajectory. Here again we note a decrease for the control simulation, indicating the loss of native contacts observed in **Figure 1b** can be explained by the loss of helical structure in the control simulations. Again, the structures in the presence of SK9 and FI10 maintain their helicity. In **Figure 1d**, we show the helix probability per residue for all simulations, calculated over the final 1μs. Clearly, we see that the residues of amylin are more likely to maintain their helical nature while in the presence of the viral segments. We also note that this effect seems to be more pronounced in the presence of FI10 compared with SK9. As these simulations were performed in an aqueous environment without SDS, our results are consistent with the experimental CD spectra of amylin in the presence and absence of SK9 and FI10 without SDS.

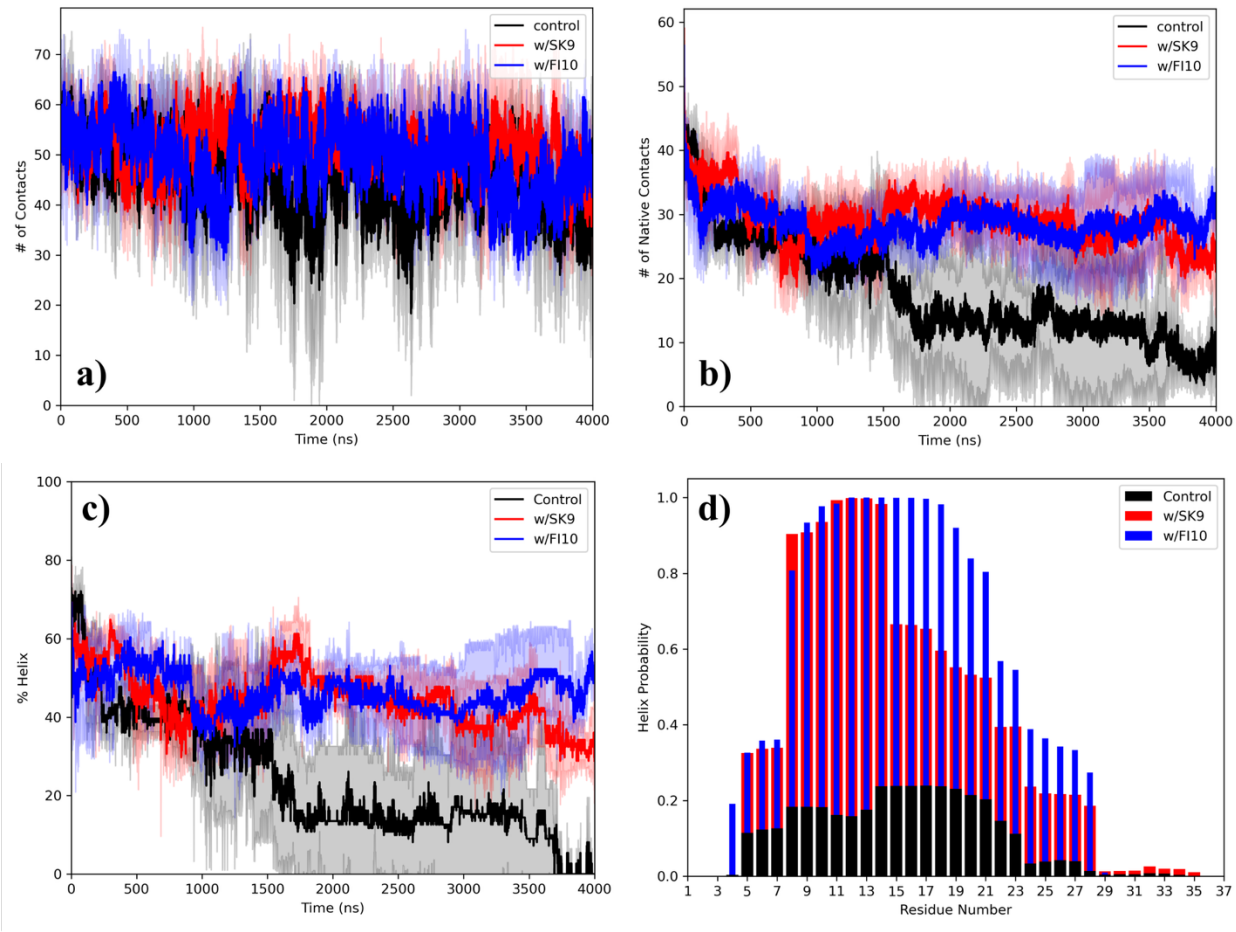

Figure 1: **a)** Average number of amylin intrachain contacts in the absence (black) and presence of SK9 (red) and FI10 (blue). Shaded regions indicate the standard deviation. **b)** Average native contacts maintained over the simulations in the absence (black) and presence of SARS-COV-2 protein fragments (red = SK9, blue = FI10)**. c)** Percentage of helical structure observed in amylin monomer. (d) Average residue-wise helicity probability of amylin monomer calculated over the final 1 μs**.**

To evaluate the interactions of SK9 and FI10 on equilibrated and disordered amylin monomer structures, another set of simulations were performed. The start structures for these simulations were taken from the above control simulations after 3μs or later. These structures were then docked with SK9 and FI10 and were simulated for 1μs. Over the course of these simulations, transient β-strand confirmations were observed. The behavior of each trajectory varied, as shown in **Figure 2**; however, once a β-strand confirmation was formed it was stabilized by the presence of SK9 and

FI10. This is illustrated by the %sheetness of V2 shown in **Figure 2**. Our results suggest that in the presence of SK9 or FI10, they will stabilize the α-helical confirmations of amylin and will stabilize the strand-like conformations when present. However, SK9 or FI10 by themselves would not actively induce the formation of such aggregation-prone conformations of amylin.

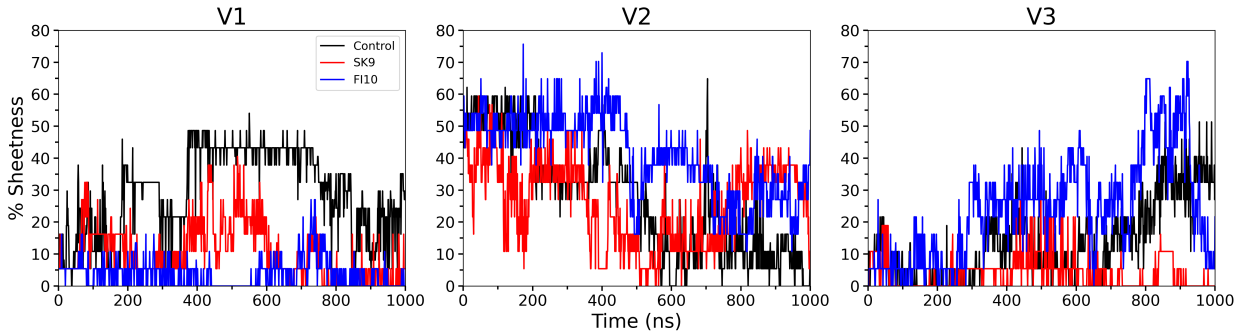

Figure 2: Percentage of sheetness as a function of time in three trajectories (V1, V2, and V3) starting from three different disordered amylin monomer confirmations obtained from three control trajectories of the monomer after 3 μs or later.

We also investigated the effects of SK9 and FI10 have on amylin oligomeric confirmations, in short 100ns trajectories. This was performed by generating an amylin dimer model from the final structure of amylin in our second control trajectory using HADDOCK. Additionally, SK9 and FI10 were docked to the dimer in a 1:1 ratio of amylin chains to viral segments using HADDOCK, shown in **Figure 3**. The solvent accessible surface area (SASA) of the systems were calculated over the last 10ns of the simulations. In the presence of SK9 and FI10 the total SASA was 7700 ± 200 Å^2 and 7400 ± 300 Å^2, respectively. These total SASA values are roughly 1000 Å^2 larger than in the absence of these peptides, 6600 ± 200 Å^2. This difference was shown to be accounted for by an increase in hydrophobic surface area in the presence of the viral segments.

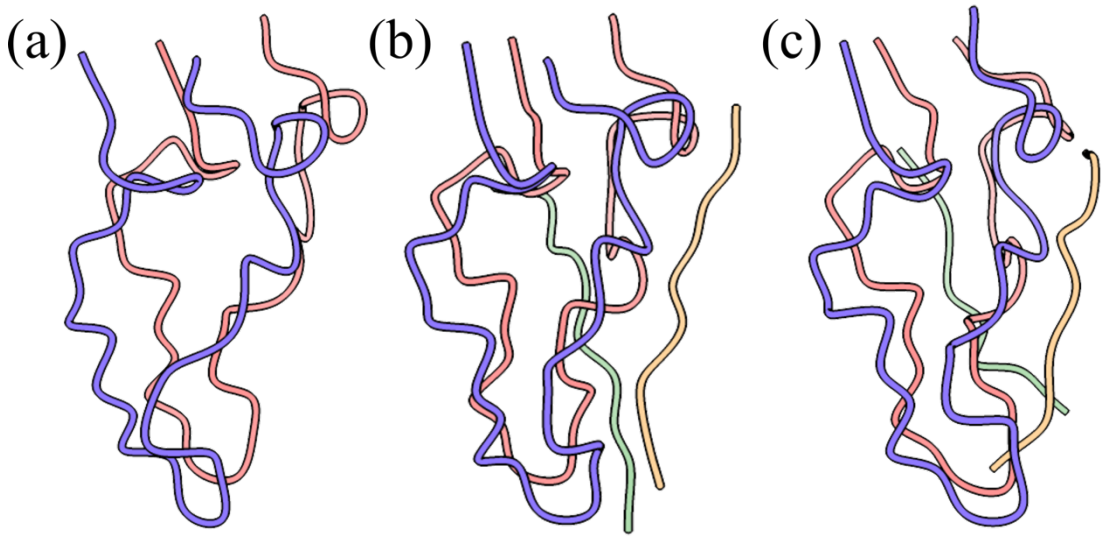

Figure 3: Amylin dimer generated from control simulation structures (a), amylin dimer docked with 2 FI10 fragments (b), and amylin dimer docked with 2 SK9 fragments (c). Amylin segments are shown in purple and pink, FI10 and SK9 fragments are shown in green and yellow.

Additionally, it was found the SK9 and FI10, differ in the way that they stabilized the chain geometry of the dimer. In the presence of FI10, more of the intrachain contacts are preserved within the chains of the dimer as compared with SK9 which showed increased flexibility of the individual chains. On the other hand, in the presence of SK9 the number of interchain contacts, or contacts between the two dimers, preserved was higher. Which may indicate why SK9 was observed to increase aggregation and elongation of amylin fibrils in vitro, and while FI10 favored shorted oligomer structures.

Chapter 5 – SARS-COV-2 Spike Protein Fragment Eases Amyloidogenesis of α-Synuclein

Our first investigations of α-Synuclein with SARS-COV-2 protein fragments began with the envelope protein fragment SK9. We investigated its effects on monomer and fibril stability, and published our results in the Journal of Physical Chemistry B in an article titled "Effect of an Amyloidogenic SARS-COV-2 Protein Fragment on α-Synuclein Monomers and Fibrils", authored by Asis K. Jana, Chance W. Lander, Andrew D. Chesney, and Ulrich H. E. Hansmann.[38] From these investigations we noted in the presence of SK9 the α-Synuclein monomers shifted toward more aggregation prone configurations that favored the rod-like fibril seeding conformations. The effects of SK9 on pre-existing or newly formed fibrils stability however were small. Following the publication of this work, an experimental group identified a potential amyloidogenic peptide segment from the SARS-COV-2 spike protein *in vitro* by proteolytic cleavage by neutrophil elastase, FI10.[19] To further evaluate the effects of this newly identified segment on α-Synuclein monomer and fibril stability, we again performed molecular dynamics simulations and compared our results with our previous simulations. Due to FI10 being a more biologically relevant peptide, the following chapter will focus on the molecular dynamic simulations performed with α-Synuclein and FI10 and their comparison with simulations in the presence of SK9. The following chapter was published in a similar form in the Journal of Chemical Physics by the author of this dissertation as the following article: SARS-COV-2 Spike Protein Fragment Eases Amyloidogenesis of α-Synuclein, J. Chem. Phys. 159, 015103 by Andrew D. Chesney, Buddhadev Maiti, Ulrich H.E. Hansmann.[72] All text and figures are taken with the permission of the publisher.

INTRODUCTION

Several neurodegenerative diseases are correlated with presence of protein aggregates in the brain, amyloids, that are characterized by a cross-beta structure. An example of such diseases is Parkinson's Disease (PD) where α-synuclein (αS) aggregates appear to be the cell-toxic agent.[73–75] It has been proposed that such amyloids may form as an immune response to an infection, rendering pathogens ineffective by entrapping them[76]. While evidence for this microbial protection hypothesis[77–79] is limited, correlations have been observed, for instance, between falling ill with COVID-19 and outbreaks of PD[80]. Because of these correlations, and SARS-COV-2 promoted αS amyloid formation *in vitro*[81–83], we have proposed earlier[38] that amyloidogenic regions on SARS-COV-2 proteins can enhance aggregation of αS. In these previous studies we investigated the interactions of the fragment SFYVYSRVK (SK9) of the Envelope protein with αS. We found that SK9 alters the ensemble of αS monomer conformations toward such that are more aggregation prone, preferentially raising the likelihood for forming the rod polymorph[84,85]. By themselves can these preliminary investigations be criticized for relying on an isolated short SARS-COV-2 protein fragment, instead of the complete viral protein where the spatial environment of the segment may change its ability to cross-seed αS. A related question is why the suspected health effects are not seen after infections by other Corona viruses that have homologous segments. However, it has been recently shown that such short fragments, derived by enzymatic cleavage of SARS-COV-2 proteins, exist in humans, and that in vitro they form amyloids[19]. Of special interest is the segment 194–203, (FKNIDGYFKI), of the spike protein as it is unique for the SARS-COV-2 virus, and as it is cleaved from the Spike protein by the enzyme neutrophil elastase. This enzyme is released from neutrophils during acute inflammation, as, for instance, caused by the infection. Motivated by these experimental investigations we have researched with extensive molecular dynamics

simulations the effect of presence of the SARS-COV-2 spike protein segment FKNIDGYFKI, which we call in the following FI10, on αS monomers and fibrils. Our goal is to demonstrate that our previous results are not an artifact of the SK9 fragment but also seen for the likely more disease-relevant and SARS-COV-2 specific FI10. For this purpose, we compare the effect that the two fragments have on αS monomers and fibrils to establish commonalities and differences. Our results let us to conjecture that viral infections raise the risk for amyloidosis when, as often in the case of SARS-COV-2, the infection causes pronounced inflammation and release of enzymes that can cleave viral proteins into in some cases amyloidogenic fragments which can cross-seed human proteins.

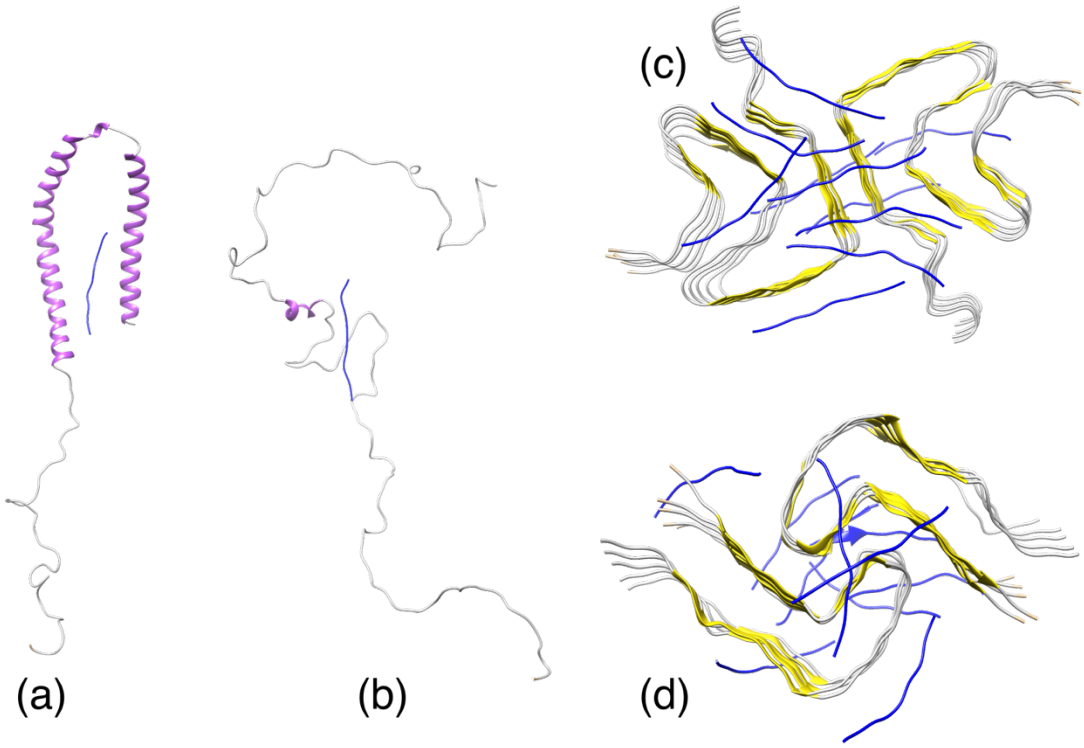

FIGURE 1: Start configurations of αS with initial binding positions of FI10: (a) monomer (PDB ID: 1XQ8), (b) heat-extended monomer, (c) rod-polymorph (PDB ID: 6CU7) fibril, and (d) twister-polymorph (PDB ID: 6CU8) fibril.

MATERIALS AND METHODS

System Preparation

Using molecular dynamics (MD) simulations we investigate how SARS-COV-2 proteins alter αS aggregation. For this purpose, we compare the effect of the ten-residue segment FKNIDGYFKI (FI10) of the Spike protein on the conformational ensemble of αS monomers and the stability of αS fibrils with that induced by the nine-residue segment SFYVYSRVK (SK9) of the Envelope protein studied by us in earlier work.[37,38] As start conformation for the αS we used either the model of micelle-bound αS deposited in the Protein Data Bank (PDB) under PDB ID: 1XQ8, or a randomized and fully-extended conformation derived by heating up the PDB conformation simulating it at 500 K for 5 ns[38]. For the fibril models we extracted decamers from the cryo-EM structures deposited in the PDB under identifiers 6CU7 (rod-like architecture) and 6CU8 (twister-like architecture).[84] In order to be consistent with earlier work[38], we add again at the N- and C-terminal a NH_3^+ and a COO^- group for both monomer and fibril models.

Simulations starting from the above described αS monomer and fibril models described above serve as control for simulations where in addition also either SK9 or FI10 peptides are present. Following Nyström and Hammarström[19] the FI10 viral fragment was derived from the structure of the SARS-COV-2 Spike protein (PDB ID: 6VXX) by extracting the segment of residues F194-I203, and capping the N- and C-terminal of this peptide by a NH_3^+ and -COO^- group. Docking FI10 segments in a ratio of 1:1 with either monomer or fibrils at binding sites predicted by AutoDock Vina[86] or HADDOCK[47,48] we obtain the initial conformations for our simulations, shown in **Figure 1**. Note that the viral protein segments are not tethered to these initial positions but move freely throughout the simulations and may detach from the αS chains. In a few cases we

extended or repeated previous simulations of SK9 interacting with αS monomers or fibrils. In these instances we followed the preparation described in our earlier work.[37,38]

Table 1: Simulated systems

System Description	Atoms	Water Molecules	Independent Trajectories	Simulation Length (ns)	Total Sampling (ns)
Monomer (PDB ID: 1XQ8)					
Control	337,169	83,670	3	1,000	3,000
w/ SK9	336,308	83,414	3	1,000	3,000
w/ FI10	336,359	83,423	3	1,000	3,000
Monomer (EXTENDED)					
Control	336,177	83,422	2	1,000	2,000
w/ SK9	336,132	83,370	2	1,000	2,000
w/ FI10	336,283	83,404	2	1,000	2,000
Rod Fibril Model (PDB ID: 6CU7)					
Control	183,222	58,098	3	200	600
w/ SK9	183,383	57,585	3	200	600
w/ FI10	215,356	68,190	3	200	600
Twister Fibril Model (PDB ID: 6CU8)					
Control	214,717	69,447	3	200	600
w/ SK9	177,583	56,525	3	200	600
w/ FI10	215,101	68,975	3	200	600

General Simulation Protocol

Following our earlier work we simulate the monomer systems with the a99SB-disp all-atom force-field[87] in combination the corresponding a99SB-disp water model, whereas the fibrils simulations rely on the CHARMM 36m all-atom force-field[50]with TIP3P explicit water[51]. Both force-field are implemented in the GROMACS package 2022 package[49] used for our simulations. Hydrogen atoms were added with the *pdb2gmx* module of the GROMACS suite[49]. The start configurations for each system were placed in the center of a cubic box with periodic boundary conditions, with

a minimum distance of 15 Å between the solute and the edge of the box. The boxes were filled with water molecules, and counterions added to neutralize the system. Na^+ and Cl^- ions are at a physiological ion concentration of 150 mM NaCl. The number of water molecules and the total number of atoms are listed in **Table 1**. The energy of each system was minimized by steepest decent for up to 50,000 steps, and afterwards the system was equilibrated at 310K for 200 ps at constant volume and an additional 200ps at constant pressure (1 atm), constraining the positions of heavy atoms with a force constant of 1000 kJ mol^{-1} nm^{-2}.

Simulations started from the above generated initial conformations (shown in **Figure 1**). A constant temperature (310 K) was maintained by a v-rescale thermostat[56] with a coupling constant of 0.1 ps, at and pressure was kept constant 1 atm by using the Parrinello-Rahman barostat[57] with a pressure relaxation time of 2 ps. By using the SETTLE algorithm[58] to keep water molecules rigid, and restraining protein bonds involving hydrogen atoms to their equilibrium length with the LINCS algorithm[59], we were able to use a time step of 2 fs for integrating the equations of motion. Since we employed periodic boundary conditions, we computed the long-range electrostatic interactions with the particle-mesh Ewald (PME) technique, using a real-space cutoff of 12 Å and a Fourier grid spacing of 1.6 Å. Short- range van der Waal interactions were truncated at 12 Å, with smoothing starting at 10.5 Å. For each system, we follow three independent trajectories differing by their initial velocity distributions. The length of the various trajectories is also listed in **Table I**. PDB-files of start and final configurations are available as **supplemental material**.

Trajectory Analysis

The molecular dynamics trajectories are analyzed with the GROMACS tools[49], VMD[60] and MDTraj software[61]. For visualization of conformations we use VMD[60]. GROMACS tools are used to calculate root-mean-square deviation (RMSD), root-mean-square-fluctuation (RMSF), radius of gyration (RGY) and solvent accessible surface area (SASA), the later quantity relying on a spherical probe of 1.4 Å radius. Contact frequencies are calculated using VMD and the MDTraj software, defining contacts by a cutoff 4.5 Å in the closest distance between heavy atoms in a residue pair. The residue-wise secondary structure propensity is calculated in VMD by the STRIDE algorithm[63]. Helicity and sheetness are defined as the percentage of residues with alpha-helical (i.e., assigned a "H" by STRIDE) or beta-strand (an "E" for extended configuration or a "B" for an isolated bridge) secondary structure in a frame of the trajectory analyzed.

RESULTS AND DISCUSSION

Monomer simulations

In previous work,[38] we established that interaction with the SARS-COV-2 Envelope protein fragment SK9 moves the ensemble of αS chain structures toward more extended and aggregation prone ones. We also argued there that these changes favor assembly into rod-like amyloids. In the present work we compare these results with that of simulations where we consider instead interaction of αS chains with the fragment FI10 of the Spike protein as this fragment is unique for SARS-COV-2 virus and is cleaved from the Spike protein under disease conditions. We remark that our results are averages over five runs, with three starting from a micelle-bound and two from an extended αS conformations (see method section). This is because we saw few differences between the two sets of runs in the last 50 ns of trajectories considered by us.

We first compare the strength with which both viral protein fragments bind to αS chains. In the start conformations SK9 has 27 contacts with the αS monomer; and FI10 forms 22 contacts. The diffusive motion of the fragments in relation to the αS chain leads to a loss of many of these contacts (on average there are for SK9 nine of the original contacts left in the final 50 ns of the trajectory, and none for FI10), but some are replaced by newly formed contacts. Consequently, the total number of binding contacts decreases more slowly, and the average number of binding contacts over the last 50 ns are 21(10) for SK9, and 5(3) for FI10. On the other hand, when calculated by the method of Ref.[65], we find binding energies of -19(4) kJ/mol for SK9 and -20(5) kJ/mol for FI10, that despite the lower number of contacts suggests a tighter binding of FI10 to the αS monomer. **Figure 2a** shows that for FI10 the persisting contacts are located in the segment A90–I112 in the C-terminus, while SK9 binds mainly to residues K21-E35 at the N-terminus, the NAC region of residues E61 to A78 and the disorganized C-terminus starting residue D119. We find that, because of these contacts, FI10 increases the flexibility of residues over the whole αS chain, see **Figure 2b**, but especially leads to an increased flexibility for the segments of residues E46 -V70 and T75-V95, i.e., the NAC and preNAC region. On the other hand, for SK9 the increase in flexibility is more narrowly restricted to the short segments where it binds strongly to the αS monomer. We remark that in the much longer simulations of Ref.[38] presence of SK9 finally also results in a higher flexibility of residues over almost the whole αS chain.

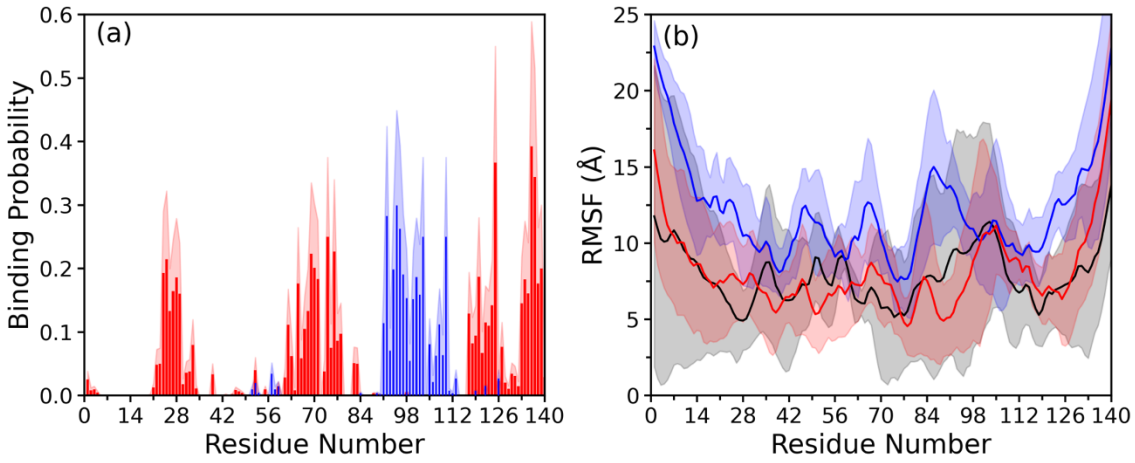

Figure 2: (a) The residue-wise normalized binding probability of the FI10 (blue) or the SK9 (red) segment to αS monomer. (b) Residue-wise mean square fluctuation (RMSF; measured in Å) obtained from αS monomer simulations in the absence (in black) and in the presence of the SK9 (red) or the FI10 peptide (blue). The RMSF values are calculated with reference to the experimentally resolved αS monomer (PDB ID: 1XQ8) considering only backbone atoms. Data are averaged over the final 50 ns of each trajectory. Shaded region represents the standard deviation of the average values defining the corresponding curves.

The net-effect of this higher flexibility is that the αS monomers are more extended and strand-like when in presence of SK9 or FI10. This can be seen in **Figure 3a** where we show the distribution of the radius of gyration (R_g), a measured for the compactness of conformations, as obtained in the last 50 ns, and averaged over all three trajectories. Interaction with the viral protein fragments shifts the ensemble towards less compact conformations. This effect is more pronounced for FI10 than for SK9 as can be also seen in the corresponding averages listed in **Table II**. The distribution of solvent-accessible surface area (SASA) in **Figure 3b** support the much larger effect that FI10 has on the ensemble of αS monomer conformations. Correspondingly we find a much lower number of contacts between residues within the αS monomers when in presence of FI10 than in the control of in presence of SK9, see **Table II**. Hence, presence of FI10 causes a pronounced shift in the ensemble of monomer conformations toward more extended, solvent-exposed and looser-

packed conformations that in this magnitude is for SK9 only observed over much larger time scales (3 μs instead of 1μs), see Ref.[38].

The decrease in the average frequency of helicity and the corresponding gain in the frequency of sheetness seen in **Table 2** indicates that the resulting conformations are more aggregation prone. The change in secondary structure is most pronounced for the N-terminal segment of residues A27–T54. Most of the known familial mutations are located in this segment assumed to be important in the early stages of αS aggregation.[88–92] In both cases is the helicity reduced from about 15% to 5%-6%, while at the same time the sheetness increases from about 8% to 12%-14% and is slightly higher for FI10. Interestingly, we find in the NAC region of residues E61-V95 an increase in both helicity and sheetness.

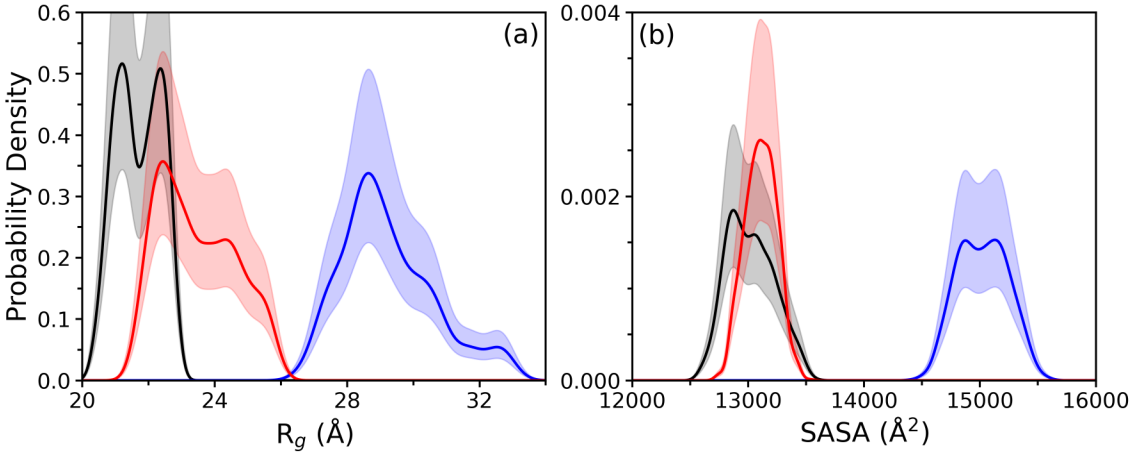

Figure 3: Probability density of (a) radius of gyration (R_g) and (b) solvent accessible surface area (SASA) of αS monomers in absence (black) and presence of the SK9 (red) and FI10 (blue) peptide. Data are averaged over the final 50 ns of each trajectory. Shaded region represents the standard deviation of the average values defining the corresponding curves.

As already observed in Ref.[38] , the shift in the αS monomer ensemble seems to be not just one toward more aggregation-prone conformations, but also favoring assembly into rod-like fibrils over such with a twister-like structure. In the rod fibril polymorph (see **Figure 1**) the segment E46-A56 forms the interface between the two protofibrils while for the twister polymorph the interface is formed by the region G68-A78. In our simulations of the αS monomer we find for the segment E46–A56 the solvent accessible surface area (SASA) raised by 90 $Å^2$ in the presence of SK9 (from 1334 (111) $Å^2$ to 1422 (108) $Å^2$), and by about 104 $Å^2$ in the presence of FI10 (to 1437 (100) $Å^2$). The difference in SASA arises in the case of SK9 almost equally from hydrophilic (48 $Å^2$) and hydrophobic residues (42 $Å^2$), while for FI10 the difference is mostly due to more exposed hydrophobic residues, (65 $Å^2$ vs. 39 $Å^2$ for hydrophilic residues). On the other hand, for the segment G68-A78 the SASA values raise only marginally from 1286 (122) $Å^2$ for the control to 1303 (85) in presence of SK9 and even decrease in presence of FI10 to 1268 (140) $Å^2$. This decrease is from hydrophilic residues (-34 $Å^2$) while hydrophobic residues are slightly more exposed by about 16 $Å^2$. For SK9 arises the difference in SASA almost equally from hydrophilic and hydrophobic residues. Hence, presence of both SK9 and FI10 leads to an exposure of solvent accessible surface (especially of hydrophobic residues) for the segment E46-A56 that is much lower or not existing for the segment G68-A78. As a consequence, association of αS chains is favored in both cases more at the segment forming in the rod-like fibril the inter-protofilament interface than at the corresponding segment in the twister-like fibril. This effect is again especially pronounced in the case of FI10 than for SK9, with FI10 even decreasing the SASA values of the segment G68-A78. On the other hand, even in the longer simulations of SK9 interacting with αS of Ref.[38] the SASA values of 1444(28) $Å^2$ for the segment E46–A56 (as measured over the last

1.5 μs of the 3 μs) barely match the values measured in the FI10 simulation already much earlier at 1μs, while for G68-A78 they further increase to 1335(46) Å^2.

Table 2: for control, SK9, FI10 average RGY, SASA, n_c, helicity, sheetness (whole range, 27-54,61-95), and binding contacts. Averages over last 50ns. Data from a previous study published in Ref[38] added separately for reference (data calculated over last 1.5 μs of 3μs trajectories).

		Control	w/ FI10	w/ SK9	Old control	Old w/ SK9
Rgy (Å)		22 (1)	29 (1)	24 (1)	22 (1)	25 (2)
SASA (Å^2)		13022 (1072)	15023 (600)	13109 (978)	13364 (937)	14293 (128)
Hydrophobic SASA(Å^2)		6893 (648)	8160 (318)	6990 (601)	7136 (587)	7685 (84)
Hydrophilic SASA (Å^2)		6128 (426)	6119 (282)	6863 (382)	6228 (354)	6592 (44)
n_c (#)		786 (9)	725 (9)	784 (7)	766 (11)	734 (26)
Helicity (%)	Residues 1-95	16 (13)	15 (9)	17 (15)	10 (6)	8 (2)
	Residues 27-54	15 (12)	6 (6)	5 (3)	4 (3)	4 (3)
	NAC region (residues 61-95)	13 (16)	21 (18)	24 (26)	14 (11)	9 (8)
Sheetness (%)	Residues 1-95	9 (4)	9 (5)	11 (9)	12 (3)	12 (3)
	Residues 27-54	8 (6)	12 (7)	14 (15)	13 (4)	17 (1)
	Residues 61-95	10 (8)	12 (17)	15 (13)	12 (6)	13 (8)
Binding Contacts		—	5 (3)	21 (10)	—	14 (7)

Hence, our monomer data confirm that alteration of the ensemble of αS monomer conformations is not restricted to the SK9 segment studied earlier by us. The net effect of the interaction between SK9 or FI10 and αS monomers is in both cases a shift toward monomer conformations that have a higher propensity to aggregate. The signal for this shift is stronger for the Spike

protein fragment FI10 which is unique for SARS-COV-2. Even more than SK9 does FI10 leads to more extended conformations with more exposed solvent accessible surface, with an exposure of hydrophobic residues favoring association into rod-like over twister-like fibrils.

Fibril simulations

Another way by which SARS-COV-2 proteins can promote amyloid formation is by raising the stability of fibril polymorphs. For this reason, we have probed in a second set of molecular dynamics simulations how SK9 or FI10 change the stability of the two most common αS fibril structures, the rod and the twister polymorphs (see **Figure 1)**. As with the monomer simulations, we compare for the two fibril polymorphs such trajectories, where SK9 or FI10 fragments bind initially to the αS chains, with the corresponding ones where the viral protein fragments are absent.

While for the rod model only 60 residues (L38-K97) out of the 140 amino acids in αS have been resolved, and only 41 residues (K43–E83) for the twister model, we decided against adding the unresolved regions as predicted by homology modeling. This is because we found in previous work[38] no qualitative differences in the behavior of the original PDB models and the ones with extended αS chains.

Initially, the SK9 peptides form about 27 contacts per chain the 6CU7 rod fibril, and the FI10 peptides form on average 33 contacts per chain. These numbers decrease quickly in the first nanosecond, and more slowly afterwards, but stay constant over the last 50 ns at 13(1) contacts per chain for SK9, and 16 (1) contacts for FI10, i.e., the number of contacts decreased by about 50% in both cases. Note that not all of these contacts appear in the start configuration: neither the

SK9 nor the FI10 fragments are tethered to the fibril, and binding contacts can both form and dissolve. The interaction between FI10 peptides and the 6CU7 rod fibril is stronger than it is between SK9 fragments and fibril, with the residue-wise distribution of contacts much broader for FI10 than for SK9 where the binding sites are localized to segments of residues H50–K60 and V71–Q79, see **Figure 4a**.

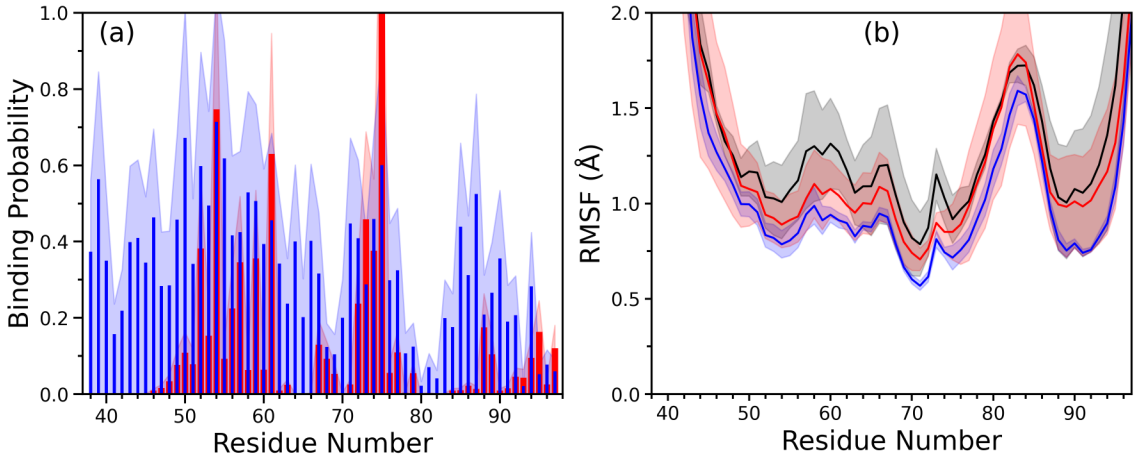

Figure 4: The residue-wise normalized binding probability of the SK9 (red) and the FI10 (blue) peptides to αS chains in the rod-like fibril model 6CU7 is shown in (a), while we display in (b) the corresponding residue-wise root-means-square fluctuations (RMSF) for αS chains (SK9: red, FI10: blue, control: black). Data are averaged over the final 50 ns of each trajectory and shaded regions represent the standard deviation of the average values defining the curves.

The binding with the viral protein fragment leads in both cases to a reduced flexibility of the αS chains, see the lower values of the residue-wise root mean square fluctuation (RMSF) in **Figure 4b.** While the overall form of all three RMSF curves is similar, residues in the 6CU7 rod fibril bound to SK9 or FI10 have lower RMSF values than the control, i.e., are less flexible, and the decrease in flexibility is closely correlated with the binding probabilities for the viral protein fragments to the αS chains in **Figure 4a**. While the RMSF distribution indicates that both SK9 and

FI10 stabilize the rod-like fibril, the effect more pronounced for FI10. Note especially the strong additional stabilization of chain geometry at the inter-protofilament interface (E46–A56), but also the stabilization of the C-terminal residues G86–K96 that is not seen for SK9.

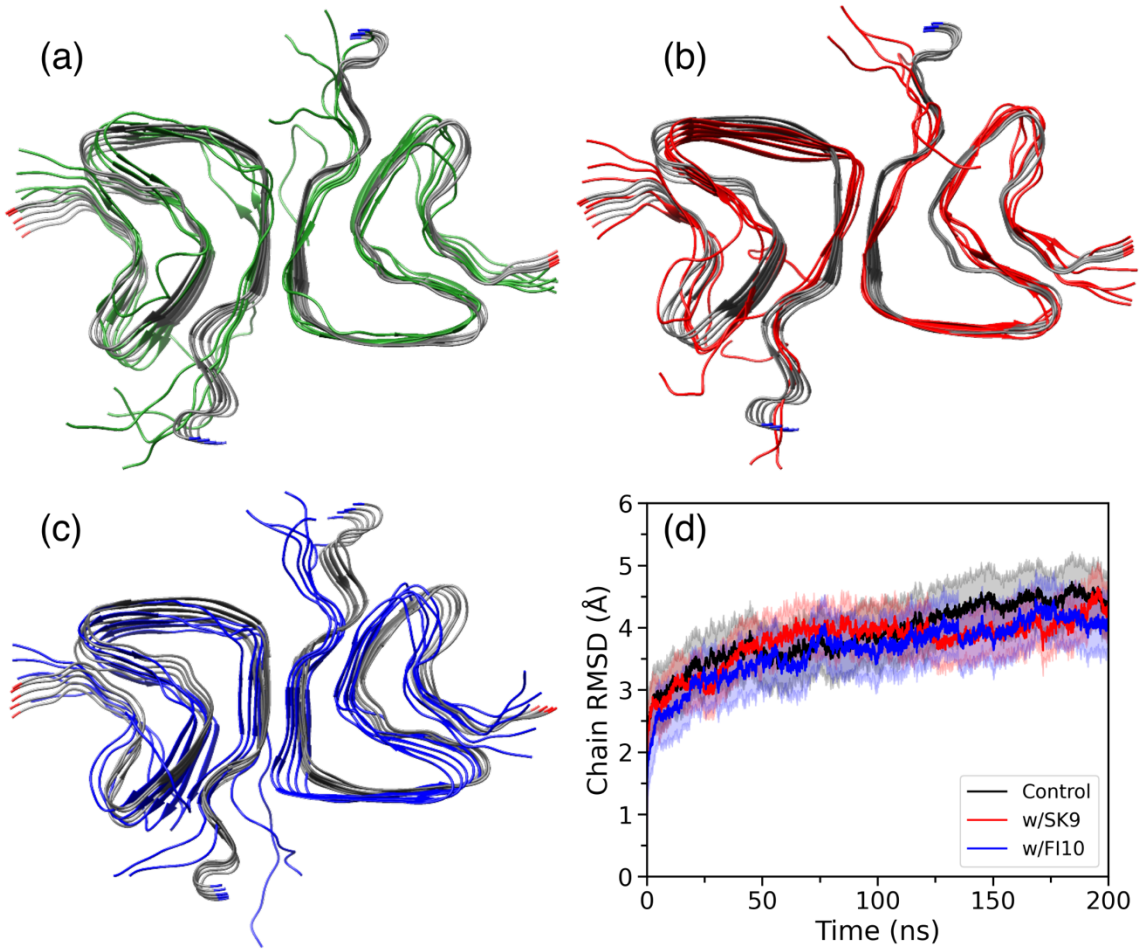

Figure 5: Representative conformations after 200 ns simulations of the rod-like αS fibril model 6CU7 in (a) absence and presence of (b) SK9 or (c) FI10. For comparison we show these conformations overlayed over the start conformation. The chain rmsd as function of time is shown for the three cases in (d), with shaded region representing the standard deviations.

Corresponding to the reduced chain flexibility are the final conformations less perturbed in presence of both viral protein fragments than for the control. Only minor changes in the stacking and packing pattern are observed, and these help to preserve the overall fibril topology, see the representative final conformations in **Figure 5a-c.** As the structural changes are mainly in the individual chains and not the overall topology of the fibril, we show in **Figure 5d** the chain root-mean-square deviation (RMSD) as function of time. Here, the RMSD calculated separately for each chain, taking only backbone atoms into account, and averaged over all ten chains in the fibril model. While the differences to the control are small, the RMSD is slightly lower when SK9 or FI10 bind to the 6CU7 rod fibril. The stabilization by SK9 and FI10 is in both cases connected with an increase in intrachain contacts (from 2410 (30) in the control to 2590 (50) for SK9 and 2533 (6) for FI10). For FI10, the increase in intrachain contacts is correlated with one in stacking contacts between layers of chains and leads to a reduced solvent accessible surface area (29400(600) $Å^2$ vs 29900(500) $Å^2$ in the control), with the difference mostly from a reduction of hydrophobic SASA (15800(300) $Å^2$ vs 16200(300) $Å^2$ in the control). However, in presence of SK9 the SASA is increased to 30500(700) $Å^2$, likely because of a lower number of packing contacts that ease separation of the two protofibrils and leads to increased exposure of hydrophilic residues, see **Table 3**.

Table 3: Mean values of hydrophobic SASA, hydrophilic SASA, total SASA, number of intrachain, stacking and packing contacts, and frequency of native interchain and intrachain contacts. All values are averages over the final 50 ns of all trajectories of the respective systems. Rod (PDB-ID 6CU7), Twister (PDB-ID 6CU8)

system	hydrophobic SASA (Å^2)	hydrophilic SASA (Å^2)	total SASA (Å^2)	intra-chain contacts	stacking contacts	packing contacts	% of native interchain contacts	% of native intrachain contacts
Rod control	16200 (300)	13700 (100)	29900 (500)	2410 (30)	1130 (20)	97 (6)	51 (4)	40 (1)
Rod w/ SK9	16300 (500)	14200 (300)	30500 (700)	2590 (50)	1130 (30)	89 (5)	54 (5)	40 (2)
Rod w/ FI10	15800 (300)	13600 (300)	29400 (600)	2533 (6)	1150 (20)	100 (20)	38 (6)	40 (1)
Twister control	10700 (400)	10700 (400)	21400 (800)	1670 (10)	700 (20)	125 (3)	43 (3)	42 (1)
Twister w/ SK9	10600 (200)	11000 (150)	21600 (400)	1642 (1)	720 (10)	112 (5)	41 (1)	40 (0)
Twister w/ FI10	10800 (100)	10900 (300)	21700 (200)	1644 (7)	719 (4)	119 (7)	49 (1)	41 (1)

On the other hand, in the 6CU8 twister fibril, per αS chain the SK9 peptides form about 31 contacts and the FI10 peptides 27 contacts. The number of contacts decreases in both cases but stays constant over the last 50 ns at 24 (1) contacts per chain for SK9, and 16 (1) contacts for FI10, i.e., the number of contacts decreased by about 20% for SK9 and 40% for FI10. As in the case of the rod-fibril simulations, neither the SK9 nor the FI10 fragment is tethered to the fibril and binding contacts may form and dissolve. Unlike for the rod-fibril, the residue-wise distribution of contacts between viral protein fragment and the αS chains in **Figure 6a** is broad for both SK9 and FI10 and covers the whole chain, with a peak for SK9 around residues H50-K58. This region of increased binding probability coincidences with the sole part of the αS chain, the segment of residues H50 to D65, where presence of SK9 leads to a pronounced decrease in flexibility that is not seen for FI10. Otherwise, few differences are seen in the residue-wise RMSD distribution when comparing

the ones for SK9 and FI10, see **Figure 6b**. Note especially that the flexibility of the region G68-A78, forming the interface between the two protofibrils in the twister polymorph, is equally reduced in presence of either of the two peptides. However, the decrease in flexibility caused by either of the two peptides appears in general to be smaller than in the case of the rod-like fibril.

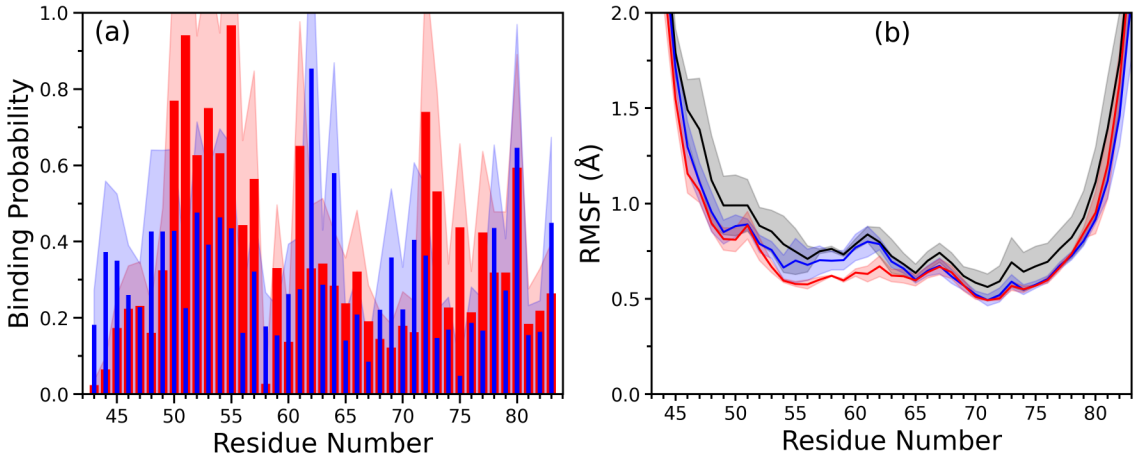

Figure 6: The residue-wise normalized binding probability of the SK9 segment (red) and the FI10 segment (blue) to αS chains in the twister-like fibril 6CU8 is shown in (a), while in (b) we show for this model the residue-wise RMSF for the αS chains in presence of SK9 (red), FI10 (blue) and in the control (black). Data are averaged over the final 50 ns of each trajectory and shaded region represents the standard deviation.

While as for the twister-like fibril the final conformations are in presence of SK9 or FI10 less perturbed than the control, see the representative final conformations in **Figure 7a-c,** we also see for the twister polymorph a clear difference in the chain RMSD curves between SK9 and FI10, see **Figure 7d**. While the values for FI10 are comparable to the control, they are for SK9 substantially lower, indicating increased stability in presence of SK9 peptides, but not in presence of FI10 fragments. This reduced RMSD likely result from the binding of SK9 to the segment H50-K58

and the induced reduction in flexibility for the segment H50-D65. However, the various quantities shown in **Table 3** do not support this picture and show only marginal differences between SK9 and FI10. While the percentage of remaining native intrachain contacts (i.e., such already present in the start conformation) changes little between rod and twister fibril, the number of interchain contacts decreases from about 50% to 40% for the SK9 complex and in the control, but it is 10% higher for FI10. This is not surprising as FI10 has the broad residue-wise binding distribution, influencing more strongly interchain binding. For the twister this leads in the case of FI10 also to a slightly increased number of stacking contacts and similar decreased number of packing contacts. However, consistent with the visual inspection of the final conformations in **Figures 7a-c** do the various quantities in **Table 3** indicate that presence of SK9 or FI10 stabilizes the twister fibril only marginally, with little differences between the two viral protein fragments. Hence, presence of the viral protein fragments affects the twister-like fibril very different from the rod-like fibril where we saw a clearer signal indicating stabilization by FI10, and to a lesser degree also by SK9.

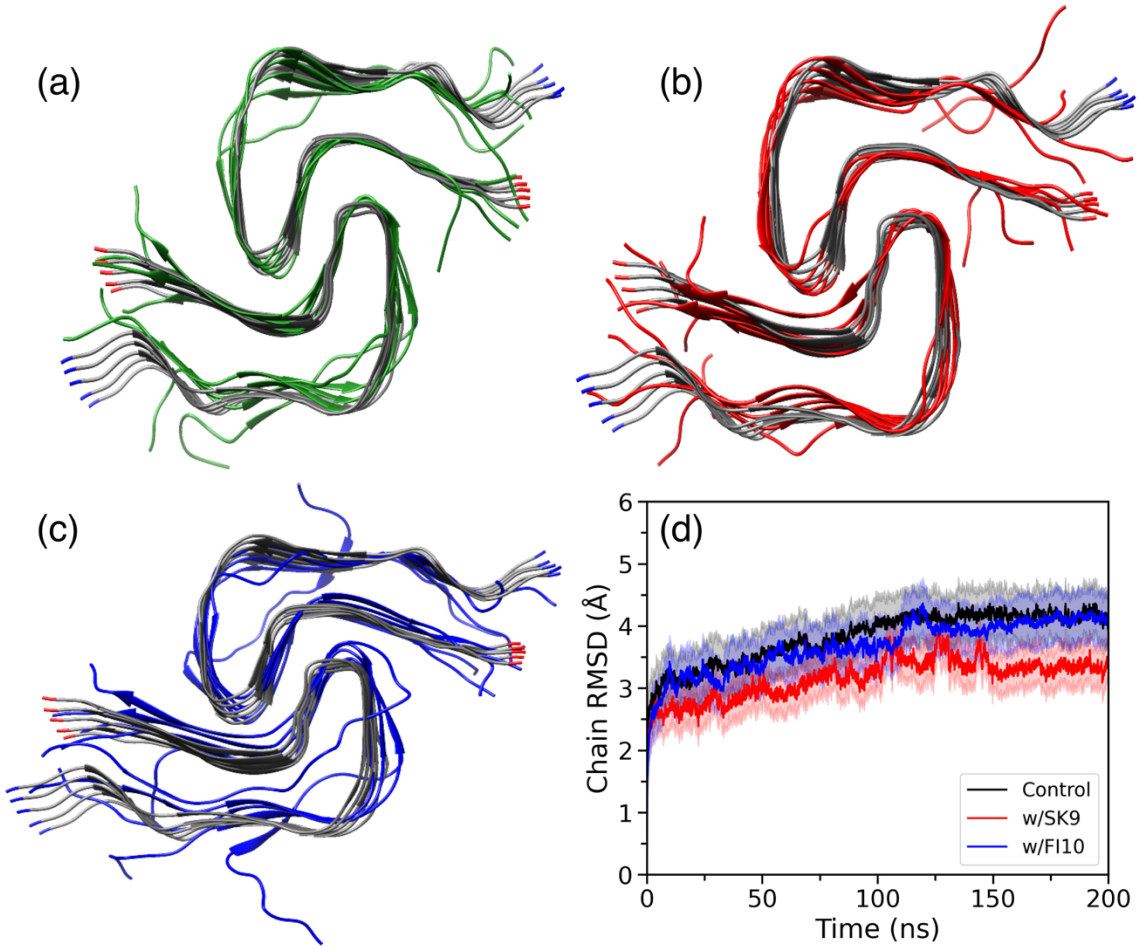

Figure 7: Representative conformations after 200 ns simulations of the twister-like αS fibril model 6CU8 in (a) absence and presence of (b) SK9 or (c) FI10. For comparison we show these conformations overlayed over the start conformation. The chain rmsd as function of time is shown for the three cases in (d), with shaded region representing the standard deviation.

CONCLUSIONS

Using molecular dynamics simulations, we have studied the effect of two protein fragments of the SARS-COV-2 virus on the structural ensemble of αS monomer, and on the stability of αS fibrils. One virus protein fragment is from the Envelope protein (SK9) and one from the Spike protein (FI10). Both bind to the αS monomer, and induce the shift toward more aggregation-prone

conformations that we also saw in our previous studies, not only of αS but also with Serum Amyloid A and amylin.[28,37] This effect is stronger for FI10, a fragment that is unique for SARS-COV-2 and cleaved from the Spike protein by enzymes released during pronounced inflammation.[19] Especially in the case of FI10 leads the shift in the ensemble of αS chains to conformations with preference for assembly into rod-like fibrils. We also find again the earlier observed stabilization of fibrils. This effect is differential. While both SK9 and FI10 alter only marginally the stability of the twister polymorph, the stability of rod-like fibrils is clearly enhanced, with the effect more pronounced for FI10 than for SK9.

Hence, while the time scales of our simulations are small compared to that of amyloid formations, our data indicate already that SARS-COV-2 protein fragments can induce amyloid formation of αS (implicated in Parkinson Disease), and that this effect is differentially, i.e., favoring certain polymorphs, in our case rod-like αS fibrils over fibrils with a twister-like chain structure. However, the relation between αS polymorphs and disease phenotype has not been established. While fibrils seeded with lysates from brain tissue of Parkinson Disease patients have rod-like structures,[93] this may be an artefact of the growth conditions. On the other hand, the clustering of familial mutations associated with Parkinson disease in the preNAC region, de-stabilizing the rod-architecture but not twister-like conformations, rather points to twister polymorphs as disease-causing agent.[84] Hence, it is not clear whether our observation points to a mechanism that may explain the correlation between SARS-COV-2 infections and early onset of Parkinson Disease. Nevertheless, our results add to an emerging picture of SARS-COV-2 protein fragments (cleaved during infection-cause inflammation) cross-seeding amyloidogenic human proteins, potentially triggering the onset of the associate amyloid diseases.

ACKNOWLEDGMENT

The simulations in this work were done using the SCHOONER cluster of the University of Oklahoma, XSEDE resources allocated under grant MCB160005 (National Science Foundation), and TACC resources allocated under grant under grant MCB20016 (National Science Foundation). We acknowledge financial support from the National Institutes of Health under grant GM120634. We thank Shailesh K. Panday for help at an early stage of this study with setting up and running simulations.

Chapter 6 - Podoplanin Positive Cell-derived Small Extracellular Vesicles Contribute to Cardiac Amyloidosis After Myocardial Infarction

The following chapter will provide a brief overview of the experimental work performed by Cimini et al, as well as the computational work performed by the author of this dissertation to support their experimental findings. The resulting work was published as "Podoplanin Positive Cell-derived Small Extracellular Vesicles Contribute to Cardiac Amyloidosis After Myocardial Infarction" in Cell Reports, 44 (2025), 105408, by Maria Cimini, Ulrich H.E. Hansmann, Carolina Gonzalez, Andrew D. Chesney, May M. Truongcao, Erhe Gao, Tao Wang, Rajika Roy, Elvira Forte, Vandana Mallaredy, Charan Thej, Ajit Magadum, Darukeshwara Joladarashi, Cindy Benedict, Water J. Koch, Çağla Tükel, and Raj Kishore.[20]

This study focused on the contributions to cardiac amyloidosis following myocardial infarction in mice. Our experimental collaborators identified a subset of activated cardiac stromal cells (CSC) that acquire the expression of a platelet aggregation-inducing type 1 transmembrane glycoprotein named Podoplanin (PDPN) as a key factor in the amyloidosis process. They went on to show that CSC^{PDPN+} release small extracellular vesicles (sEVs) to communicate with macrophages following myocardial infarction. The components within the CSC^{PDPN+} sEVs were then evaluated via proteomic analysis using mass spectrometry. It was found that serum amyloid A3, was quantitatively and statistically upregulated in CSC^{PDPN+} sEVs. They then showed that CSC^{PDPN+} sEVs are required to activate and induce SAA3 over expression in bone marrow derived macrophages (BMDMs) via toll-like receptor 2 (TLR2) activation and p38-MAPK

phosphorylation. This over expression of SAA3 was shown to contribute to the presence of amyloid fibrils in heart scar tissue following myocardial infarction.

Previously, in the Hansmann group the effects of small peptides on human SAA1 fibril stability were investigated.[21] From these computational investigations the peptide RSFFS, or R5S, was identified to destabilized the fully formed SAA1 fibril structures. However, due to the inherent difficulties this peptide would exhibit when utilized as a treatment *in vivo*, namely proteolytic cleavage, a D-retro-inverso version was purposed. A D-retro-inverso (DRI) peptide is a peptide in which the sequence of the amino acids is reversed, while also inverting the chirality of the amino acids from the native L-enantiomer to the D-enantiomer. Simulations with this peptide were also shown to destabilize the fibril structure of SAA1. From these results, our experimental collaborators utilized this DRI-R5S peptide in their mice system following myocardial infarction as a potential treatment. Treating the mice with DRI-R5S every other day for 30 days after myocardial infarction resulted in decreased scar formation as well as increased cardiac function compared to those treated with saline. These results are extremely promising as there are currently no specific treatments for cardiac amyloidosis.

To provide a possible explanation for the results observed, molecular docking and free energy calculation were performed. Of interest were the interactions between DRI-R5S and human sAA1 cross-β fibril structures, mouse SAA3 monomers, fibronectin, and collagen 1α. As well as the effect these interactions had on the interactions between the proteins investigated. Molecular docking was performed using HADDOCK[94] to model the interactions, and binding free energy was approximated with PRODIGY[67]. From our calculations, it was found that DRI-R5S binds

most strongly to SAA3 monomer (-36 kJ/mol) and fibronectin (-43 kJ/mol), as compared to its interactions with the SAA1 fibril (-22 kJ/mol) and collagen 1α (-16 kJ/mol). The results indicate that all SAA3 monomers will be bound with DRI-R5S as well as the fibronectin fibrils. From our calculations, we found that the DRI-RSFFS segment interacts with the following mouse SAA3 monomer residues: E27, A28, G31, S32, M35, W36, Y39, M42, K43, D51, H55, A62, G68, G69, A72, A73, I76, R80, V83, Q84, T87, H89. The guanidinium group of the arginine (R) residue of the DRI peptide was found to nestle into a pocket in the surface of the monomer and contributed most to the interactions between the peptide and monomer, interacting with E27, A28, G31, S32, G68, G69, A72, A73. It was also noted that the DRI peptide interacts with residue E27 through its backbone atoms rather than its sidechain carboxylate group. The DRI-RSFFS segment was found to interact with the following fibronectin residues (PDB-ID: 1FBR): F5, D6, H7, L21, P22, Y23, M27, V29, G39, I41, T42, C43, T44, S45, R48, C49, N50, R83, G84, E85, W86. These interactions can be organized into 3 main clusters depending on the DRI residue: Cluster 1 (DRI-residue 1), Cluster 2 (DRI-residues 2-4), and Cluster 3 (DRI-residue 5). Interactions involved in Cluster 1 include the following residues: F5, D6, H7, G39, I41. Cluster 2: L21, P22, Y23, M27, V29, I41, T42, C43, T44, S45. Cluster 3: T44, S45, R48, C49, N50, R83, G84, E85, W86. The fibronectin residues of the Cluster 3 formed a pocket with which the C-terminal arginine residue of the DRI segment interacted. These interactions contribute to most of the contacts observed. Similarly, cluster 1 also formed a pocket on the surface of the protein, which interacted with the N-terminus of the DRI-peptide. Cluster 2 contributed to a grove that connected Cluster 1 and Cluster 3.

Additionally, free energy calculations were performed to examine the effects DRI-R5S has on the ability of SAA3 monomers to interact with collagen 1α and fibronectin. It was shown that the

presence of DRI-R5S had little impact on the binding of SAA3 monomers with collagen 1α, while there was a slight increase in binding free energy between SAA3 monomers bound with DRI-R5S and fibronectin. This slight increase may indicate that SAA3 monomers will bind with fibronectin and be less likely to form fibril structures. We also noted a strong reduction in the stability of growing SAA1 fibrils when in the presence of DRI-R5S. This was evaluated by docking two fibril structures together, in the presence of absence of the DRI-R5S segment. This indicated a destabilization effect, which may make the formation of elongated fibrils difficult.

Overall, in this project I was able to help provide insights into the interactions observed in our collaborator's experiments. However, this relatively simple analysis can be further evaluated utilizing molecular dynamics simulations. In the following chapter, **Chapter 7**, I introduce and discuss a project that stemmed from this collaboration, in which I seek to identify new DRI-peptides that may be able to disrupt the stability of mouse SAA3 utilizing molecular dynamics.

Chapter 7 – D-Retro-Inverso Peptides for Inhibition of Serum Amyloid A3 Aggregation

The following chapter is taken from a draft of a forthcoming article soon to be submitted.

Introduction

Serum amyloid A (SAA) is an acute phase protein that is associated with the inflammation response. Following inflammation, SAA levels increase to upwards of 1000 times normal levels. This spike in concentration is normally short lived, however chronic inflammation can lead to high concentrations of SAA in the body. These high concentrations can lead to the potential misfolding and aggregation of SAA into fibril structures. These fibrils can then deposit into organs such as the liver, kidneys, and the heart, resulting in secondary amyloidosis. SAAs are evolutionary conserved throughout vertebrate species. With there being high sequence similarities between human and mice SAA1/2 and SAA4. However, in mice there is the presence of SAA3, which is considered to be a pseudogene in humans due to an early stop codon but has been shown to exist as fusion protein with SAA2[95]. SAA proteins in mice are known to be synthesized hepatically (SAA1/2/4)[96–98] and extra-hepatically (SAA3)[98]. Those synthesized hepatically largely contribute to the circulating SAAs, while SAA3 is secreted more locally at the site of injury[99]. As SAA3 can bind to toll-like receptor 2 (TLR2) on macrophages, it leads to signaling that initiates the enhanced self-production of SAA3 and other cytokines and chemokines.[100,101] During chronic inflammation, the enhanced levels of SAA3 derived from activated macrophages leads to decreased cleavage of SAA3. As a result, saturated lysosomes release SAA3 monomers that are enriched with β-sheet motifs that are prone to aggregation, which accumulate into insoluble amyloid protofilaments in the extra cellular matrix[102].

It has been recently shown experimentally that following myocardial infarctions in mice, amyloidosis occurs in the heart, and the amyloid fibrils produced are comprised of macrophage-derived SAA3 monomers[20]. Previously, the Hansmann group investigated potential small peptide inhibitors for human SAA aggregation[21]. Of the small peptides investigated, the first five residues of human SAA1, RSFFS, or R5S, was shown to destabilize the full-length fibril model of SAA the most. Which built upon previous experimental results that highlighted the ability of the peptide to inhibit the formation of amyloid fibrils made of short SAA_{1-12} fragments[103]. However, due to the likely short half-life when implemented because of proteolytic cleavage another form of the peptide was tested. A peptide in which the sequence was reversed, and the chirality of each residue was inversed was utilized. The resulting peptide is referred to as a D-retro-inverso (DRI) peptide. By reversing the target sequence and inverting the chirality, the resulting peptide is more resistant to proteolytic cleavage while maintaining similar sidechain orientations of the native L-enantiomer. An example illustrating the D-retro-inverso transformation is shown in **Figure 1.**

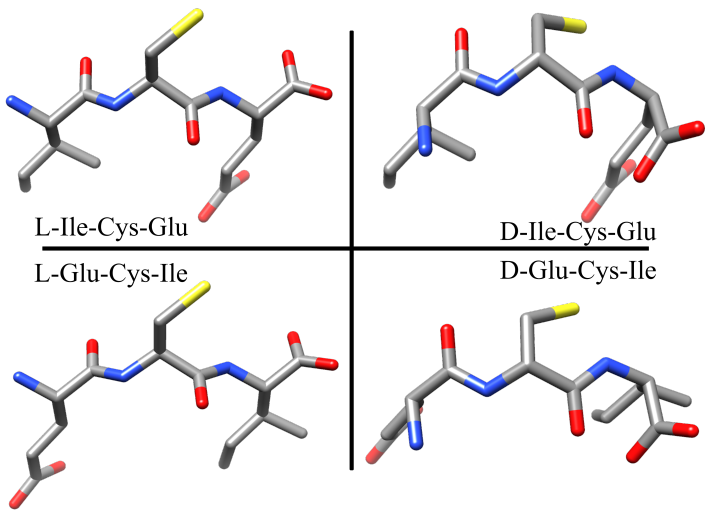

Figure 1: Diagram illustrating the differences and similarities of between a L-enantiomer, top left quadrant, and a DRI-peptide, bottom right quadrant.

The DRI-R5S peptide also showed fibril disruption capabilities like the L-enantiomer. As a result of this study, experimental investigators, Cimini et al., utilized this proposed peptide in their investigations of mouse SAA3 amyloidosis following myocardial infarction. The proposed peptide was able to decrease the formation of SAA3 amyloid fibrils as well as improve the cardiac function of the treated mice compared to the control group[20]. Motivated by this successful implementation of DRI-R5S as a treatment for mice following myocardial infarction, we have performed all-atomistic molecular dynamic simulations to investigate the effects DRI-R5S has on mouse SAA3 fibril stability. Additionally, we have performed virtual screening utilizing hexamer DRI-peptides and have identified three novel potential inhibitor candidates. For further evaluation of the inhibitor candidates, molecular dynamics simulations were also performed.

Methods

Generation of SAA3 Fibril Model

At this point in time there is no fibril structure of mouse SAA3 available from the Protein Data Bank. To generate a structure to use in our simulations, a vascular variant of human SAA1 was utilized, PDB ID: 7zky. Due to the high sequence similarity between human SAA1 and mouse SAA3, this structure served as a backbone to build our model. The structure was then mutated to match the mouse SAA3 sequence using UCSF Chimera[62]. The resulting model generated is shown in **Figure 2** and consists of three layers with two protein chains per layer for a total of six chains. A system of consisting of two folds and three layers was selected as previous studies within the Hansmann group had shown that such a structure was above the critical threshold required for fibril stability[21].

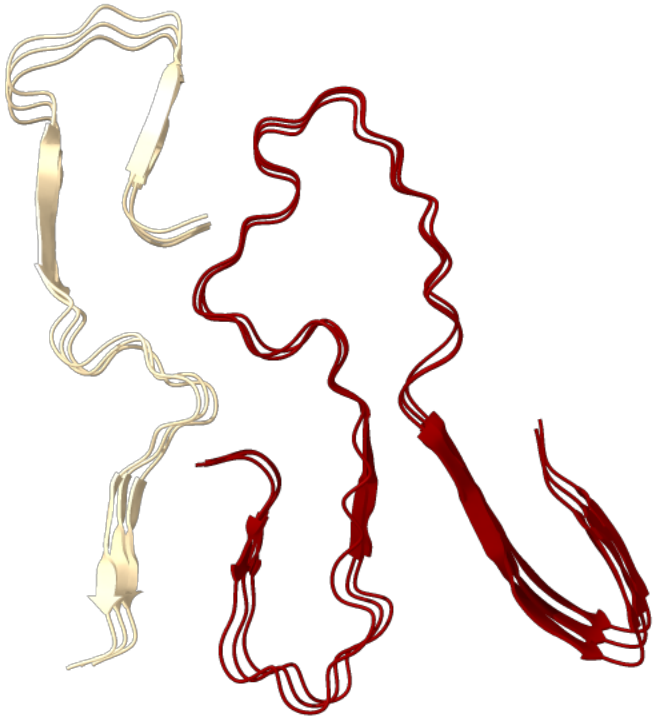

Figure 2: Fibril model of SAA3 utilized in simulations. Protofibril 1 is shown in red and Protofibril 2 is shown in cream.

Generation of DRI-Peptides

To begin our investigations, we decided to look at identifying potential hexapeptide inhibitor candidates. Due to the possible ~ 20^6 combinations of hexapeptides, a smaller data set was used. Stemming from the origins of the RSFFS segment, which comes from the first five residues of human SAA1, the WALTZ-DB 2.0 database[104] of potential amyloid forming hexapeptides was utilized resulting in 1,402 peptides. To generate the reversed peptides, the sequences of the hexapeptides were reversed. Then were generated using PeptideBuilder[105]. Following the creation of the reversed peptide structure files, the peptides were then converted to their D-enantiomer confirmation by swapping the positions of the β-carbon and α-hydrogen for each residue. The resulting structures were then energy minimized in gas phase using SANDER from AmberTools[106]. The DRI-RSFFS segment was generated in a similar manner. The 1,402 peptides generated were

then screened against the SAA3 fibril model. Autodock Vina[86] version 1.1.2 was utilized in a global search as no binding sites of SAA3 are known. A grid search area of 107.309Å x 80.0083Å x 47.3189Å was used to allow ample room for the peptides to move around the SAA3 fibril. To account for potential off-target molecule interactions, the peptides were also screened against collagen 1α (PDB:2LLP) and fibronectin (PDB:1FBR), with search areas of 53.5701Å x 24.4785Å x 26.1194Å and 61.8103Å x 28.7406Å x 37.8707Å, respectively. Following the screening process, the top three inhibitor candidates based off Autodock Vina affinity scores were selected for further study. The three peptides selected were DRI-GVWWFF (DRI-G6F), DRI-ERGFFY (DRI-E6Y), and DRI-HFVWIA (DRI-H6A). The Autodock Vina affinity scores of the peptides with respect to SAA3, collagen 1α, and fibronectin are shown in **Table** 1.

Table 1: Autodock Vina affinity scores of the top inhibitor candidates and DRI-R5S with respect to SAA3, collagen 1a, and fibronectin.

Peptides	Autodock Vina Affinity Scores (kcal/mol)		
	SAA3	Collagen 1a	Fibronectin
DRI-GVWWFF	-9.2	-4.5	-6.0
DRI-ERGFFY	-8.7	-4.3	-5.6
DRI-HFVWIA	-8.4	-5.3	-6.5
DRI-RSFFS	-7.6	-4.7	-7.3

The selected inhibitor candidates and DRI-RSFFS were then docked with the SAA3 fibril model in a 1:1 ratio of peptide to monomer chains found in the fibril model using HADDOCK 2.4[47,94], resulting in four structures. Similarly, the peptides were docked with collagen 1a and fibronectin to explore possible off-target effects.

General System Preparation and Simulation Protocol

To generate the initial structures for the molecular dynamic simulations performed, the SAA3 model, collagen 1a (PDB:2LLP), fibronectin (PDB:1FBR), and all the docked structures were converted to GROMACS format using the pdb2gmx module. During this step hydrogen atoms were added to the structures. All chains and peptides were also capped with $-NH_3^+$ and $-COO^-$ groups. For the simulations performed the CHARMM 36m-July 2017[50] all-atom force field was utilized with TIP3P[107] explicit water molecules. All simulations were performed with GROMACS 2020.4 software package[49]. The structures were then placed in the center of cubic simulation boxes with a minimum distance of 15Å between the solute and the edge of the box. The boxes were then filled with water molecules, and counter ions were added to neutralize the system in accordance with the particle-mesh Ewald method. Na^+ and Cl^- ions were used as the counterions and were set to a physiological concentration of 150 mM NaCl. The total number of atoms and water molecules from each system is listed in **Table 1**. Following the addition of water and counterions, the systems were then energy minimized. The steepest decent method was used, and the systems were minimized for up to 50,000 steps. The systems were then subjected to equilibration at constant volume to set the temperature of the system to 310K for 200ps. Then, at a constant pressure of 1 bar for an additional 200ps. During these equilibration steps the heavy atoms were constrained with a force constant of 1000 kJ/mol•nm^2.

To main a constant temperature during the simulation a velocity-rescale thermostat[56] was used with a coupling constant of 0.1 ps. Pressure was maintained by using the Parrinello-Rahman barostat[57] with a pressure relaxation time of 2 ps. A time step of 2 fs was used for integrating the equations of motion. This was made possible by using the SETTLE[58] algorithm to insure the water

molecules were rigid, as well as restraining protein bonds involving hydrogen atoms to their equilibrium length with the LINCS[59] algorithm. Periodic boundary conditions were utilized for all systems, as a result the long-range electrostatic interactions were computed with the particle-mesh Ewald method, using a real-space cutoff of 12Å and a 1.6Å Fourier grid spacing. Short-range van der Waals interactions were truncated at 12Å with smoothing beginning at 10 Å. Each system was simulated in triplicate differing by their initial velocity distribution. The length of the trajectories studied for each system is listed in **Table 2**.

Table 2: Simulated Systems

	System	Total Atoms	Water Molecules	Individual Simulation Time (ns)	Total Simulation Time (ns)
SAA3	Control	217,853	70,729	500	1500
	DRI-R5S	210,506	68,106		1500
	DRI-G6F	209,565	67,745		1500
	DRI-E6Y	210,665	68,119		1500
	DRI-H6A	211,966	68,554		1500
Collagen 1α	Control	51,635	16,463	400	1200
	DRI-R5S	49,508	16,166		1200
	DRI-G6F	49,526	16,148		1200
	DRI-E6Y	47,253	15,395		1200
	DRI-H6A	50,913	16,614		1200
Fibronectin	Control	72,606	23,689	400	1200
	DRI-R5S	72,195	23,522		1200
	DRI-G6F	73,493	23,946		1200
	DRI-E6Y	74,025	24,124		1200
	DRI-H6A	73,140	23,830		1200

Trajectory Analysis

The molecular dynamics trajectories are analyzed with the GROMACS tools[49] and MDTraj software[61]. For visualization of trajectory conformations we use VMD[60] version 1.9.4a57, and UCSF ChimeraX-1.9[108]. The root-mean-square deviation (RMSD), root-mean-square-fluctuation (RMSF), and solvent accessible surface area (SASA) are calculated using GROMACS tools, for the latter quantity using a spherical probe of 1.4 Å radius. The residue-wise contact frequencies are calculated using GROMACS and MDTraj software, defining contacts by a cutoff 4.5 Å in the closest distance between heavy atoms in a residue pair. The binding free energy between the inhibitor candidates and the SAA3 fibril and off-target proteins was calculated using the approach described in Bellaiche et. al[65]. This approach was used earlier to study inhibition of Aβ amyloid formation by small peptides[66] and relies on calculating a dimensionless association constant from the distribution of bound and unbound conformations.

Results and Discussion

Mouse SAA3 Fibril Simulations

We begin our discussion on the effects of DRI-peptide inhibitor candidates on mouse SAA3 by exploring the effects the peptides have on the overall structure of the fibril model. To gleam an overall picture of the fibril assembly over the course of a trajectory the global backbone RMSD of the SAA3 fibril was calculated. As shown in **Figure 3**, we note that both the control simulations, the simulations in the absence of any peptide, and the simulations in the presence of DRI-R5S have an increased average global RMSD compared to the other simulated systems. While the overall system in the presence of DRI-G6F shows less deviation compared to initial structure.

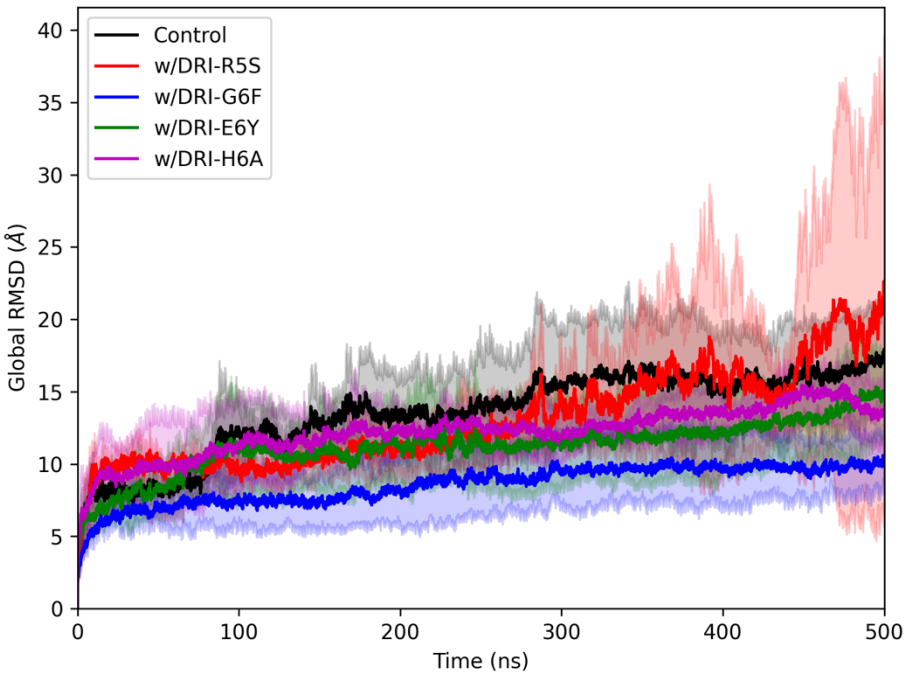

Figure 3: Average Global Root Mean Square Deviation (RMSD) of SAA3 backbone atoms in reference to the initial frame of the simulation in the absence and presence of DRI peptide inhibitor candidates, with shaded regions indicating standard deviation. Control simulations are shown in black. Simulations in the presence of DRI-R5S are shown in red, DRI-G6F in blue, DRI-E6Y in green, and DRI-H6A in magenta.

However, to further quantify the effect the peptide inhibitors have on the system other quantities must be examined. When we shift to examine the average chain-wise backbone RMSD, **Figure 4**, we note a similar trend, in which the control simulations have a higher deviation than the inhibitor candidates. From the chain-wise RMSD we note that the control simulations fibril chains are moving on average 10Å from the initial positions. Interestingly, the simulations in the presence of DRI-H6A, show a higher chain-wise RMSD than the other inhibitor candidates.

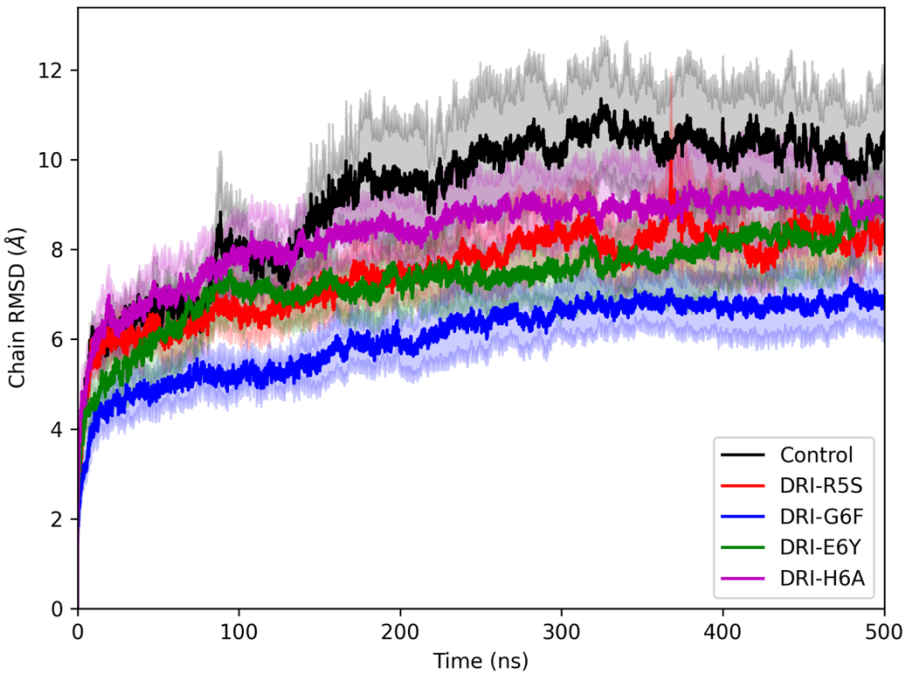

Figure 4: Average chain-wise RMSD of SAA3 backbone atoms in reference to the initial frame of the simulation in the absence and presence of DRI peptide inhibitor candidates, with shaded regions indicating standard deviation. Control simulations are shown in black. Simulations in the presence of DRI-R5S are shown in red, DRI-G6F in blue, DRI-E6Y in green, and DRI-H6A in magenta.

To evaluate the effect of the presence of the DRI peptides on residue-wise backbone fluctuations RMSF was calculated, and averaged over the last 100ns of the simulations, **Figure 5**. Due to the asymmetric nature of the fibril model utilized, RMSF is shown averaged over each respective protofibril. In the presence of DRI-H6A we note an increased flexibility in protofibril 1 ranging from residue 15 to 46 and residue 53-69 compared to the control simulations. While in the presence of the other peptides, a decreased flexibility of protofibril one is observed. In the presence of DRI-R5S and DRI-E6Y, protofibril 2 shows an increased flexibility in the N-terminal residues, 2-12, compared with the control. In the presence of all peptides, residues 21-40 in protofibril 2 show decreased flexibility.

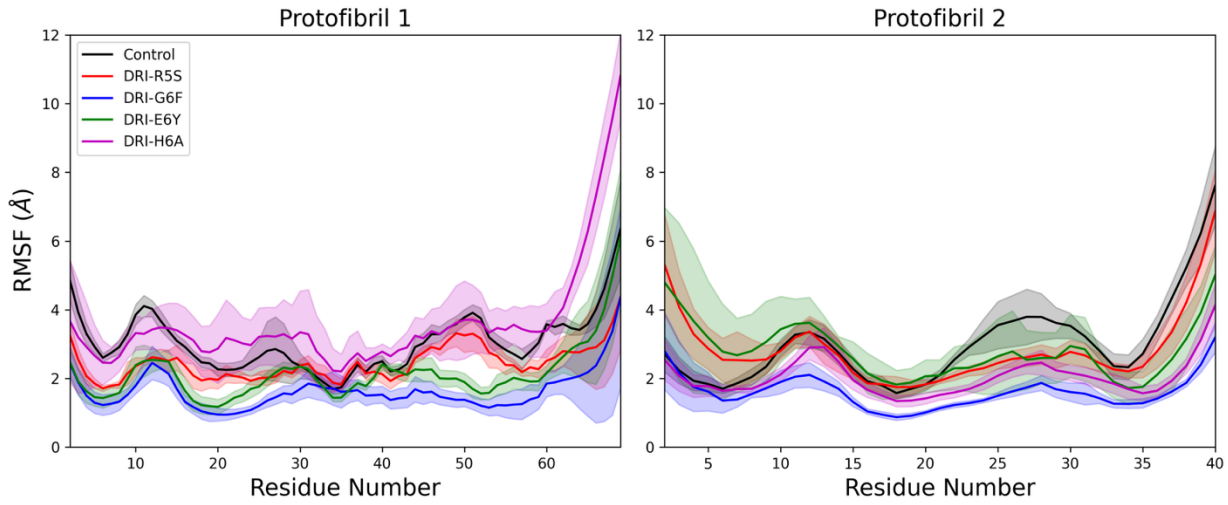

Figure 5: Average residue-wise Root-Mean-Square-Fluctuation (RMSF) of SAA3 fibril backbone in the presence and absence of DRI peptide inhibitors candidates. Standard deviation indicated by the shaded regions.

To get an understanding of how the DRI-peptides are interacting with the SAA3 fibril model, contacts between the peptide segments and fibril were calculated. To allow for easier comparison between the peptide sequences, the number of contacts were averaged and normalized, such that the number of contacts in the initial frame were equal to 1. As failing to do so artificially indicates less interactions between the DRI-R5S segments and the fibril, due to the peptide consisting of 5 amino acids compared to the other hexapeptides used. As shown in **Figure 6a**, we note that DRI-G6F has approximately over 80% of its total contacts remaining compared to the initial frame over the last 100ns. While DRI-R5S and DRI-E6Y both have approximately 60% of their total contacts. DRI-H6A however shows decreased contacts over the last 200ns, with approximately 50% of its total contacts remaining compared with the initial frame. To further evaluate the interactions between the DRI-peptides, we look at the evolution of the native, or initial, contacts between the fibril and segments. This is shown in **Figure 6b**. We note in all simulations a decrease in the contacts that were present initially. This indicates that the segments are moving from their initial

binding sites, as there are no restraints applied to the peptides some drift is to be expected. We do see that approximately 12% of the initial contacts between DRI-G6F are preserved over the simulation. When compared to the other peptides whose normalized native contacts range from 5-7%, DRI-G6F is clearly interacting stronger with the SAA3 fibril.

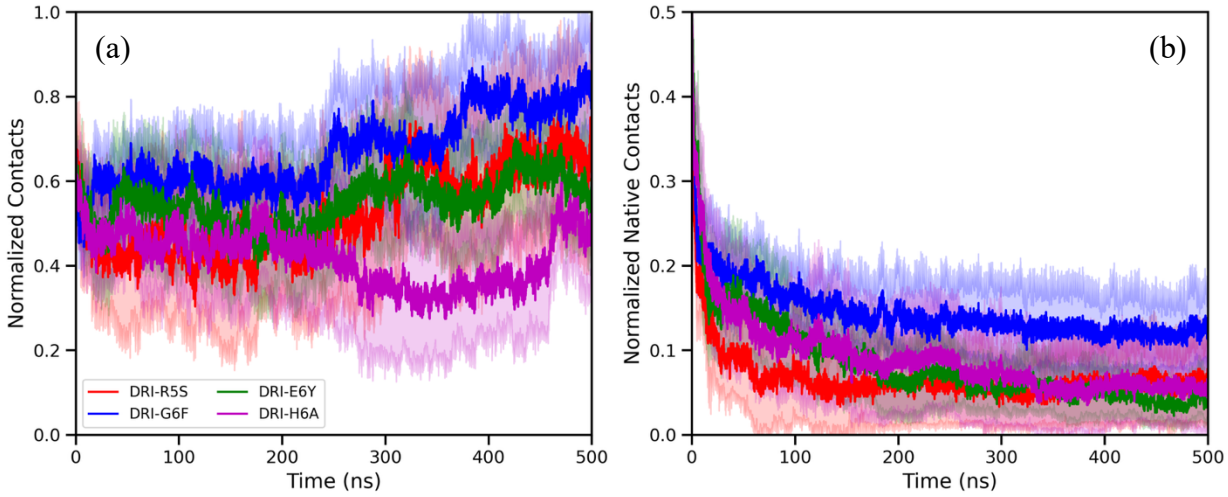

Figure 6: (a) Normalized average contacts between the DRI peptides and SAA3 fibril over the length of the simulations. Contacts are normalized to the number of contacts in the initial frame of the trajectory. **(b)** Normalized average native contacts between the DRI peptides and SAA3 fibril over time. Native contacts are taken to be contacts found in the initial frame of the trajectory. Shaded regions indicate standard deviations.

To explore the location of the binding interactions on the fibril model, the average contact frequency per DRI-peptide segment was calculated over the last 100ns of the simulations and plotted against the fibril residue index, **Figure 7**. From this figure we see clear differences in contact distribution between the various peptides.

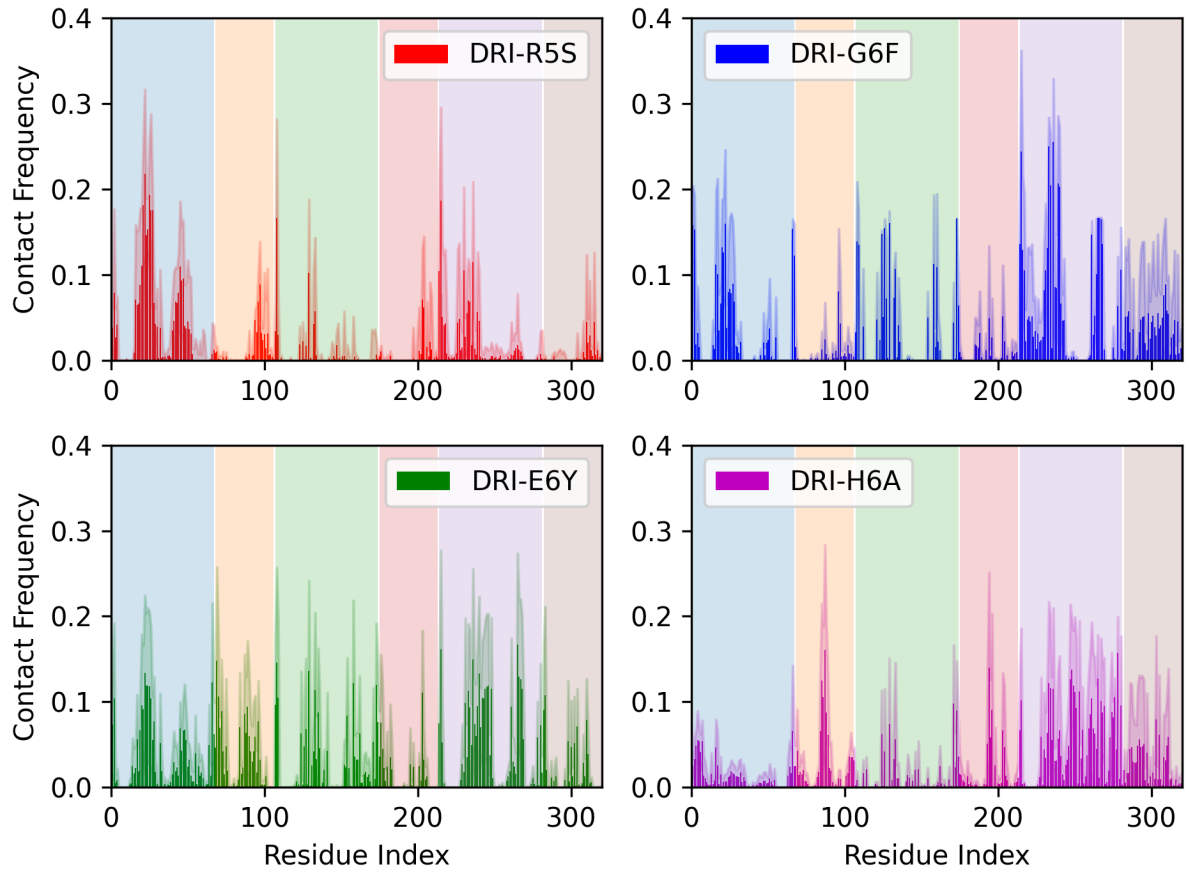

Figure 7: Average contact frequency per DRI-peptide segment with respect to SAA3 fibril residue index with shaded regions indicating the standard deviation. The contact frequency was calculated over the last 100ns of the simulations. To indicate the regions associated with the six chains found in the fibril model, Chain A is highlighted in blue, Chain B in orange, Chain C in green, Chain D in red, Chain E in purple, and Chain F in brown.

DRI-R5S interacts mainly with residues found in chain A of the fibril model, while mainly DRI-G6F interacts with the N-terminal region of chain E as well as chains A and F. In comparison, the distribution of DRI-E6Y is broad and spread over all chains in the fibril. Like DRI-G6F, the DRI-H6A segments interacting mainly with chain E and F, as well as chains B and D. Additionally from this figure, we note that the contact frequency for DRI-G6F is increased compared with the other peptides, further indicating the increased interactions observed with the SAA3 fibril.

Table 3: Average normalized final values of total SASA, hydrophobic SASA, hydrophilic SASA, stacking and packing contacts for the SAA3 fibril systems.

System	Total SASA	Hydrophobic SASA	Hydrophilic SASA	Stacking Contacts	Packing Contacts
Control	1.30 ± 0.03	1.37 ± 0.05	1.24 ± 0.01	0.73 ± 0.03	0.80 ± 0.01
DRI-R5S	1.27 ± 0.09	1.3 ± 0.1	1.23 ± 0.09	0.81 ± 0.05	0.53 ± 0.06
DRI-G6F	1.26 ± 0.05	1.19 ± 0.07	1.33 ± 0.03	0.80 ± 0.05	0.42 ± 0.08
DRI-E6Y	1.23 ± 0.04	1.21 ± 0.04	1.25 ± 0.06	0.76 ± 0.04	0.6 ± 0.1
DRI-H6A	1.27 ± 0.05	1.25 ± 0.08	1.29 ± 0.03	0.76 ± 0.03	0.5 ± 0.3

To evaluate the effect of the various peptides on the fibril stability solvent accessible surface area (SASA) was calculated. SASA is a measurement of how much surface is exposed to the solvent. Folded proteins prioritize burying their hydrophobic residues; therefore, structures that have lower exposed hydrophobic residues are more compact. The total SASA, hydrophobic SASA, and hydrophilic SASA were calculated over the course of the simulations. Shown in **Table 3** are the average normalized final SASAs for each system. All systems indicate an increase in total SASA compared to the initial structure. This increase indicates a structure that is less compact than the initial structure. When comparing the final normalized hydrophobic SASA between the systems a larger difference is observed. For the control and the DRI-R5S simulations we observe an average final normalized value of 1.37 ± 0.05 and 1.3 ± 0.1 respectively. Comparing with the other peptide simulations we note that this increase in hydrophobic SASA is more pronounced, especially compared to the DRI-G6F simulations which have an average final value of 1.19 ± 0.07. This difference in hydrophobic surface area shows that the hydrophobic core of the fibril structure in

the absence and presence of DRI-R5S is more exposed resulting in a less compact structure. In the presence of DRI-G6F the hydrophilic SASA of the SAA3 fibril has increased more than the other systems. This along with the relatively decreased exposed hydrophobic SASA indicates that the SAA3 in the presence of DRI-G6F is more compact.

Other quantities calculated to evaluate the effect of DRI-peptides on fibril stability were stacking and packing contacts of the fibril. Stacking contacts here refer to the number of contacts between the layers of the fibril. In the simulations stacking contacts were calculated by determining the number of contacts between layer 1 and 2, and layer 2 and 3. These values were then added to achieve the total number of stacking contacts. Packing contacts refer to the contacts between the two protofibrils found in the fibril. Also shown in **Table 3** are the final average normalized stacking and packing contacts. Overall, the normalized stacking contacts for all peptide systems range from approximately 76-81% of the number of contacts present in the initial frame. This indicates that the stacking contacts in the presence of the DRI-peptides are relatively unaffected compared to the control simulations with approximately 73% of the initial number of contacts remaining. However, when packing contacts are considered, there is quite a difference between the control and peptide simulations. The control system has 0.80 ± 0.1 of the initial number of contacts at the end of the simulation while the peptide simulations have normalized packing contacts ranging from 0.42 to 0.6. The lowest being associated with DRI-G6F. This may, however, be misleading. After visual inspection of the trajectories, the fragments of DRI-G6F are interacting at the protofibril interface. As a result, there is a decrease in contacts forming between the two protofibrils. As both protofibrils are interacting with the fragments in this interface, the overall stability is preserved and explains the trends observed in SASA and RMSD.

Simulations of Off Target molecules, Collagen 1α and Fibronectin

To evaluate the potential effects on off-target molecules that were identified by Cimini et. al, we performed molecular dynamic simulations of collagen 1α and fibronectin in the presence and absence of the DRI-peptides identified. We begin our discussion by focusing on the simulations performed with collagen 1α. To examine the effect on the overall structure of the protein over the trajectory, global backbone RMSD was calculated. **Figure 8a** shows the average RMSD of the collagen 1a backbone in the presence and absence of the DRI-peptides. We note that on average in the presence of DRI-E6Y, DRI-R5S, and DRI-G6F the RMSD of collagen 1a is increased compared to the control simulations. While the simulations in the presence of DRI-H6A behaved similarly as the control simulations. The average normalized contacts between the peptides and collagen 1α were also calculated and are shown in **Figure 8b**. In all simulations we note fewer contacts over the course of the trajectories. Especially for DRI-R5S and DRI-H6A. This decrease in contacts indicates little binding specificity to the collagen 1a protein. As collagen 1α is an off target, this decreased affinity is promising.

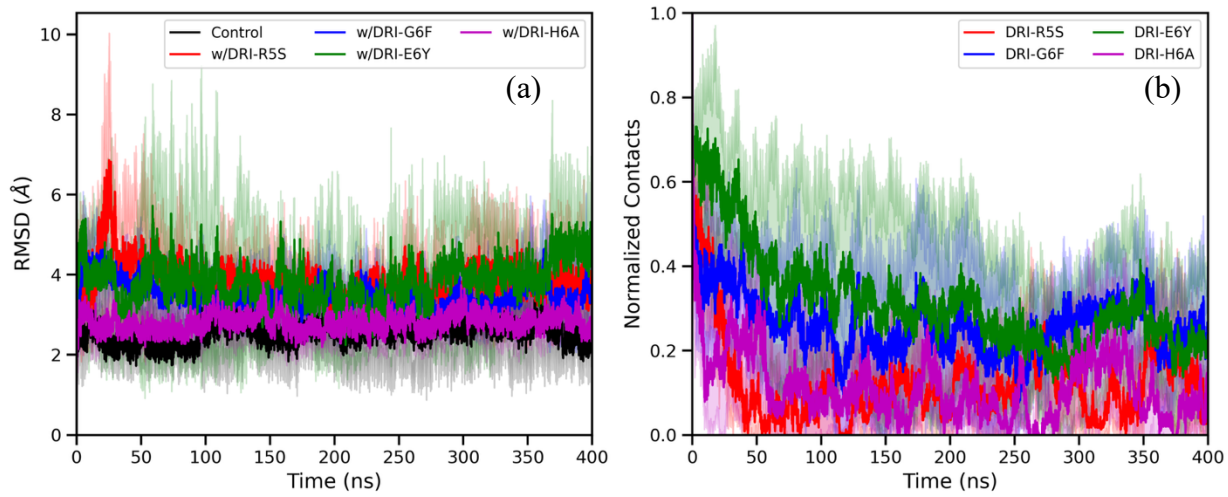

Figure 8: (a) Average backbone RMSD of collagen 1α in the presence and absence of DRI-peptides. **(b)** Average normalized contacts between DRI-peptides and collagen 1α over the course of the simulations. Contacts are normalized to the initial frame of the simulations. Shaded regions indicate the standard deviation.

Table 4: Average normalized final total SASA, hydrophobic SASA, and hydrophilic SASA of collagen 1α in the presence and absence of DRI-Peptides

System	Total SASA	Hydrophobic SASA	Hydrophilic SASA
Control	1.011 ± 0.009	0.950 ± 0.008	1.12 ± 0.02
DRI-R5S	0.96 ± 0.05	0.95 ± 0.05	0.96 ± 0.08
DRI-G6F	0.92 ± 0.06	0.92 ± 0.04	0.9 ± 0.1
DRI-E6Y	1.0 ± 0.2	1.0 ± 0.2	1.1 ± 0.2
DRI-H6A	0.89 ± 0.02	0.88 ± 0.04	0.914 ± 0.009

SASA was calculated for the collagen 1α simulations, the final average normalized values are shown in **Table 4**. When observing the normalized SAA of collagen 1α in the presence and absence of DRI-peptides we note that the final total SASA is very similar to the initial values, with the exception for DRI-H6A which has ~10% less total SASA. Indicating the systems are maintaining their compactness. This observation is further supported by the normalized hydrophobic surface area. In all systems, besides DRI-E6Y, there is a slight decrease in hydrophobic SASA meaning

less hydrophobic residues are exposed resulting in more compact structures. Overall, the effect that the DRI-peptide inhibitor candidates have on collagen 1α stability is very minimal.

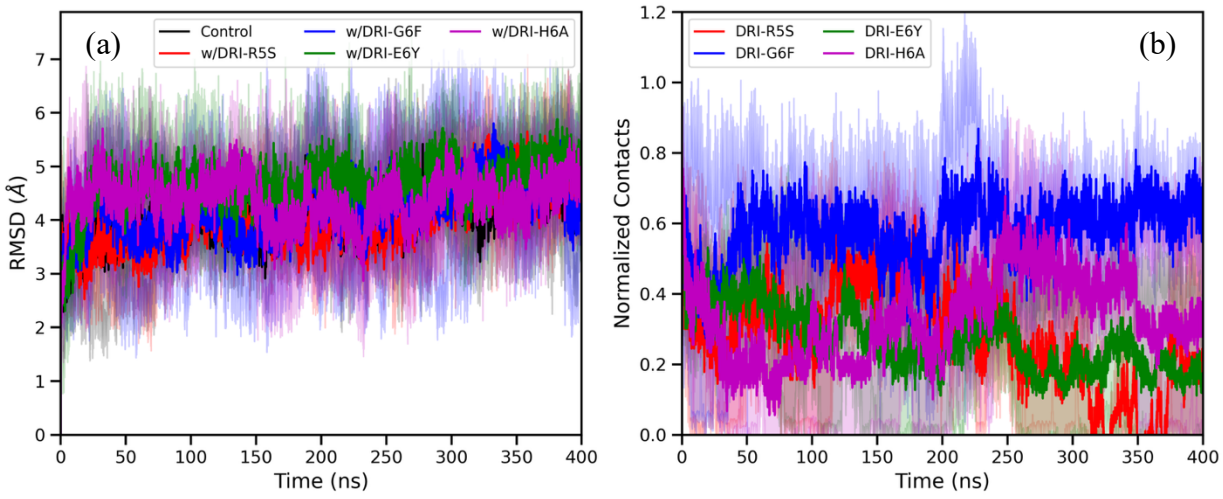

Figure 9: (a) Average backbone RMSD of fibronectin in the presence and absence of DRI-peptides. **(b)** Average normalized contacts between DRI-peptides and collagen 1a over the course of the simulations. Contacts are normalized to the initial frame of the simulations. Shaded regions indicate the standard deviation.

We similarly evaluated the effects of the DRI-peptide inhibitor candidates on the off-target molecule fibronectin. We bean by calculating the global backbone RMSD of all systems simulated, **Figure 9a**. From this figure the overall structure of the fibronectin varies little between the control simulations and the peptide simulations. Indicating there is minimal effects on overall structure deviations in the presence of the DRI-peptides. To gain a better understanding of the interactions between fibronectin and the DRI-peptides, normalized contacts were calculated. **Figure 9b** shows the average normalized contacts over the simulations. We note a clear difference in contacts with DRI-G6F and the other peptides. DRI-G6F has on average ~70% of the number contacts in the initial frame, while the remaining peptides have less than ~40%. DRI-G6F seems to have a higher

affinity for fibronectin than the other peptides. As fibronectin is an off-target, this higher affinity is a possible concern for off-target effects.

Similarly, as was done for collagen 1a the total SASA, hydrophobic SASA, and hydrophilic SASA was calculated for fibronectin. Overall, the effect of the DRI-peptide on fibronectin SASA is very minimal as shown in the average normalized final values reported in **Table 5**.

Table 5: Average normalized final total SASA, hydrophobic SASA, and hydrophilic SASA of fibronectin in the presence and absence of DRI-Peptides

System	Total SASA	Hydrophobic SASA	Hydrophilic SASA
Control	0.99 ± 0.02	1.18 ± 0.07	0.88 ± 0.02
DRI-R5S	0.98 ± 0.02	1.10 ± 0.02	0.90 ± 0.03
DRI-G6F	1.01 ± 0.02	1.09 ± 0.01	0.95 ± 0.02
DRI-E6Y	0.98 ± 0.03	1.08 ± 0.04	0.91 ± 0.03
DRI-H6A	0.974 ± 0.005	1.06 ± 0.01	0.92 ± 0.01

To evaluate the binding affinity of the DRI-peptide inhibitor candidates against mouse SAA3, collagen 1a, and fibronectin the average binding free energy was calculated over the last 100ns of all stimulations, **Table 6**.

Table 6: Average binding free energy calculated for the last 100ns of simulations.

Peptides	Binding Free Energy last 100ns (kJ/mol)		
	SAA3	Collagen 1α	Fibronectin
DRI-R5S	-16 ± 1	-8 ± 2	-10 ± 3
DRI-G6F	-19 ± 1	-12 ± 2	-17.1 ± 0.1
DRI-E6Y	-18.2 ± 0.5	-9 ± 2	-11 ± 4
DRI-H6A	-18 ± 2	-9 ± 2	-14 ± 2

For all peptides, the binding free energy against mouse SAA3 had a larger magnitude compared with the off-target molecules. Indicating the peptides have higher preferential affinity for the SAA3 fibril model. As mentioned previously, we note an increased binding free energy for DRI-G6F with fibronectin compared to the other peptides. Additionally, the difference in binding free energies between DRI-G6F & SAA3 and DRI-G6F & fibronectin is approximately 2 kJ/mol. This small difference may indicate that the DRI-G6F peptide will bind with either molecule. It should be mentioned that the free energy calculation method utilized has limitations. For instance, if a segment maintains contacts with the target molecule for the entire interval the free energy is calculated than the resulting free energy is infinite by the methods definition and cannot be included in the averaging. For the simulations of DRI-G6F with SAA3, 2-3 segments in each of the three simulations performed maintained contacts throughout, as a result the reported free energy is likely an underestimate of the actual binding energy.

Conclusion

From our extensive molecular dynamic simulations of mouse SAA3 with DRI-R5S, and newly identified DRI-G6F, DRI-E6Y, and DRI-H6A we have observed the effects these peptides have on the stability of the fibril model. In the presence of DRI-G6F, the SAA3 fibril maintains its structure and is the most stable. However, this increased stability may allow for further aggregation of SAA3 in more elongated fibrils. That along with the increased binding affinity for fibronectin and collagen 1α compared with the other peptides, leads to suggesting DRI-G6F not to be further studied as a potential inhibitor candidate. As observed experimentally, DRI-R5S was shown to decrease the fibril stability, leading to increased solvent accessible surface area and increased global RMSD. SAA3 in the presence of DRI-H6A showed decreased fibril stability as well as increased flexibility in protofibril 1. Additionally, an increase of hydrophobic SASA was observed.

However, the normalized contacts between DRI-H6A and SAA3 indicate that DRI-H6A interacts less than the other peptides tested. For further evaluation, mutational studies to increase this specificity should be performed. All peptides identified showed little effect on the off-target molecules from our extensive molecular dynamics of collagen 1α and fibronectin.

Acknowledgements

The simulations in this work were done using ACCESS resources allocated under grant MCB160005 (National Science Foundation) and were performed on the SDSC Expanse GPU partition. Analysis of trajectories was performed on the SCHOONER cluster of the University of Oklahoma.

Chapter 8 – Summary

In the presented work, I have investigated the effects of small peptides of various origins on amyloid aggregation. Initially motivated by the COVID-19 pandemic, my research began by focusing on the interactions of two amyloidogenic SARS-CoV-2 proteins, SK9 and FI10, on amylin, the amyloid protein associated with type II diabetes. From my simulations of amylin monomer within aqueous solution in the presence of SK9 and FI10, a secondary structure stabilizing effect was observed. These results were validated by our experimental collaborators, in which CD spectra of amylin in the presence of SK9 or FI10 remained in α-helical conformations. Additionally, our collaborators noted differential effects on amylin in the presence of SK9 and FI10 within a membrane environment. This effect indicated SK9 promotes accelerated formation of fibril aggregates, while FI10 stabilized the formation of smaller oligomeric structures which proved to be more cytotoxic. These results may provide a plausible mechanism for the increased cases of type II diabetes observed following contraction of SARS-CoV-2.

To further explore the effect of SK9 and FI10 on amyloid proteins, we investigated their effects on α-synuclein, the amyloid protein associated with Parkinson's disease. In the presence of SK9 and FI10, α-synuclein monomers showed a shift in their conformational ensemble towards more aggregation prone structures. This effect was shown to be higher in the presence FI10. Additionally, we observed an effect on fibril stability. FI10 was shown to preferentially enhance the stability of the rod polymorph of α-synuclein. As we continue post the COVID-19 pandemic, the long-term effects of SARS-CoV-2 infections are not known. With the many overlapping symptoms between individuals suffering from neurodegenerative disease and Long-COVID[9,10,16], this work has shown some possible interactions between SARS-CoV-2 and amyloid proteins that

may provide a plausible mechanism for some of these overlaps. However, to further explore the possible interactions with SARS-CoV-2 other amyloid protein need to be investigated. For instance, one of the key proteins associated in Alzheimer's, amyloid-β. In these projects we have only evaluated the effect of the viral protein segments on monomers or fully formed fibrils. To fully explore the effects on amyloid aggregation studies focusing on early aggregation need to be performed.

The latter half of the research that was performed during my graduate career, again, focused on amyloid protein and the interactions with small peptides. However, in this research the aim was to determine peptides that could destabilize amyloid fibrils and inhibit their aggregation. This research was motivated greatly by the successful implantation of DRI-R5S as a treatment in mice following myocardial infarction. I sought to identify new potential DRI-peptide inhibitors for mouse SAA3 via virtual screening and molecular dynamics. From this virtual screening three new peptides were identified, DRI-GSFFS (DRI-G6F), DRI-ERGFFY (DRI-E6Y), and DRI-HFVWIA (DRI-H6A). These peptides along with DRI-R5S, were simulated with a mouse SAA3 fibril model. Simulations of DRI-R5S and DRI-H6A showed decreased fibril stability compared with the other peptides tested. The results observed with the DRI-R5S peptides further support those observed in the mice experiments of Cimini et al.[20] It was noted that DRI-H6A had decreased contact frequency compared with the other peptides tested. In the future, computational mutational studies should be performed to increase this specificity. Additionally, these peptides identified should be simulated with SAA3 monomers to evaluate the effects of early aggregation events. To further validate the results the peptides should be evaluated *in vitro* as performed by Cimini et. al.

This research has only begun to scratch the surface of possible effect of small peptides have on amyloid aggregation. I hope the work presented here may provide a steppingstone for future researchers in the field.

List of Publications Related to Dissertation

1) Jana, A. K.; Lander, C. W.; **Chesney, A. D.**; Hansmann, U. H. E. Effect of an Amyloidogenic SARS-COV-2 Protein Fragment on α-Synuclein Monomers and Fibrils. *J. Phys. Chem. B* **2022**, *126* (20), 3648–3658. https://doi.org/10.1021/acs.jpcb.2c01254.

2) **Chesney, A. D.**; Maiti, B.; Hansmann, U. H. E. SARS-COV-2 Spike Protein Fragment Eases Amyloidogenesis of α-Synuclein. *J. Chem. Phys.* **2023**, *159* (1), 015103. https://doi.org/10.1063/5.0157331

3) **Chesney, A. D.**; Maiti, B.; Hansmann, U. H. E. Human Amylin in the Presence of SARS-COV-2 Protein Fragments. *ACS Omega* **2023**, *8* (13), 12501–12511. https://doi.org/10.1021/acsomega.3c00621.

4) Zhang, J.; Mesias, V. St. D.; **Chesney, A. D.**; Anand, V. K.; Feng, X.; Hsing, I.-M.; Hansmann, U. H. E.; Huang, J. Differential Effects of SARS-CoV-2 Amyloidogenic Segments on the Aggregation and Toxicity of Human Islet Amyloid Polypeptide within Membrane Environments. *Int. J. Biol. Macromol.* **2024**, *283*, 137930. https://doi.org/10.1016/j.ijbiomac.2024.137930.

5) M. Cimini, U.H.E. Hansmann, C. Gonzales, **A.D. Chesney**, M.M. Truongcao, E. Gao,T. Wang, R. Roy,E. Forte, V. Mallaredy, C. Thej, A. Magadum, D. Joladarashi, C. Benedict, W.J. Koch, C. Tukel and R. Kishore, *Podoplanin Positive Cell-derived Small Extracellular Vesicles Contribute to Cardiac Amyloidosis After Myocardial Infarction*, Cell Rep. **44** (2025),105408.

Other Publications

1) Pan, X.; Snyder, R.; Wang, J.; Lander, C.; Wickizer, C.; Van, R.; **Chesney, A**.; Xue, Y.; Mao, Y.; Mei, Y.; Pu, J.; Shao, Y. Training Machine Learning Potentials for Reactive Systems: A Colab Tutorial on Basic Models. *J. Comput. Chem.* **2024**, jcc.27269. https://doi.org/10.1002/jcc.27269.

References

(1) Buxbaum, J. N.; Eisenberg ,David S.; Fändrich ,Marcus; McPhail ,Ellen D.; Merlini ,Giampaolo; Saraiva ,Maria J. M.; Sekijima ,Yoshiki; and Westermark, P. Amyloid Nomenclature 2024: Update, Novel Proteins, and Recommendations by the International Society of Amyloidosis (ISA) Nomenclature Committee. *Amyloid* **2024**, *31* (4), 249–256. https://doi.org/10.1080/13506129.2024.2405948.

(2) Greenwald, J.; Riek, R. Biology of Amyloid: Structure, Function, and Regulation. *Structure* **2010**, *18* (10), 1244–1260. https://doi.org/10.1016/j.str.2010.08.009.

(3) Flagmeier, P.; Meisl, G.; Vendruscolo, M.; Knowles, T. P. J.; Dobson, C. M.; Buell, A. K.; Galvagnion, C. Mutations Associated with Familial Parkinson's Disease Alter the Initiation and Amplification Steps of α-Synuclein Aggregation. *Proc. Natl. Acad. Sci.* **2016**, *113* (37), 10328–10333. https://doi.org/10.1073/pnas.1604645113.

(4) Hassan, S.; White, K.; Terry, C. Linking hIAPP Misfolding and Aggregation with Type 2 Diabetes Mellitus: A Structural Perspective. *Biosci. Rep.* **2022**, *42* (5), BSR20211297. https://doi.org/10.1042/BSR20211297.

(5) Press, M.; Jung, T.; König, J.; Grune, T.; Höhn, A. Protein Aggregates and Proteostasis in Aging: Amylin and β-Cell Function. *Mech. Ageing Dev.* **2019**, *177*, 46–54. https://doi.org/10.1016/j.mad.2018.03.010.

(6) Bendor, J.; Logan, T.; Edwards, R. H. The Function of α-Synuclein. *Neuron* **2013**, *79* (6), 10.1016/j.neuron.2013.09.004. https://doi.org/10.1016/j.neuron.2013.09.004.

(7) *COVID-19 deaths | WHO COVID-19 dashboard*. datadot. https://data.who.int/dashboards/covid19/cases (accessed 2025-05-23).

(8) *Coronavirus disease (COVID-19): Post COVID-19 condition*. https://www.who.int/news-room/questions-and-answers/item/coronavirus-disease-(covid-19)-post-covid-19-condition (accessed 2025-05-23).

(9) Davis, H. E.; McCorkell, L.; Vogel, J. M.; Topol, E. J. Long COVID: Major Findings, Mechanisms and Recommendations. *Nat. Rev. Microbiol.* **2023**, *21* (3), 133–146. https://doi.org/10.1038/s41579-022-00846-2.

(10) Davis, H. E.; Assaf, G. S.; McCorkell, L.; Wei, H.; Low, R. J.; Re'em, Y.; Redfield, S.; Austin, J. P.; Akrami, A. Characterizing Long COVID in an International Cohort: 7 Months of Symptoms and Their Impact. *eClinicalMedicine* **2021**, *38*, 101019. https://doi.org/10.1016/j.eclinm.2021.101019.

(11) Xie, Y.; Al-Aly, Z. Risks and Burdens of Incident Diabetes in Long COVID: A Cohort Study. *Lancet Diabetes Endocrinol.* **2022**, *10* (5), 311–321. https://doi.org/10.1016/S2213-8587(22)00044-4.

(12) Xie, Y.; Xu, E.; Bowe, B.; Al-Aly, Z. Long-Term Cardiovascular Outcomes of COVID-19. *Nat. Med.* **2022**, *28* (3), 583–590. https://doi.org/10.1038/s41591-022-01689-3.

(13) Mancini, D. M.; Brunjes, D. L.; Lala, A.; Trivieri, M. G.; Contreras, J. P.; Natelson, B. H. Use of Cardiopulmonary Stress Testing for Patients With Unexplained Dyspnea Post–Coronavirus Disease. *JACC Heart Fail.* **2021**, *9* (12), 927–937. https://doi.org/10.1016/j.jchf.2021.10.002.

(14) Kedor, C.; Freitag, H.; Meyer-Arndt, L.; Wittke, K.; Hanitsch, L. G.; Zoller, T.; Steinbeis, F.; Haffke, M.; Rudolf, G.; Heidecker, B.; Bobbert, T.; Spranger, J.; Volk, H.-D.; Skurk, C.; Konietschke, F.; Paul, F.; Behrends, U.; Bellmann-Strobl, J.; Scheibenbogen, C. A Prospective Observational Study of Post-COVID-19 Chronic Fatigue Syndrome Following

the First Pandemic Wave in Germany and Biomarkers Associated with Symptom Severity. *Nat. Commun.* **2022**, *13* (1), 5104. https://doi.org/10.1038/s41467-022-32507-6.
(15) Larsen, N. W.; Stiles, L. E.; Shaik, R.; Schneider, L.; Muppidi, S.; Tsui, C. T.; Geng, L. N.; Bonilla, H.; Miglis, M. G. Characterization of Autonomic Symptom Burden in Long COVID: A Global Survey of 2,314 Adults. *Front. Neurol.* **2022**, *13*. https://doi.org/10.3389/fneur.2022.1012668.
(16) Hammarström, P.; and Nyström, S. Viruses and Amyloids - a Vicious Liaison. *Prion* **2023**, *17* (1), 82–104. https://doi.org/10.1080/19336896.2023.2194212.
(17) Hammarström, P.; and Nyström, S. Viruses and Amyloids - a Vicious Liaison. *Prion* **2023**, *17* (1), 82–104. https://doi.org/10.1080/19336896.2023.2194212.
(18) Ghosh, A.; Pithadia, A. S.; Bhat, J.; Bera, S.; Midya, A.; Fierke, C. A.; Ramamoorthy, A.; Bhunia, A. Self-Assembly of a Nine-Residue Amyloid-Forming Peptide Fragment of SARS Corona Virus E-Protein: Mechanism of Self Aggregation and Amyloid-Inhibition of hIAPP. *Biochemistry* **2015**, *54* (13), 2249–2261. https://doi.org/10.1021/acs.biochem.5b00061.
(19) Nyström, S.; Hammarström, P. Amyloidogenesis of SARS-CoV-2 Spike Protein. *J. Am. Chem. Soc.* **2022**, *144* (20), 8945–8950. https://doi.org/10.1021/jacs.2c03925.
(20) Cimini, M.; Hansmann, U. H. E.; Gonzalez, C.; Chesney, A. D.; Truongcao, M. M.; Gao, E.; Wang, T.; Roy, R.; Forte, E.; Mallaredy, V.; Thej, C.; Magadum, A.; Joladarashi, D.; Benedict, C.; Koch, W. J.; Tükel, Ç.; Kishore, R. Podoplanin-Positive Cell-Derived Small Extracellular Vesicles Contribute to Cardiac Amyloidosis after Myocardial Infarction. *Cell Rep.* **2025**, *44* (3), 115408. https://doi.org/10.1016/j.celrep.2025.115408.
(21) Jana, A. K.; Greenwood, A. B.; Hansmann, U. H. E. Small Peptides for Inhibiting Serum Amyloid A Aggregation. *ACS Med. Chem. Lett.* **2021**, *12* (10), 1613–1621. https://doi.org/10.1021/acsmedchemlett.1c00456.
(22) Goodman, M.; Chorev, M. On the Concept of Linear Modified Retro-Peptide Structures. *Acc. Chem. Res.* **1979**, *12* (1), 1–7. https://doi.org/10.1021/ar50133a001.
(23) Lau, J. L.; Dunn, M. K. Therapeutic Peptides: Historical Perspectives, Current Development Trends, and Future Directions. *Bioorg. Med. Chem.* **2018**, *26* (10), 2700–2707. https://doi.org/10.1016/j.bmc.2017.06.052.
(24) Gandbhir, O.; Sundaram, P. Pre-Clinical Safety and Efficacy Evaluation of Amytrap, a Novel Therapeutic to Treat Alzheimer's Disease. *J. Alzheimers Dis. Rep.* **2019**, *3* (1), 77–94. https://doi.org/10.3233/ADR-190107.
(25) Gregori, M.; Taylor, M.; Salvati, E.; Re, F.; Mancini, S.; Balducci, C.; Forloni, G.; Zambelli, V.; Sesana, S.; Michael, M.; Michail, C.; Tinker-Mill, C.; Kolosov, O.; Sherer, M.; Harris, S.; Fullwood, N. J.; Masserini, M.; Allsop, D. Retro-Inverso Peptide Inhibitor Nanoparticles as Potent Inhibitors of Aggregation of the Alzheimer's Aβ Peptide. *Nanomedicine Nanotechnol. Biol. Med.* **2017**, *13* (2), 723–732. https://doi.org/10.1016/j.nano.2016.10.006.
(26) Parthsarathy, V.; McClean, P. L.; Hölscher, C.; Taylor, M.; Tinker, C.; Jones, G.; Kolosov, O.; Salvati, E.; Gregori, M.; Masserini, M.; Allsop, D. A Novel Retro-Inverso Peptide Inhibitor Reduces Amyloid Deposition, Oxidation and Inflammation and Stimulates Neurogenesis in the APPswe/PS1ΔE9 Mouse Model of Alzheimer's Disease. *PLOS ONE* **2013**, *8* (1), e54769. https://doi.org/10.1371/journal.pone.0054769.
(27) MacKerell, A. D. Jr.; Bashford, D.; Bellott, M.; Dunbrack, R. L. Jr.; Evanseck, J. D.; Field, M. J.; Fischer, S.; Gao, J.; Guo, H.; Ha, S.; Joseph-McCarthy, D.; Kuchnir, L.; Kuczera, K.;

Lau, F. T. K.; Mattos, C.; Michnick, S.; Ngo, T.; Nguyen, D. T.; Prodhom, B.; Reiher, W. E.; Roux, B.; Schlenkrich, M.; Smith, J. C.; Stote, R.; Straub, J.; Watanabe, M.; Wiórkiewicz-Kuczera, J.; Yin, D.; Karplus, M. All-Atom Empirical Potential for Molecular Modeling and Dynamics Studies of Proteins. *J. Phys. Chem. B* **1998**, *102* (18), 3586–3616. https://doi.org/10.1021/jp973084f.

(28) Chesney, A. D.; Maiti, B.; Hansmann, U. H. E. Human Amylin in the Presence of SARS-COV-2 Protein Fragments. *ACS Omega* **2023**, *8* (13), 12501–12511. https://doi.org/10.1021/acsomega.3c00621.

(29) Shi, S.; Qin, M.; Shen, B.; Cai, Y.; Liu, T.; Yang, F.; Gong, W.; Liu, X.; Liang, J.; Zhao, Q.; Huang, H.; Yang, B.; Huang, C. Association of Cardiac Injury With Mortality in Hospitalized Patients With COVID-19 in Wuhan, China. *JAMA Cardiol.* **2020**, *5* (7), 802. https://doi.org/10.1001/jamacardio.2020.0950.

(30) Sheraton, M.; Deo, N.; Kashyap, R.; Surani, S. A Review of Neurological Complications of COVID-19. *Cureus* **2020**. https://doi.org/10.7759/cureus.8192.

(31) Su, H.; Yang, M.; Wan, C.; Yi, L.-X.; Tang, F.; Zhu, H.-Y.; Yi, F.; Yang, H.-C.; Fogo, A. B.; Nie, X.; Zhang, C. Renal Histopathological Analysis of 26 Postmortem Findings of Patients with COVID-19 in China. *Kidney Int.* **2020**, *98* (1), 219–227. https://doi.org/10.1016/j.kint.2020.04.003.

(32) Morris, S. B.; Schwartz, N. G.; Patel, P.; Abbo, L.; Beauchamps, L.; Balan, S.; Lee, E. H.; Paneth-Pollak, R.; Geevarughese, A.; Lash, M. K.; Dorsinville, M. S.; Ballen, V.; Eiras, D. P.; Newton-Cheh, C.; Smith, E.; Robinson, S.; Stogsdill, P.; Lim, S.; Fox, S. E.; Richardson, G.; Hand, J.; Oliver, N. T.; Kofman, A.; Bryant, B.; Ende, Z.; Datta, D.; Belay, E.; Godfred-Cato, S. Case Series of Multisystem Inflammatory Syndrome in Adults Associated with SARS-CoV-2 Infection — United Kingdom and United States, March–August 2020. *MMWR Morb. Mortal. Wkly. Rep.* **2020**, *69* (40), 1450–1456. https://doi.org/10.15585/mmwr.mm6940e1.

(33) Beliard, K. A.; Yau, M.; Wilkes, M.; Romero, C. J.; Wallach, E.; Rapaport, R. SARS-CoV-2 Infection Related Diabetes Mellitus. *J. Endocr. Soc.* **2021**, *5* (Supplement_1), A397–A397. https://doi.org/10.1210/jendso/bvab048.808.

(34) Hollstein, T.; Schulte, D. M.; Schulz, J.; Glück, A.; Ziegler, A. G.; Bonifacio, E.; Wendorff, M.; Franke, A.; Schreiber, S.; Bornstein, S. R.; Laudes, M. Autoantibody-Negative Insulin-Dependent Diabetes Mellitus after SARS-CoV-2 Infection: A Case Report. *Nat. Metab.* **2020**, *2* (10), 1021–1024. https://doi.org/10.1038/s42255-020-00281-8.

(35) Moreno, D. M.; Ramos, R. J. A.; Fernández, L. G.; Montenegro, A. M. R.; González, M. M.; Torrecilla, N. B.; Albarrán, O. G. Clinical/Biochemical Characteristics and Related Outcomes in People with New-onset Diabetes and COVID -19: Experience from a Single Centre. *Pract. Diabetes* **2022**, *39* (6), 24–31. https://doi.org/10.1002/pdi.2426.

(36) Hayden, M. R. An Immediate and Long-Term Complication of COVID-19 May Be Type 2 Diabetes Mellitus: The Central Role of β-Cell Dysfunction, Apoptosis and Exploration of Possible Mechanisms. *Cells* **2020**, *9* (11), 2475. https://doi.org/10.3390/cells9112475.

(37) Jana, A. K.; Greenwood, A. B.; Hansmann, U. H. E. Presence of a SARS-CoV-2 Protein Enhances Amyloid Formation of Serum Amyloid A. *J. Phys. Chem. B* **2021**, *125* (32), 9155–9167. https://doi.org/10.1021/acs.jpcb.1c04871.

(38) Jana, A. K.; Lander, C. W.; Chesney, A. D.; Hansmann, U. H. E. Effect of an Amyloidogenic SARS-COV-2 Protein Fragment on α-Synuclein Monomers and Fibrils. *J. Phys. Chem. B* **2022**, *126* (20), 3648–3658. https://doi.org/10.1021/acs.jpcb.2c01254.

(39) Kryshtafovych, A.; Moult, J.; Billings, W. M.; Della Corte, D.; Fidelis, K.; Kwon, S.; Olechnovič, K.; Seok, C.; Venclovas, Č.; Won, J.; CASP-COVID participants. Modeling SARS-CoV-2 Proteins in the CASP-commons Experiment. *Proteins Struct. Funct. Bioinforma.* **2021**, *89* (12), 1987–1996. https://doi.org/10.1002/prot.26231.
(40) Nyström, S.; Hammarström, P. *Amyloidogenesis of SARS-CoV-2 Spike Protein*; preprint; Biochemistry, 2021. https://doi.org/10.1101/2021.12.16.472920.
(41) Nanga, R. P. R.; Brender, J. R.; Vivekanandan, S.; Ramamoorthy, A. Structure and Membrane Orientation of IAPP in Its Natively Amidated Form at Physiological pH in a Membrane Environment. *Biochim. Biophys. Acta BBA - Biomembr.* **2011**, *1808* (10), 2337–2342. https://doi.org/10.1016/j.bbamem.2011.06.012.
(42) Wiltzius, J. J. W.; Sievers, S. A.; Sawaya, M. R.; Cascio, D.; Popov, D.; Riekel, C.; Eisenberg, D. Atomic Structure of the Cross-β Spine of Islet Amyloid Polypeptide (Amylin). *Protein Sci.* **2008**, *17* (9), 1467–1474. https://doi.org/10.1110/ps.036509.108.
(43) Pandey, P.; Nguyen, N.; Hansmann, U. H. E. \textlessspan Style="font-Variant:Small-Caps;"\textgreaterd\textless/Span\textgreater -Retro Inverso Amylin and the Stability of Amylin Fibrils. *J. Chem. Theory Comput.* **2020**, *16* (8), 5358–5368. https://doi.org/10.1021/acs.jctc.0c00523.
(44) Gallardo, R.; Iadanza, M. G.; Xu, Y.; Heath, G. R.; Foster, R.; Radford, S. E.; Ranson, N. A. Fibril Structures of Diabetes-Related Amylin Variants Reveal a Basis for Surface-Templated Assembly. *Nat. Struct. Mol. Biol.* **2020**, *27* (11), 1048–1056. https://doi.org/10.1038/s41594-020-0496-3.
(45) Mesias, V. St. D.; Zhu, H.; Tang, X.; Dai, X.; Liu, W.; Guo, Y.; Huang, J. Moderate Binding between Two SARS-CoV-2 Protein Segments and α-Synuclein Alters Its Toxic Oligomerization Propensity Differently. *J. Phys. Chem. Lett.* **2022**, *13* (45), 10642–10648. https://doi.org/10.1021/acs.jpclett.2c02278.
(46) Trott, O.; Olson, A. J. AutoDock Vina: Improving the Speed and Accuracy of Docking with a New Scoring Function, Efficient Optimization, and Multithreading. *J. Comput. Chem.* **2009**, NA-NA. https://doi.org/10.1002/jcc.21334.
(47) Van Zundert, G. C. P.; Rodrigues, J. P. G. L. M.; Trellet, M.; Schmitz, C.; Kastritis, P. L.; Karaca, E.; Melquiond, A. S. J.; Van Dijk, M.; De Vries, S. J.; Bonvin, A. M. J. J. The HADDOCK2.2 Web Server: User-Friendly Integrative Modeling of Biomolecular Complexes. *J. Mol. Biol.* **2016**, *428* (4), 720–725. https://doi.org/10.1016/j.jmb.2015.09.014.
(48) Honorato, R. V.; Koukos, P. I.; Jiménez-García, B.; Tsaregorodtsev, A.; Verlato, M.; Giachetti, A.; Rosato, A.; Bonvin, A. M. J. J. Structural Biology in the Clouds: The WeNMR-EOSC Ecosystem. *Front. Mol. Biosci.* **2021**, *8*, 729513. https://doi.org/10.3389/fmolb.2021.729513.
(49) Abraham, M. J.; Murtola, T.; Schulz, R.; Páll, S.; Smith, J. C.; Hess, B.; Lindahl, E. GROMACS: High Performance Molecular Simulations through Multi-Level Parallelism from Laptops to Supercomputers. *SoftwareX* **2015**, *1–2*, 19–25. https://doi.org/10.1016/j.softx.2015.06.001.
(50) Huang, J.; Rauscher, S.; Nawrocki, G.; Ran, T.; Feig, M.; De Groot, B. L.; Grubmüller, H.; MacKerell, A. D. CHARMM36m: An Improved Force Field for Folded and Intrinsically Disordered Proteins. *Nat. Methods* **2017**, *14* (1), 71–73. https://doi.org/10.1038/nmeth.4067.

(51) Jorgensen, W. L.; Chandrasekhar, J.; Madura, J. D.; Impey, R. W.; Klein, M. L. Comparison of Simple Potential Functions for Simulating Liquid Water. *J. Chem. Phys.* **1983**, *79* (2), 926–935. https://doi.org/10.1063/1.445869.
(52) Wang, W.; Hansmann, U. H. E. Stability of Human Serum Amyloid A Fibrils. *J. Phys. Chem. B* **2020**, *124* (47), 10708–10717. https://doi.org/10.1021/acs.jpcb.0c08280.
(53) Siwy, C. M.; Lockhart, C.; Klimov, D. K. Is the Conformational Ensemble of Alzheimer's Aβ10-40 Peptide Force Field Dependent? *PLOS Comput. Biol.* **2017**, *13* (1), e1005314. https://doi.org/10.1371/journal.pcbi.1005314.
(54) Samantray, S.; Yin, F.; Kav, B.; Strodel, B. Different Force Fields Give Rise to Different Amyloid Aggregation Pathways in Molecular Dynamics Simulations. *J. Chem. Inf. Model.* **2020**, *60* (12), 6462–6475. https://doi.org/10.1021/acs.jcim.0c01063.
(55) Man, V. H.; He, X.; Derreumaux, P.; Ji, B.; Xie, X.-Q.; Nguyen, P. H.; Wang, J. Effects of All-Atom Molecular Mechanics Force Fields on Amyloid Peptide Assembly: The Case of Aβ $_{16–22}$ Dimer. *J. Chem. Theory Comput.* **2019**, *15* (2), 1440–1452. https://doi.org/10.1021/acs.jctc.8b01107.
(56) Bussi, G.; Donadio, D.; Parrinello, M. Canonical Sampling through Velocity Rescaling. *J. Chem. Phys.* **2007**, *126* (1), 014101. https://doi.org/10.1063/1.2408420.
(57) Parrinello, M.; Rahman, A. Polymorphic Transitions in Single Crystals: A New Molecular Dynamics Method. *J. Appl. Phys.* **1981**, *52* (12), 7182–7190. https://doi.org/10.1063/1.328693.
(58) Miyamoto, S.; Kollman, P. A. Settle: An Analytical Version of the SHAKE and RATTLE Algorithm for Rigid Water Models. *J. Comput. Chem.* **1992**, *13* (8), 952–962. https://doi.org/10.1002/jcc.540130805.
(59) Hess, B.; Bekker, H.; Berendsen, H. J. C.; Fraaije, J. G. E. M. LINCS: A Linear Constraint Solver for Molecular Simulations. *J. Comput. Chem.* **1997**, *18* (12), 1463–1472. https://doi.org/10.1002/(SICI)1096-987X(199709)18:12<1463::AID-JCC4>3.0.CO;2-H.
(60) Humphrey, W.; Dalke, A.; Schulten, K. VMD: Visual Molecular Dynamics. *J. Mol. Graph.* **1996**, *14* (1), 33–38. https://doi.org/10.1016/0263-7855(96)00018-5.
(61) McGibbon, R. T.; Beauchamp, K. A.; Harrigan, M. P.; Klein, C.; Swails, J. M.; Hernández, C. X.; Schwantes, C. R.; Wang, L.-P.; Lane, T. J.; Pande, V. S. MDTraj: A Modern Open Library for the Analysis of Molecular Dynamics Trajectories. *Biophys. J.* **2015**, *109* (8), 1528–1532. https://doi.org/10.1016/j.bpj.2015.08.015.
(62) Pettersen, E. F.; Goddard, T. D.; Huang, C. C.; Couch, G. S.; Greenblatt, D. M.; Meng, E. C.; Ferrin, T. E. UCSF Chimera—A Visualization System for Exploratory Research and Analysis. *J. Comput. Chem.* **2004**, *25* (13), 1605–1612. https://doi.org/10.1002/jcc.20084.
(63) Frishman, D.; Argos, P. Knowledge-Based Protein Secondary Structure Assignment. *Proteins Struct. Funct. Genet.* **1995**, *23* (4), 566–579. https://doi.org/10.1002/prot.340230412.
(64) Kumari, R.; Kumar, R.; Open Source Drug Discovery Consortium; Lynn, A. *G_mmpbsa* — A GROMACS Tool for High-Throughput MM-PBSA Calculations. *J. Chem. Inf. Model.* **2014**, *54* (7), 1951–1962. https://doi.org/10.1021/ci500020m.
(65) Bellaiche, M. M. J.; Best, R. B. Molecular Determinants of Aβ $_{42}$ Adsorption to Amyloid Fibril Surfaces. *J. Phys. Chem. Lett.* **2018**, *9* (22), 6437–6443. https://doi.org/10.1021/acs.jpclett.8b02375.

(66) Leguizamon Herrera, V. L.; Buell, A. K.; Willbold, D.; Barz, B. Interaction of Therapeutic D -Peptides with Aβ42 Monomers, Thermodynamics, and Binding Analysis. *ACS Chem. Neurosci.* **2022**, *13* (11), 1638–1650. https://doi.org/10.1021/acschemneuro.2c00102.
(67) Xue, L. C.; Rodrigues, J. P.; Kastritis, P. L.; Bonvin, A. M.; Vangone, A. PRODIGY: A Web Server for Predicting the Binding Affinity of Protein–Protein Complexes. *Bioinformatics* **2016**, btw514. https://doi.org/10.1093/bioinformatics/btw514.
(68) Westermark, P.; Engström, U.; Johnson, K. H.; Westermark, G. T.; Betsholtz, C. Islet Amyloid Polypeptide: Pinpointing Amino Acid Residues Linked to Amyloid Fibril Formation. *Proc. Natl. Acad. Sci.* **1990**, *87* (13), 5036–5040. https://doi.org/10.1073/pnas.87.13.5036.
(69) Jaikaran, E. T. A. S.; Higham, C. E.; Serpell, L. C.; Zurdo, J.; Gross, M.; Clark, A.; Fraser, P. E. Identification of a Novel Human Islet Amyloid Polypeptide β-Sheet Domain and Factors Influencing Fibrillogenesis. *J. Mol. Biol.* **2001**, *308* (3), 515–525. https://doi.org/10.1006/jmbi.2001.4593.
(70) Thu, T. T. M.; Li, M. S. Protein Aggregation Rate Depends on Mechanical Stability of Fibrillar Structure. *J. Chem. Phys.* **2022**, *157* (5), 055101. https://doi.org/10.1063/5.0088689.
(71) Zhang, J.; Mesias, V. St. D.; Chesney, A. D.; Anand, V. K.; Feng, X.; Hsing, I.-M.; Hansmann, U. H. E.; Huang, J. Differential Effects of SARS-CoV-2 Amyloidogenic Segments on the Aggregation and Toxicity of Human Islet Amyloid Polypeptide within Membrane Environments. *Int. J. Biol. Macromol.* **2024**, *283*, 137930. https://doi.org/10.1016/j.ijbiomac.2024.137930.
(72) Chesney, A. D.; Maiti, B.; Hansmann, U. H. E. SARS-COV-2 Spike Protein Fragment Eases Amyloidogenesis of α-Synuclein. *J. Chem. Phys.* **2023**, *159* (1), 015103. https://doi.org/10.1063/5.0157331.
(73) Spillantini, M. G.; Schmidt, M. L.; Lee, V. M.-Y.; Trojanowski, J. Q.; Jakes, R.; Goedert, M. α-Synuclein in Lewy Bodies. *Nature* **1997**, *388* (6645), 839–840. https://doi.org/10.1038/42166.
(74) Viennet, T.; Wördehoff, M. M.; Uluca, B.; Poojari, C.; Shaykhalishahi, H.; Willbold, D.; Strodel, B.; Heise, H.; Buell, A. K.; Hoyer, W.; Etzkorn, M. Structural Insights from Lipid-Bilayer Nanodiscs Link α-Synuclein Membrane-Binding Modes to Amyloid Fibril Formation. *Commun. Biol.* **2018**, *1* (1), 44. https://doi.org/10.1038/s42003-018-0049-z.
(75) Owen, M. C.; Gnutt, D.; Gao, M.; Wärmländer, S. K. T. S.; Jarvet, J.; Gräslund, A.; Winter, R.; Ebbinghaus, S.; Strodel, B. Effects of *in Vivo* Conditions on Amyloid Aggregation. *Chem. Soc. Rev.* **2019**, *48* (14), 3946–3996. https://doi.org/10.1039/C8CS00034D.
(76) Frölich, L. Alzheimer's Disease – the 'Microbial Hypothesis' from a Clinical and Neuroimaging Perspective. *Psychiatry Res. Neuroimaging* **2020**, *306*, 111181. https://doi.org/10.1016/j.pscychresns.2020.111181.
(77) Seaks, C. E.; Wilcock, D. M. Infectious Hypothesis of Alzheimer Disease. *PLOS Pathog.* **2020**, *16* (11), e1008596. https://doi.org/10.1371/journal.ppat.1008596.
(78) Li, F.; Hearn, M.; Bennett, L. E. The Role of Microbial Infection in the Pathogenesis of Alzheimer's Disease and the Opportunity for Protection by Anti-Microbial Peptides. *Crit. Rev. Microbiol.* **2021**, *47* (2), 240–253. https://doi.org/10.1080/1040841X.2021.1876630.
(79) Eimer, W. A.; Vijaya Kumar, D. K.; Navalpur Shanmugam, N. K.; Rodriguez, A. S.; Mitchell, T.; Washicosky, K. J.; György, B.; Breakefield, X. O.; Tanzi, R. E.; Moir, R. D. Alzheimer's Disease-Associated β-Amyloid Is Rapidly Seeded by Herpesviridae to Protect

against Brain Infection. *Neuron* **2018**, *99* (1), 56-63.e3. https://doi.org/10.1016/j.neuron.2018.06.030.
(80) Leta, V.; Boura, I.; Van Wamelen, D. J.; Rodriguez-Violante, M.; Antonini, A.; Chaudhuri, K. R. Covid-19 and Parkinson's Disease: Acute Clinical Implications, Long-COVID and Post-COVID-19 Parkinsonism. In *International Review of Neurobiology*; Elsevier, 2022; Vol. 165, pp 63–89. https://doi.org/10.1016/bs.irn.2022.04.004.
(81) Ait Wahmane, S.; Achbani, A.; Ouhaz, Z.; Elatiqi, M.; Belmouden, A.; Nejmeddine, M. The Possible Protective Role of A-SYNUCLEIN Against Severe Acute Respiratory Syndrome Coronavirus 2 Infections in Patients With Parkinson's Disease. *Mov. Disord.* **2020**, *35* (8), 1293–1294. https://doi.org/10.1002/mds.28185.
(82) Semerdzhiev, S. A.; Fakhree, M. A. A.; Segers-Nolten, I.; Blum, C.; Claessens, M. M. A. E. Interactions between SARS-CoV-2 N-Protein and α-Synuclein Accelerate Amyloid Formation. *ACS Chem. Neurosci.* **2022**, *13* (1), 143–150. https://doi.org/10.1021/acschemneuro.1c00666.
(83) Ge, W.-Y.; Deng, X.; Shi, W.-P.; Lin, W.-J.; Chen, L.-L.; Liang, H.; Wang, X.-T.; Zhang, T.-D.; Zhao, F.-Z.; Guo, W.-H.; Yin, D.-C. Amyloid Protein Cross-Seeding Provides a New Perspective on Multiple Diseases *In Vivo*. *Biomacromolecules* **2023**, *24* (1), 1–18. https://doi.org/10.1021/acs.biomac.2c01233.
(84) Li, B.; Ge, P.; Murray, K. A.; Sheth, P.; Zhang, M.; Nair, G.; Sawaya, M. R.; Shin, W. S.; Boyer, D. R.; Ye, S.; Eisenberg, D. S.; Zhou, Z. H.; Jiang, L. Cryo-EM of Full-Length α-Synuclein Reveals Fibril Polymorphs with a Common Structural Kernel. *Nat. Commun.* **2018**, *9* (1), 3609. https://doi.org/10.1038/s41467-018-05971-2.
(85) Tuttle, M. D.; Comellas, G.; Nieuwkoop, A. J.; Covell, D. J.; Berthold, D. A.; Kloepper, K. D.; Courtney, J. M.; Kim, J. K.; Barclay, A. M.; Kendall, A.; Wan, W.; Stubbs, G.; Schwieters, C. D.; Lee, V. M. Y.; George, J. M.; Rienstra, C. M. Solid-State NMR Structure of a Pathogenic Fibril of Full-Length Human α-Synuclein. *Nat. Struct. Mol. Biol.* **2016**, *23* (5), 409–415. https://doi.org/10.1038/nsmb.3194.
(86) Trott, O.; Olson, A. J. AutoDock Vina: Improving the Speed and Accuracy of Docking with a New Scoring Function, Efficient Optimization, and Multithreading. *J. Comput. Chem.* **2010**, *31* (2), 455–461. https://doi.org/10.1002/jcc.21334.
(87) Robustelli, P.; Piana, S.; Shaw, D. E. Developing a Molecular Dynamics Force Field for Both Folded and Disordered Protein States. *Proc. Natl. Acad. Sci.* **2018**, *115* (21). https://doi.org/10.1073/pnas.1800690115.
(88) Zarranz, J. J.; Alegre, J.; Gómez-Esteban, J. C.; Lezcano, E.; Ros, R.; Ampuero, I.; Vidal, L.; Hoenicka, J.; Rodriguez, O.; Atarés, B.; Llorens, V.; Tortosa, E. G.; Del Ser, T.; Muñoz, D. G.; De Yebenes, J. G. The New Mutation, E46K, of α-Synuclein Causes Parkinson and Lewy Body Dementia: New α-Synuclein Gene Mutation. *Ann. Neurol.* **2004**, *55* (2), 164–173. https://doi.org/10.1002/ana.10795.
(89) Appel-Cresswell, S.; Vilarino-Guell, C.; Encarnacion, M.; Sherman, H.; Yu, I.; Shah, B.; Weir, D.; Thompson, C.; Szu-Tu, C.; Trinh, J.; Aasly, J. O.; Rajput, A.; Rajput, A. H.; Jon Stoessl, A.; Farrer, M. J. Alpha-Synuclein p.H50Q, a Novel Pathogenic Mutation for Parkinson's Disease: α- Synuclein p.H50q, A Novel Mutation For Pd. *Mov. Disord.* **2013**, *28* (6), 811–813. https://doi.org/10.1002/mds.25421.
(90) Lesage, S.; Anheim, M.; Letournel, F.; Bousset, L.; Honoré, A.; Rozas, N.; Pieri, L.; Madiona, K.; Dürr, A.; Melki, R.; Verny, C.; Brice, A.; for the French Parkinson's Disease Genetics Study Group. G51D α-Synuclein Mutation Causes a Novel Parkinsonian-

Pyramidal Syndrome: SNCA G51D in Parkinsonism. *Ann. Neurol.* **2013**, *73* (4), 459–471. https://doi.org/10.1002/ana.23894.
(91) Lee, M. K.; Stirling, W.; Xu, Y.; Xu, X.; Qui, D.; Mandir, A. S.; Dawson, T. M.; Copeland, N. G.; Jenkins, N. A.; Price, D. L. Human α-Synuclein-Harboring Familial Parkinson's Disease-Linked Ala-53 → Thr Mutation Causes Neurodegenerative Disease with α-Synuclein Aggregation in Transgenic Mice. *Proc. Natl. Acad. Sci.* **2002**, *99* (13), 8968–8973. https://doi.org/10.1073/pnas.132197599.
(92) Pasanen, P.; Myllykangas, L.; Siitonen, M.; Raunio, A.; Kaakkola, S.; Lyytinen, J.; Tienari, P. J.; Pöyhönen, M.; Paetau, A. A Novel α-Synuclein Mutation A53E Associated with Atypical Multiple System Atrophy and Parkinson's Disease-Type Pathology. *Neurobiol. Aging* **2014**, *35* (9), 2180.e1-2180.e5. https://doi.org/10.1016/j.neurobiolaging.2014.03.024.
(93) Strohäker, T.; Jung, B. C.; Liou, S.-H.; Fernandez, C. O.; Riedel, D.; Becker, S.; Halliday, G. M.; Bennati, M.; Kim, W. S.; Lee, S.-J.; Zweckstetter, M. Structural Heterogeneity of α-Synuclein Fibrils Amplified from Patient Brain Extracts. *Nat. Commun.* **2019**, *10* (1), 5535. https://doi.org/10.1038/s41467-019-13564-w.
(94) Honorato, R. V.; Trellet, M. E.; Jiménez-García, B.; Schaarschmidt, J. J.; Giulini, M.; Reys, V.; Koukos, P. I.; Rodrigues, J. P. G. L. M.; Karaca, E.; Van Zundert, G. C. P.; Roel-Touris, J.; Van Noort, C. W.; Jandová, Z.; Melquiond, A. S. J.; Bonvin, A. M. J. J. The HADDOCK2.4 Web Server for Integrative Modeling of Biomolecular Complexes. *Nat. Protoc.* **2024**, *19* (11), 3219–3241. https://doi.org/10.1038/s41596-024-01011-0.
(95) Tomita, T.; Ieguchi, K.; Sawamura, T.; Maru, Y. Human Serum Amyloid A3 (SAA3) Protein, Expressed as a Fusion Protein with SAA2, Binds the Oxidized Low Density Lipoprotein Receptor. *PLOS ONE* **2015**, *10* (3), e0118835. https://doi.org/10.1371/journal.pone.0118835.
(96) Buck, M. D.; Gouwy, M.; Wang, J. M.; Snick, J. V.; Opdenakker, G.; Struyf, S.; Damme, J. V. Structure and Expression of Different Serum Amyloid A (SAA) Variants and Their Concentration-Dependent Functions During Host Insults. *Curr. Med. Chem. 23* (17), 1725–1755. https://doi.org/10.2174/0929867323666160418114600.
(97) Thorn, C. F.; and Whitehead, A. S. Differential Transcription of the Mouse Acute Phase Serum Amyloid A Genes in Response to Pro-Inflammatory Cytokines. *Amyloid* **2002**, *9* (4), 229–236. https://doi.org/10.3109/13506120209114098.
(98) Chiba, T.; Han, C. Y.; Vaisar, T.; Shimokado, K.; Kargi, A.; Chen, M.-H.; Wang, S.; McDonald, T. O.; O'Brien, K. D.; Heinecke, J. W.; Chait, A. Serum Amyloid A3 Does Not Contribute to Circulating SAA Levels. *J. Lipid Res.* **2009**, *50* (7), 1353–1362. https://doi.org/10.1194/jlr.M900089-JLR200.
(99) Chait, A.; den Hartigh, L. J.; Wang, S.; Goodspeed, L.; Babenko, I.; Altemeier, W. A.; Vaisar, T. Presence of Serum Amyloid A3 in Mouse Plasma Is Dependent on the Nature and Extent of the Inflammatory Stimulus. *Sci. Rep.* **2020**, *10* (1), 10397. https://doi.org/10.1038/s41598-020-66898-7.
(100) Deguchi, A.; Tomita, T.; Omori, T.; Komatsu, A.; Ohto, U.; Takahashi, S.; Tanimura, N.; Akashi-Takamura, S.; Miyake, K.; Maru, Y. Serum Amyloid A3 Binds MD-2 To Activate P38 and NF-κB Pathways in a MyD88-Dependent Manner. *J. Immunol.* **2013**, *191* (4), 1856–1864. https://doi.org/10.4049/jimmunol.1201996.
(101) Cheng, N.; He, R.; Tian, J.; Ye, P. P.; Ye, R. D. Cutting Edge: TLR2 Is a Functional Receptor for Acute-Phase Serum Amyloid A1. *J. Immunol.* **2008**, *181* (1), 22–26. https://doi.org/10.4049/jimmunol.181.1.22.

(102) Jayaraman, S.; Gantz, D. L.; Haupt, C.; Gursky, O. Serum Amyloid A Forms Stable Oligomers That Disrupt Vesicles at Lysosomal pH and Contribute to the Pathogenesis of Reactive Amyloidosis. *Proc. Natl. Acad. Sci.* **2017**, *114* (32), E6507–E6515. https://doi.org/10.1073/pnas.1707120114.
(103) Sosnowska, M.; Skibiszewska, S.; Kamińska, E.; Wieczerzak, E.; Jankowska, E. Designing Peptidic Inhibitors of Serum Amyloid A Aggregation Process. *Amino Acids* **2016**, *48* (4), 1069–1078. https://doi.org/10.1007/s00726-015-2167-y.
(104) Louros, N.; Konstantoulea, K.; De Vleeschouwer, M.; Ramakers, M.; Schymkowitz, J.; Rousseau, F. WALTZ-DB 2.0: An Updated Database Containing Structural Information of Experimentally Determined Amyloid-Forming Peptides. *Nucleic Acids Res.* **2020**, *48* (D1), D389–D393. https://doi.org/10.1093/nar/gkz758.
(105) Tien, M. Z.; Sydykova, D. K.; Meyer, A. G.; Wilke, C. O. PeptideBuilder: A Simple Python Library to Generate Model Peptides. *PeerJ* **2013**, *1*, e80. https://doi.org/10.7717/peerj.80.
(106) Case, D. A.; Aktulga, H. M.; Belfon, K.; Cerutti, D. S.; Cisneros, G. A.; Cruzeiro, V. W. D.; Forouzesh, N.; Giese, T. J.; Götz, A. W.; Gohlke, H.; Izadi, S.; Kasavajhala, K.; Kaymak, M. C.; King, E.; Kurtzman, T.; Lee, T.-S.; Li, P.; Liu, J.; Luchko, T.; Luo, R.; Manathunga, M.; Machado, M. R.; Nguyen, H. M.; O'Hearn, K. A.; Onufriev, A. V.; Pan, F.; Pantano, S.; Qi, R.; Rahnamoun, A.; Risheh, A.; Schott-Verdugo, S.; Shajan, A.; Swails, J.; Wang, J.; Wei, H.; Wu, X.; Wu, Y.; Zhang, S.; Zhao, S.; Zhu, Q.; Cheatham, T. E.; Roe, D. R.; Roitberg, A.; Simmerling, C.; York, D. M.; Nagan, M. C.; Merz, K. M. AmberTools. *J. Chem. Inf. Model.* **2023**, *63* (20), 6183–6191. https://doi.org/10.1021/acs.jcim.3c01153.
(107) Price, D. J.; Brooks, C. L. A Modified TIP3P Water Potential for Simulation with Ewald Summation. *J. Chem. Phys.* **2004**, *121* (20), 10096–10103. https://doi.org/10.1063/1.1808117.
(108) Pettersen, E. F.; Goddard, T. D.; Huang, C. C.; Meng, E. C.; Couch, G. S.; Croll, T. I.; Morris, J. H.; Ferrin, T. E. UCSF ChimeraX: Structure Visualization for Researchers, Educators, and Developers. *Protein Sci. Publ. Protein Soc.* **2021**, *30* (1), 70–82. https://doi.org/10.1002/pro.3943.